Modeling and Design of Hydraulic Power Take-Offs for Ocean Wave-Powered Reverse Osmosis Desalination

A DISSERTATION
SUBMITTED TO THE FACULTY OF THE GRADUATE SCHOOL
OF THE UNIVERSITY OF MINNESOTA
BY

Jeremy Wayne Simmons II

IN PARTIAL FULFILLMENT OF THE REQUIREMENTS
FOR THE DEGREE OF
DOCTOR OF PHILOSOPHY

James Donald Van de Ven

April, 2024

Acknowledgements

There are many people that have earned my gratitude for their contribution to my time in graduate school and to the work presented in this thesis.

First, I would like to thank my mother for being the caring parent I needed and a friend with which to ponder the mysteries of the universe.

I would like to thank Dr. Daniel Dolan for encouraging me to pursue a PhD, for writing the "best letter of recommendation" he had yet written, and for discussing how we grow.

I would like to thank Dr. James Van de Ven for support and encouragement and for being a caring guide.

I would like to thank Dr. Erik Storlie for just sitting.

I would like to thank Michael Kelly for giving me my first exposure to wave energy while we were both attending South Dakota School of Mines and Technology.

I would like to thank the folks whom I worked with through Resolute Marine Energy: Allan Chertok, Marcus Gay, Seth McFadyen, Matt Folley, Darragh Clabby, Bill Staby, and Linda Rauch of Next Rung Technology.

I would like to thank the folks whom I worked with at the National Renewable Energy Laboratory during my appointment with the Marine and Hydrokinetic Graduate Student Research Program: Yi-Hsiang Yu, Michael Lawson, and Scott Jenne. I especially appreciate Yi-Hsiang's effort to supply me with the Simulink Models they had used in their 2017 publication on wave-powered reverse osmosis.

I would like to acknowledge the support of funding agencies. The research presented in Chapter 2 and Chapter 5 were supported in part by an appointment with the Marine and Hydrokinetic Graduate Student Research Program sponsored by the U.S. Department of Energy (DOE), Office of Energy Efficiency and Renewable Energy, and Water Power Technologies Office. This program is administered by the Oak Ridge Institute for Science and Education (ORISE) for the DOE. ORISE is managed by Oak Ridge Associated Universities (ORAU) under DOE contract number DE-SC0014664. Material presented in Chapter 3 is based upon work supported by the DOE through DE-SC0019995. Material presented in Chapter 4 is based upon work supported by the National Science Foundation (NSF) under Grant No. CMMI-2206018. All opinions expressed in this material are the my own and do not necessarily reflect the policies and views of DOE, ORAU, ORISE, or NSF.

I would also like to acknowledge the support of Resolute Marine Energy, Inc. for work presented in Chapter 2 through a subcontract of DOE SBIR Phase II Grant No. DE-SC0017699.

Dedication

To the engineer: may we be wise in solving problems and in giving guidance about our technology.

Abstract

Ocean wave-powered desalination of seawater using reverse osmosis (RO) presents an important opportunity for coastal communities as an economical and clean source of fresh water. However, the breadth and depth of study in the design of hydraulic power take-offs (PTOs) for ocean wave-powered RO is not sufficient for reliable high-performance. This work introduces several novel PTO architectures for wave-powered RO systems that take the approach of pressurizing seawater directly using a pump that is driven by the wave energy converter (WEC). These architectures include co-generation of electricity with fresh water to support the system without reliance on a local electrical grid. These architectures are modeled and compared in terms of the size of the WEC-driven pump, the RO membrane module, high-pressure accumulator volume, and the yearly average rate of permeate production. Results show that a parallel-type PTO architecture that closely resembles the state-of-the-art is consistently outperformed by series-type architectures. The series-type architecture, which is examined with and without an integrated switch-mode power transformer, produces as much fresh water as the parallel-type architecture while (1) using a WEC-driven pump that is 30–74 percent smaller without the switch-mode power transformer and 70–92 percent smaller with the switch-mode power transformer and (2) requiring 75 percent less high-pressure accumulator volume. Results also show that varying the active RO membrane area as a function of sea conditions can improve performance in terms of WEC-driven pump size, RO membrane module size, and permeate production, by 7–41 percent. Using model predictive control as an optimal load control method, this work also finds that a variable displacement WEC-driven pump can enhance productivity by 11–29 percent. Pipeline modeling methods are also examined for their use in wave energy systems and results show that a lumped parameter pipeline model that represents a pipeline in multiple segments is sufficient for the design of these systems, subject to a constraint on

the length of pipe each segment represents. As a whole, this work provides guidance to the design of PTOs in future projects with insight into selecting the architecture of the PTO, formulation of multi-objective design problems, and models that can be used effectively for model-based design.

Contents

List of Tables

List of Figures

Chapter 1

Introduction

1.1 Background

Researchers have recently estimated that four billion people experience severe water scarcity for at least one month out of the year [1] [1]. Despite the prevalence of water on Earth, only 0.8 percent of water on earth is accessible in the form of river water, fresh lake water, or groundwater [3]. Furthermore, local availability is sparse and not all source can support an area sustainably [4]. Most water, about 97 percent, carries too much salt (e.g., sea water) to be useful and the rest is otherwise inaccessible.

For arid and drought prone coastal regions, like areas of the southwest United States, North Africa, and the Middle East, desalination and treatment of seawater may be a feasible solution for increasing sustainable resources of water. However, all desalination processes require significant amounts of power to perform and add to the energy demands of a community. Reverse osmosis desalination is a membrane-based process used to separate water from dissolved solids using high pressure as a driving force. It is a common desalination process and is three to six times more energy efficient than thermal desalination processes [5, 6].

[1] Qualifying and quantifying water scarcity is a complex problem and there are many metrics used to qualify water scarcity [2]

Researchers have recently turned their attention toward renewable energy, such as solar, wind, ocean wave energy, as direct sources of power for desalination [7, 8, 9]. In fact, the US Department of Energy has recently encouraged commercial application of these methods by hosting competitions for teams to design and build desalination systems powered by solar energy and ocean wave energy [10]. As a way to reduce cost and improve the efficiency of a wave-powered desalination process, a community of researchers and a developing wave energy industry have considered integrating the reverse osmosis process into the hydraulic circuit of a wave energy converter (WEC) power take-off (PTO) (the subsystem responsible for loading the WEC and converting power) to avoid losses in the conversion of power to and from mechanical and electrical power for pressurizing feedwater [9, 11, 12, 13, 14].

The global resource for power in wind generated ocean waves has been estimated to be about 2.1 TW [15]. Compared to the world average power consumption in 2018 of 18 TW [16, 17]; this is not insignificant. However, the same study estimated that only about 97 GW is extractable with current wave energy conversion technology. Nonetheless, coastal regions with convenient access to the resource would benefit from a local wave energy resource offsetting the power demand of desalination. This was found to be plausible for the Gran Canaria Island, an arid island off the coast of northwestern Africa that depends on desalination to meet roughly 55 percent of its water needs [18]. Researchers at the National Renewable Energy Laboratory also estimated the cost of water production powered directly from wave energy would be competitive with other source of water in the drought prone state of California [19].

Conversion of wave energy to fresh water via reverse osmosis is a considerable technical challenge. The wave energy conversion process is a characteristically variable process that deals with absorbing power under the force of slow, random, and irregular waves. For instance, the ratio between the peak and mean power absorbed by a WEC has been estimated to be anywhere between 7 and 58 to 1, depending on the system design and control scheme [20, 21]. In contrast, conventional RO processes are characteristically

steady, with changes to operation being made very slowly and only as feedwater temperature changes or the membranes accumulate debris and degrade. This steady operation is necessary, to a degree, for the relatively fragile components of RO systems.

The work presented in this thesis addresses the challenge of designing an effective and robust wave-powered reverse osmosis systems by considering the trade-offs between several power take-off architectures. The contributions of this thesis include the introduction of several novel power take-off architectures for this application, the formulation and execution of three multi-objective design problems, and comparative analysis of the architectures within these multi-objective design problems. Furthermore, the analysis performed as part of one of these comparative studies contributes clear motivation for further work to understand and clarify the limits of conventional reverse osmosis components when subjected to significant pressure variation. In addition to exploring the architecture for the power take-off, this work contributes to the design of these systems with a comparative study examining modeling practices for capturing the effects of long pipelines when they appear in the context of a wave-energy system.

1.2 Literature Review

This section provides a more detailed review of the technologies involved in wave-powered RO systems and on the state of the literature for these systems. First, a review of the RO process is provided with a discussion on modeling the process and the design constraints placed on RO systems. Next, the challenge with the variability of ocean waves is discussed. This is followed by a review of the various PTO architectures considered for both electrical power producing and water producing wave energy systems. The review concludes with a discussion on long pipelines and a comparison of modeling standards in literature to the case of wave-powered systems.

1.2.1 Reverse Osmosis Desalination

Reverse osmosis (RO) desalination is a membrane-based process used to separate water from seawater, which has high concentrations of dissolved salts and suspended solids. The membranes are designed to be selectively permeable to water molecules and relatively impermeable to larger molecules like most salt ions. Pressure is applied to the side of the membrane with higher salt concentration and serves as the driving force for diffusion of water though the membrane. This pressure must overcome the chemical potential that results from the difference in solute concentration; the balancing pressure to the chemical potential is the osmotic pressure.

The behavior of this process is illustrated by Figure 1.1, which shows the trends in water and salt flux across a conventional RO membrane as a function of the pressure differential applied to the membrane. The flux of water is approximately linear with pressure and is offset by the osmotic pressure (usually between 2 and 3 MPa for seawater). Salt flux is approximately constant. The bottom plot shows that the rejection of the salt, based on the difference in salt concentration, increases for pressures above the osmotic pressure but is not effective (i.e., with salt rejection greater than about 95 percent) until a higher pressure of about 4 MPa (600 psi) is reached.

In the conventional, continuous process of reverse osmosis, the pressurized stream flows across the surface of the membrane. The feedwater that enters the process becomes more concentrated as water is driven through the membrane. The more concentrated brine, or concentrate, is discharged as a waste stream, often back into the ocean. The less concentrated water, or permeate, is discharge as a product stream to be made usable by other processes (e.g., by the introduction of minerals for drinkability). In early process designs, the concentrate stream was throttled from the higher feed pressure to the lower pressure of the discharge piping. Now, the convention is to include a device called an energy recovery unit (ERU) to use the high pressure of the concentrate stream to do useful work toward pressurizing the feedwater. This provides a large improvement to

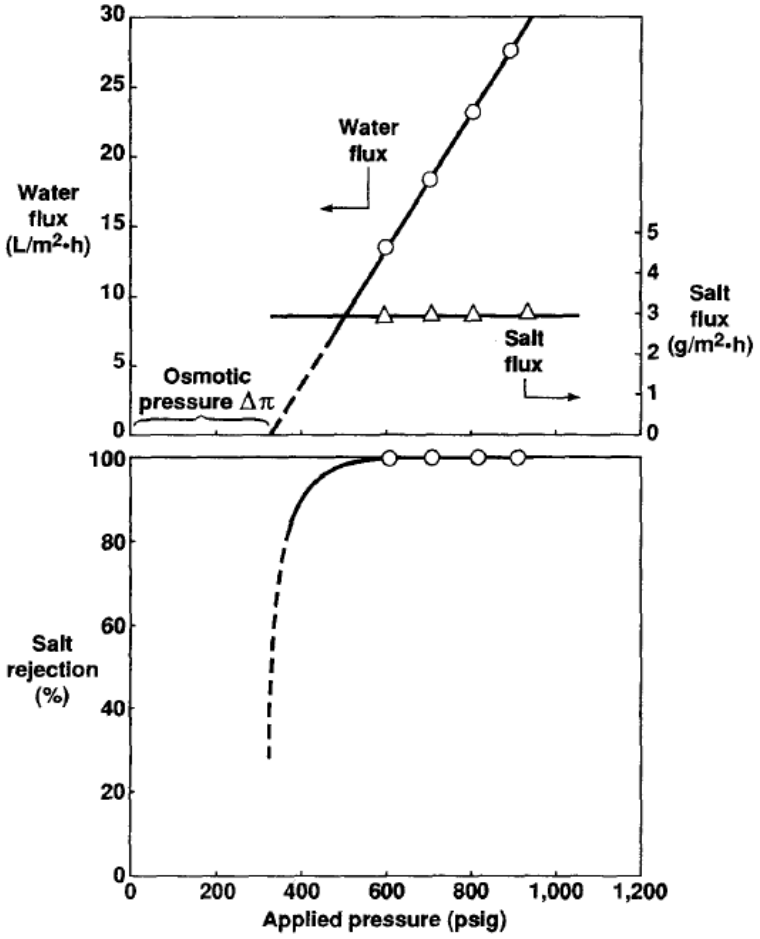

Figure 1.1: Water flux and salt rejection data and curve fit in a reverse osmosis membrane [22].

efficiency of the process since the concentrate steam accounts for one to two times the volumetric rate of the permeate stream.

Modeling the RO Process

Modeling the RO process can be performed in a variety of ways. Manufacturers provide software for system design analysis (see [23] for a list of software programs by manufacturer). However, these software packages are not useful for time-domain simulations. For simulations of wave-powered RO systems, researchers have obtained explicit models by manually collecting data from these software packages and performing least squares model fitting [11, 24]. Although the explicit model is computationally inexpensive in a time-domain simulation, this is time intensive up-front and may prevent automated design of the RO system. Alternatively, the system of nonlinear equations that these software programs implement can be implemented into the system model, giving direct access to design parameters without requiring manual collection of data. For example, the technical manual for FilmTec^{TM} membranes includes a system of equations that includes nonlinear effects in the process [25]. Researchers studying photovoltaic-powered RO systems have implemented this approach [26].

Constraints on the RO Process

There are several important limits to consider in the design of an RO system. First, a number of static constraints make up a window of operation with respect to pressure and flow rate. Several of these constraints are shown in Figure 1.2 and are specified by membrane manufactures, as in [25]. Each of these relate to either fouling of the membrane or to mechanical damage. For example, a minimum brine flow rate is required to prevent accumulation of fouling material while a maximum brine flow rate is specified to limit flow forces on the membranes.

Additionally, start-up and shut-down of RO systems should be performed relatively slowly, with a rate of pressure change less than 70 kPa per second, to avoid mechanical

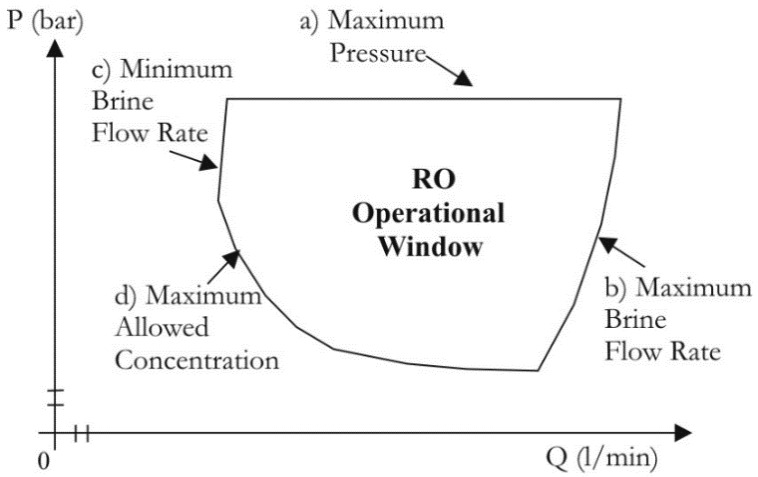

Figure 1.2: RO membrane operational window, where the pressure (P) is the pressure differential across the membrane and the flow rate (Q) is the rate of feed water flow [27].

damage to the membrane and membrane housing [28, 23, 25]. Extension of this constraint to continuous operation is not made explicit. However, in normal operation of a conventional RO plant, the pressure is held nearly constant, so it is understandable that an extension of this constraint to normal operation has not been made explicit. Furthermore, the value of the constraint seems to not be substantiated in any literature.

The lack of clarity suggests that the pressure rate-of-change constraint may be a conservative value and that the underlying mechanisms may not be well understood. However, both [28] and [23] claim this constraint relates to mechanical damage to the membrane and membrane housing such as compaction of the membrane or cracking on the housing. Until the constraint is reevaluated it should be considered valid, especially for the design of the highly variable wave-powered application. Prior work on wave-powered RO systems has neglected this pressure dynamic constraint. In the work by Folley et al., the constraint was acknowledged but neglected for lack of substantiation and intuition that RO system components could be designed to be more robust if the wave-powered RO market created the demand [29].

1.2.2 Ocean Waves and Wave Energy Harvesting

A substantial challenge in the design of a wave-powered plant is made apparent when timescales over which wave energy is variable are considered. Figure 1.3 shows a representation of the surface elevation in time for a fixed location. It also shows the resulting force that the passing waves would have on a two-meter wide buoy-type WEC [30]. The surface elevation is essentially random and varies at several time scales: within a single wave, wave-to-wave, and between groups of waves. Further, Figure 1.3 represents a single sea condition that may persist at the same mean energy level over a several hours; this mean energy level is variable as well.

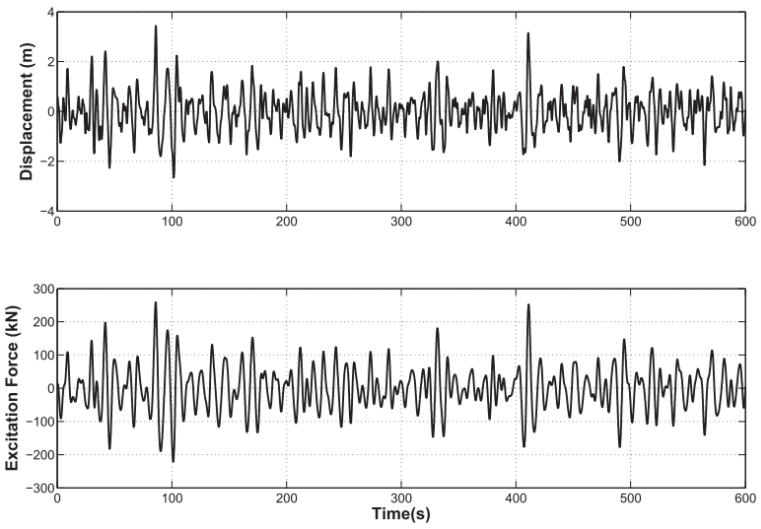

Figure 1.3: Example of surface displacement in realistic sea conditions and the resulting force exerted on a buoy with radius of 2 meters and draft of 4 meters.

It is at the longer time scales that researchers have developed a theory of sea states, as it is at this scale that wave conditions become consistent enough to characterize statistically [31]. In this theory, the surface elevation is described by a stochastic description of the mean energy as a function of frequency, termed a wave spectrum. These wave spectra can be transformed to the time-domain for simulation and analysis of marine systems, such as WECs. Parameterized, analytical expressions such, as the JONSWAP

spectrum [32] and Pierson-Moskowitz spectrum, [33] capture the typical shape of the distribution and can be parameterized by relatively short time-series measurements of the surface elevation (typically 20-minute worth of data [31]). The dominant wave period and a characteristic wave height are the most important parameters that characterize these sea states.

The extraction of energy from ocean waves is like any other form of power transmission involving motion under force. Power is captured by a WEC when a surface is moved by the hydrodynamic force of a wave and is reacted against by the PTO. The PTO generally reacts against the motion of the WEC and is responsible for transmitting, converting, and conditioning the power extracted from the waves. There are many concepts that have been proposed for the WEC and there is yet to be real convergence on a particular concept within the community [34, 35, 36, 37]. Common WEC types include (1) buoy-like devices referred to as point absorbers, (2) flap-type devices referred to as oscillating wave surge converters, (3) attenuators that articulate with joint rotations perpendicular to the wave direction and follow the surface profile of the waves, (4) oscillating water columns that extract energy from the air compressed by a raising and falling water-level within a structure, and (5) over-topping devices that capture seawater flowing over the device into a basin with a gravity fed turbine. Figure 1.4 gives an example for how power may be transmitted from the WEC to the PTO for the case of an OWSC driving a hydraulic cylinder used as a pump within a hydraulic PTO circuit.

The load with which the PTO reacts against the WEC is often referred to as the damping force and serves an important function in the efficiency of power capture. Providing the optimal load control scheme has been the subject of many researchers' attention [38]. The two simplest versions of the load control problem is to determine either a constant, Coulomb-like damping force or a damping rate (such that the load is proportional to the velocity) that maximizes the power absorption. From these two

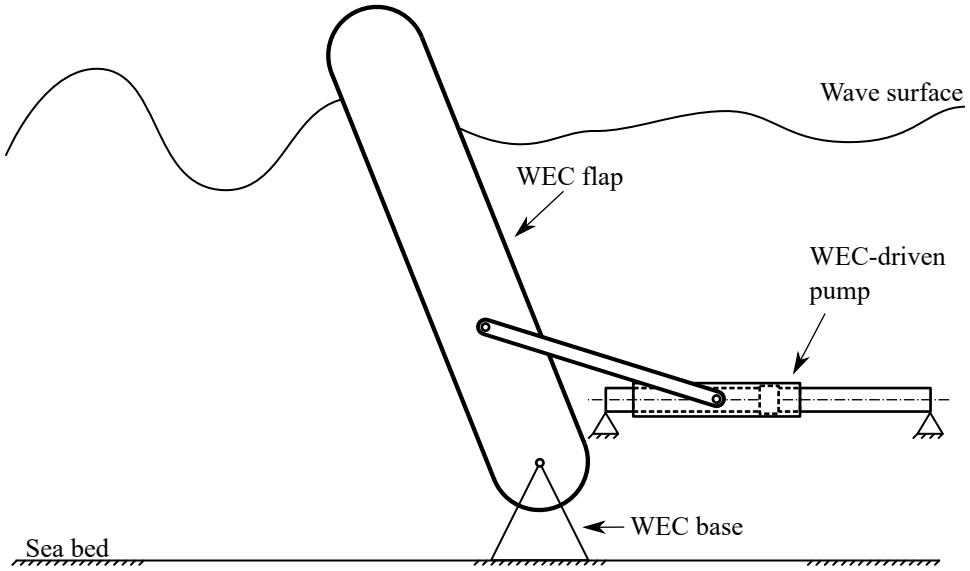

Figure 1.4: Example for how power may be transmitted from the WEC to the PTO for the case of an OWSC driving a hydraulic cylinder used as a pump within a hydraulic PTO circuit.

simple strategies, the constant Coulomb-like reaction force is often considered for hydraulic systems [36]. However, a load that is proportional to the WEC velocity found favor in the field for being amenable to frequency-domain analysis [39].

More advanced approaches have been considered as the field has developed. Approaches include assisting the device into a resonance condition by i) feeding energy back into the WEC from the PTO [40], ii) switching between a high and low forces [41], and iii) restraining the motion of the WEC for some period [42]. More recently, model predictive control and machine learning (e.g., neural networks) have been applied to the problem in order to give optimal control over the load on the WEC [38].

1.2.3 Power Take-Off Design - Wave Energy and Wave-Powered Desalination

In this subsection, the scope of efforts to design an effective hydraulic PTO is examined for both the electrical power producing and water producing applications. By far, most

work has focused on the electrical power producing systems and has resulted in the most diversity in PTO architectures. The first part of this review gives an overview of work exploring the design of hydraulic PTOs for electrical power production with a focus on this diversity. This is then contrasted with work concerned with coupling a hydraulic PTO directly to a reverse osmosis process. This field lacks the same diversity in PTO architecture.

Power Take-off Design for Electrical Power Production

Serious study of hydraulic PTO design in the electrical energy producing application of wave energy harvesting began around 2010 despite the initial surge in research into the extraction of wave energy coming in the late 1970s with the oil crisis of that period. In 2009, Plummer and Schlotter [43] suggested that prior analysis of wave energy systems neglected to consider limitations and losses in the hydraulic power take-offs and that, at best, researchers had assumed that PTOs had a constant efficiency across operating conditions. The authors illustrated how significant the non-ideal characteristics of hydraulic machines are by comparing the performance of a WEC and its PTO in simulation design using two methods, (1) with the assumption of ideal machines and (2) with realistic loses.

Soon after, researchers considered more realistic models of hydraulic power take-offs and began pointing out significant trade-offs to consider in their design. For example, analysis that included the diminishing efficiency of a hydraulic motor in part-load operating conditions led Cargo et al. [44] to recommend that hydraulic power take-offs either implement a large number of smaller motors or implement motors with better part load efficiency like digitally variable displacement motors [45][2].

Two PTO architectures are considered to represent the simplest embodiment of a hydraulic PTO. These are the variable pressure PTO and the constant pressure PTO,

[2]Their recommendation was in line with previous intuitions and findings about the poor part-load efficiency of hydraulic systems given in [43].

shown in Figure 1.5 [35, 46, 47]. Most researchers have considered the constant pressure architecture [30, 36, 41, 48, 49] because it offers a significant degree of power smoothing and can be more efficient since the variability of the hydraulic motor operating condition can be small. However, the variable pressure PTO is considered to offer greater control over the reaction forces on the WEC and thus greater power capture.

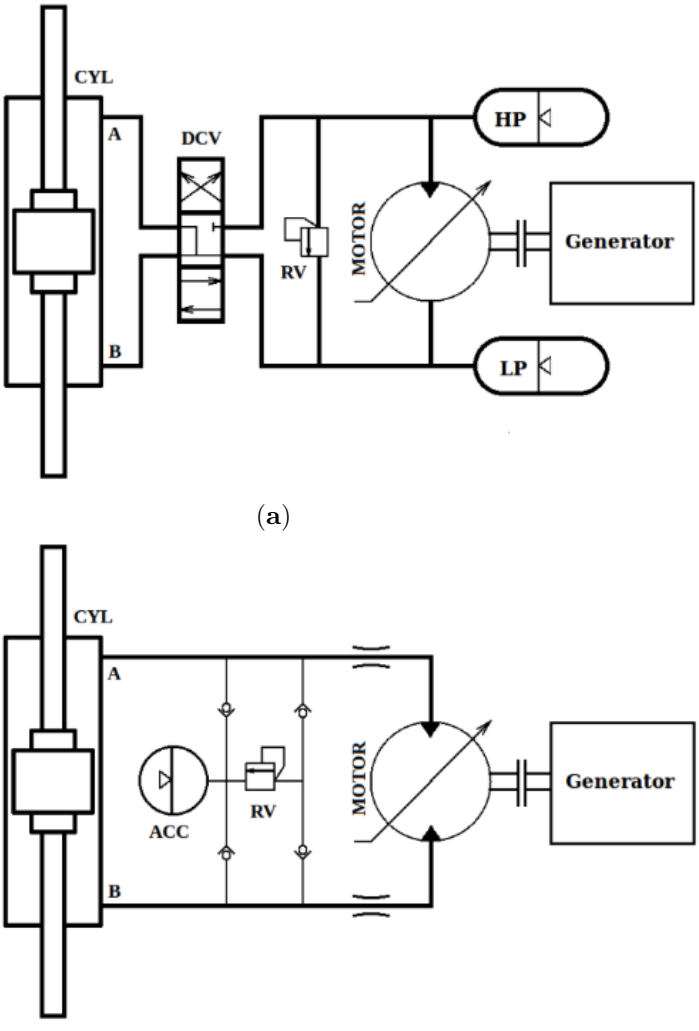

Figure 1.5: Two basic hydraulic architectures: the constant pressure PTO 1.5a and the variable pressure PTO 1.5b [46].

Costello et al., in [46], studied both these architectures with the aim of clarifying the trade-offs between them and to uncover the challenges of each that might be overcome by alterations to these architectures. The results of the study confirmed that the variable pressure PTO could capture more power and that it was less efficient than the constant pressure PTO. The study found that the difference in performance was not large and that the choice of hydraulic motor and generator architecture should be the deciding factor in the choice of architecture. However, later work challenged these distinctions.

Cargo et al., in [30], considered how well real-time control over the reaction force, by varying the system pressure, could improve the performance of the constant pressure architecture. Their study revealed that the relatively slow dynamics of accumulators prevented effective real-time tuning of the PTO reaction force at the time scale of each passing wave, as is achievable with the variable pressure PTO architecture.

Hansen et al. [20] considered the variable pressure PTO but considered a higher degree of control than in [46]. Their architecture considered a four-quadrant control over the motor torque using a variable displacement motor whereas [46] considered only two quadrant control of the motor torque. This allowed for a reversal of power flow from the PTO to the WEC that could assist the WEC into a resonant condition.

Later, Hansen et al. [50] considered an alteration to the constant pressure architecture that avoided the slow control over the PTO force found by [30] and also enabled four-quadrant control. Instead of the fixed displacement WEC-driven pumps previously considered, this new architecture included a discretely variable displacement pump comprised for a hydraulic cylinder having several switched chambers with different piston areas.

Finally, Dießel et al. considered a similar approach to [50] providing variable displacement for the constant pressure architecture using multiple cylinders switched in and out of a pumping mode [47]. The approach uses a single on/off valve and two check valves that can latch in the open position. This approach involves fewer and simpler components than [50] and gives faster control than the unaltered constant pressure

architecture, but is slower than in [50] and does not allow for four quadrant control.

Power Take-Off Design for Wave-Powered Reverse Osmosis

The wave-powered RO system designs considered in literature and by industry take relatively simple approaches to addressing the design constraints, but they are likely overly expensive and inefficient. These designs rely on large of hydraulic-pneumatic accumulator volumes and the dissipation of power through pressure relief valves to deal with the variation in flow supplied by the WEC-driven pump and meet the constraints on operating pressures imposed by integration of the RO module [11, 51, 52].

The first wave-powered reverse osmosis system was built in the 1980's [51, 53]. The DELBUOY, as it was called, was comprised of a 2.5-meter buoy driving a hydraulic cylinder serving as a sea water pump to the RO module with an accumulator to smooth pressure variation. This same circuit architecture was considered again in the 2000's with the development of a control system to maintain a desired RO feed pressure [14, 54].

Folley et al. reintroduced the concept of wave-powered reverse osmosis with a step toward a more energy efficient process by introducing an architecture that included an ERU [11, 29]. As shown in Figure 1.6, this ERU is a pressure exchanger-intensifier used to recover power from the concentrate stream. The work included parameter studies on the effect of the accumulator volume and the number of RO elements on water production and product salt concentration. This level of analysis went beyond the work published by Hicks and Please [51] but was narrowly focused on optimizing production rates for this simple design without consideration of constraints on the process other than the maximum pressure.

Yu and Jenne introduced a model of a system adapted from [29]. They modeled the system to estimate the cost of water production [19] and studied the dynamics and design of the plant [24]. The model was implemented using WEC-Sim [55], a modeling framework developed by the National Renewable Energy Lab in Simulink and SimScape Fluids, the MATLAB-based graphical user interface. They presented analysis similar

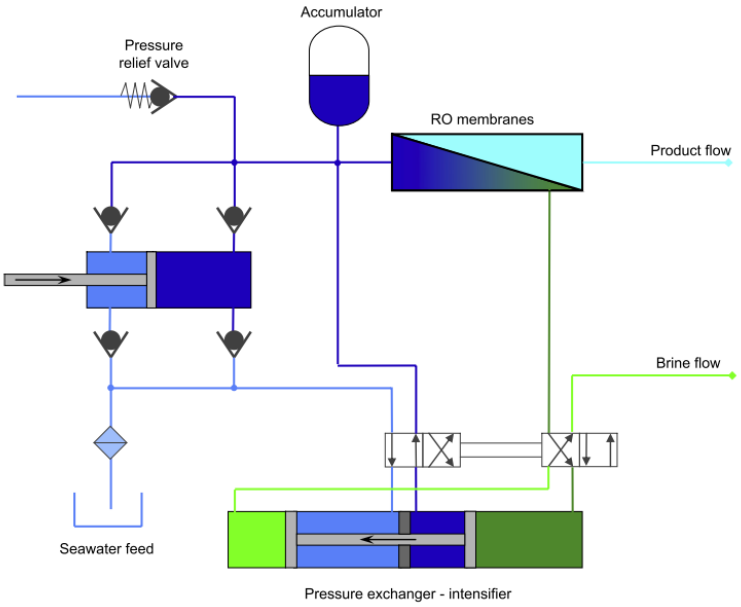

Figure 1.6: Wave energy powered reverse osmosis power take-off schematic[29].

to the work by Folley et al. [29] concerned with determining the optimal capacity (i.e., effectively the total installed membrane area) for minimizing the cost of water [19]. They also considered the effect of the total accumulator volume on the magnitude of variation in pressure during plant operation, settling on a total accumulator volume of 6000 liters [24]. For a sense of scale, this plant was rated for about 150-kW of average power throughput. It is likely that these systems will require significantly large volumes of accumulators. Yet, no study on the design of these systems has considered the constraint on the rate-of-change in pressure of the RO process, a constraint that may drive the total accumulator volumes required even higher.

More recent works have reverted to using the simpler design without energy recovery [56, 57, 58]. Each of these present a design concept for the system they consider and report model results using WEC-Sim but do not present any design analysis aimed at improving the performance of the PTO. Their models in WEC-Sim are modifications of the WEC-Sim model built by Yu and Jenne [24].

The only recent work to consider a different design for the PTO has considered a batch RO process with a conventional hydraulic power transformer and an electric generator that is driven by a separate hydraulic motor[59]. This system is shown in Figure 1.7. The transformer is formed by coupling the shafts of a turbine and pump. The shaft speed is controlled with either a throttling valve or an inline hydraulic motor and electric motor/generator. Control of the shaft speed enables control of the batch RO process. The analysis of this work focused on estimating the levelized cost of water and the specific energy consumption of the process. No design analysis was presented to determine component sizes but the work did compare the performance difference between using a throttling valve and a hydraulic motor for speed control of the hydraulic power transformer.

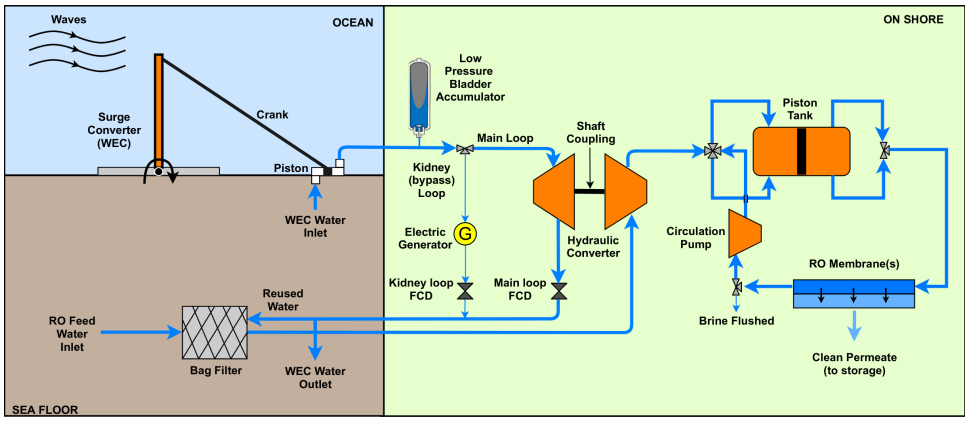

Figure 1.7: Schematic for a wave-powered batch RO system [59].

Other practical analysis such as the electrical power demands, avoiding cavitation, and meeting conventional constraints on the RO process have not been considered in any literature on these directly coupled, wave-powered RO systems. Notably, an intake system capable of providing an initial filtering processes and providing an elevated pressure to the WEC-driven pump inlet has been neglected. Instead, it has been assumed that filtered seawater will be available from a sea well with low flow resistance.

The PTO architectures studied for wave-powered RO have not been iterated upon

as much as the electrical power producing PTOs. However, some of the approaches applied to the electrical power producing PTO architectures could be applied to the wave-powered RO PTOs as well, especially those for the constant-pressure type PTO architectures. Doing so could serve to improve the effectiveness of power absorption but may not address the requirement for large accumulator volumes. The field has not presented any alternative to using large accumulators and pressure relief valves for power smoothing in wave powered RO systems.

1.2.4 Pipeline Modeling for Wave Energy Systems

Prior modeling and design analyses given in literature are likely inadequate for practical implementation because they neglect the dynamics of long pipelines in the system. In fact, no published work on wave energy converters have considered the presence of long pipelines despite being a feature of many wave-powered RO system concepts [13, 51] and some electrical power producing system concepts [52]. For scale, for the electric power producing prototype plant built by Aquamarine Power, called Oyster 1, the bottom-mounted, flap-type WEC and the driven linear pump were placed 500 meters offshore while the turbine and electric generator was placed onshore; these two parts of the plant were connected by 500-meter-long, high-pressure and low-pressure pipelines [52]. Depending on the geography of the seabed, the pipeline may be anywhere between 300 and 1500 meters long [51]. With a WEC generating flow pulsations every three to ten seconds, these lengths of pipeline are on the same order of distance as the wavelength of pressure waves traveling in the working fluid (e.g., sea water and mineral oil having speeds of sound between 1500 and 800 m/s respectively). This condition for the pipeline flow may have important effects on plant performance and the control of pressure variation at the RO module.

The presence of a pipeline may not be necessary for all electrical power generating plants because the electrical generating machines might also be placed offshore and a set of undersea cables could transmit the electrical power that is generated. However,

the wave-powered RO systems must have at least one pipeline in the system. This is the case whether the pipeline is supplying pressurized feedwater to the RO module onshore or piping the freshwater product to shore from a RO module placed offshore. In both cases, the presence of the pipeline with the distributed inertive, resistive, and capacitive properties of the working fluid may have significant effects on the variation of pressure in the RO system. Therefore, models of pipeline dynamics should be incorporated into the modeling and design framework for these systems so that 1) the performance of the plant is modeled accurately and 2) the systems can be designed to meet the constraints on the RO system operation effectively.

1.3 Overview

Based on the review of the literature in Section 1.2, the work of this thesis addresses the following research questions about power take-off design.

1. How do alternative hydraulic PTO architectures perform on design metrics such as production and component size requirements, while also meeting constraints, such as limits on pressure and constraints on the rate-of-change in feed pressure?

2. What effect does a constraint on the rate-of-change in feed pressure of the RO process have on design metrics (e.g., component size and plant efficiency)?

3. What modeling techniques are appropriate for capturing the dynamic effects of pipelines in the system?

This work specifically explores the design oriented questions, questions 1 and 2, in the context of a system that co-produces freshwater and electrical power. This is to enable a more robust design then has been considered previously and that can truly be autonomous as it can meet its own electrical power demands. The schematic in Figure 1.8 illustrates a WEC/PTO system that is designed for co-production of electricity and potable water and is considered the baseline architecture throughout

this work. The PTO includes (1) a WEC-driven, hydraulic cylinder and check valve rectifier that together function as a pump, (2) an RO system comprised of the RO membrane module and an optional energy recovery unit (ERU) used to recover power from the high-pressure brine that would otherwise be throttled, (3) an electric motor-driven charge pump that resupplies seawater consumed in the RO process and provides an elevated pressure so that cavitation is avoided in the suction side of the WEC-driven pump, (4) an electric generator that is driven by a hydraulic motor and is used as a source of electrical power and a means of regulating the pressure at the RO feed inlet, and (5) hydraulic accumulators that give the system capacitance, reducing the pressure variation caused by the variations in flow rate from the WEC-driven pump.

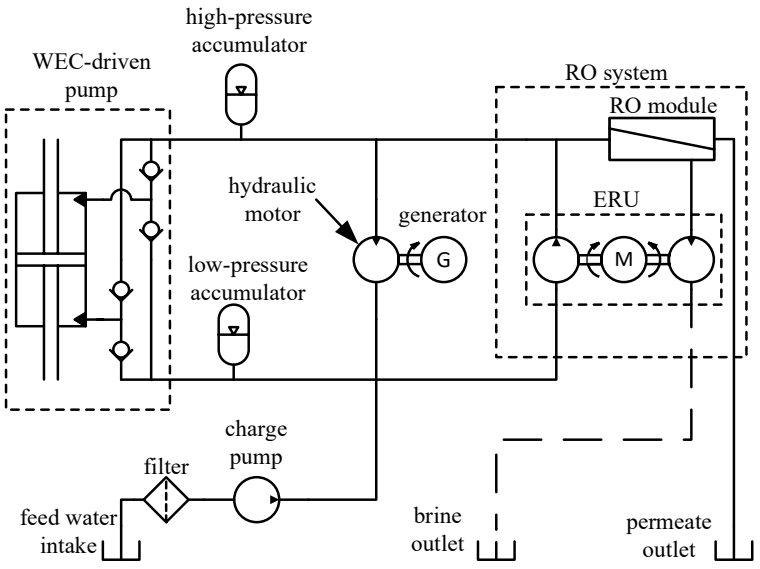

Figure 1.8: Simple wave-powered reverse osmosis desalination plant with co-production of electric power.

The aims of this work are addressed by three multi-objective design studies and a modeling study. Chapter 2 presents a design study that considers component sizing and yearly-averaged permeate production in the context of variable sea conditions. The

component sizing considered in this study includes (1) the sizing of the WEC-driven pump (specifically, the volumetric displacement) and (2) the sizing of the RO module (specifically, the total membrane area). Variations to the PTO architecture include variable displacement as a feature of the WEC-driven pump, variable membrane area as a feature of the RO module, and the configuration of the circuit with the hydraulic motor in parallel or in series with the WEC-driven pump and RO module. The study also considers an extension of the series-type architecture to include switch-mode techniques to form a switch-mode power transformer within the circuit. This study is performed using a computationally efficient approach that models the time-averaged system performance on the basis of discrete sea conditions and ignores the dynamics of the PTO.

Chapter 3 builds upon the findings of Chapter 2 by considering how varying the load on the WEC on a moment-to-moment basis, through load control, affects the mean power captured by the WEC in a discrete sea condition and on a yearly-averaged basis in the context of variable sea conditions. This study specifically examines how the limits of the PTO effect performance. The type of limits considered include the maximum load, minimum load, and the maximum rate the load can be adjusted. A model predictive control based machine learning scheme is developed to perform this study; the goal of which is to identify the absolute maximum performance that can be achieved without regard to practical control system implementation in a real system. The results of this study are applicable to both electrical power production from wave energy and wave-powered desalination.

Chapter 4 addresses the dynamics of the PTO in its design using a two-way coupled model of the WEC and PTO. This design study considers the sizing of the high-pressure accumulators and mean power loss in the context of meeting a constraint on the rate-of-change in RO feed pressure. Four PTO architectures are considered, including the baseline parallel-type, the parallel-type with dynamic pressure filters, and the series-type architecture. Pareto optimal designs are found for each architecture using grid studies. The Pareto fronts are compared to provide a rank-ordering of the architectures. The

design of the baseline architecture is also considered without regard for the pressure rate-of-change constraint to quantify what the cost of this constraint is on the design performance of the PTO.

To frame this work in the context of a concrete application, the work of Chapters 2, 3, and 4 will assume a specific WEC design and location for the system. Specifically, this work assumes the same WEC and site location considered by Yu and Jenne in [19].

Chapter 5 presents a study comparing pipeline modeling methods in wave energy systems. Three lumped parameter models and two distributed parameter models are implemented as part of a generic PTO system model with a prescribed, realistic WEC-driven pump flow rate. Parameters of the system, such as accumulator capacitance and pipeline length are varied across several design cases. The performance of each pipeline model is judged based on the comparison on resulting estimates of several design metrics across all design cases. The design metrics include power loss, pressure variation, and peak rate-of-change in the load pressure.

This work is reviewed and its conclusions are summarized in Chapter 6. Chapter 6 also provides conclusions made in view of the work as a whole and provides suggestions for future work.

Chapter 2

A Comparison of Power Take-Off Architectures for Wave-Powered Reverse Osmosis with Co-Production of Electricity

The content of this chapter was first presented in [60].

2.1 Introduction

This chapter introduces several proposed PTO architectures, and presents a study quantifying their potential design performance in terms of the annual average production rate of fresh water, the power density of the WEC-driven pump, and the installed capacity of the RO module.

A useful design metric for these systems is the levelized cost of water as examined in [29, 19, 61] (i.e., the cost of constructing and operating the system normalized by the water that is produced). However, this requires a suitable techno-economic model, which

is out of scope for this work. While the analyses in [29, 19, 61] include techno-economic models of similar systems, they do not include the effect of the PTO's component sizing on the costs of the system, other than the installed capacity of the RO module [29, 19]. Without a model including the effects of the PTO component sizing, there is no basis for combining the proposed design metrics in a single metric; therefore, the comparisons made in the work will made under the framing of a multi-objective optimization where the design of the system can trade merit between the objectives.

This work will assume the same WEC design and wave environments as is considered in [19]. This enables bench-marking and establishes a point of reference for comparing an architecture design performance on multiple design objectives. However, some additional work is required to establish values for the displacement of the WEC-driven pump and capacity of the RO module for the system in [19] in terms considered in this work. Furthermore, the performance results of the system in [19] do not account for limits to the pressure of the RO system. Although this was addressed by the work in [24] with the addition of a pressure relief valve, an updated estimate for the average annual freshwater production has not been produced. Therefore, the model used in [19] will be augmented to include the effect of a pressure relief valve and will be exercised to produce an updated estimate for its average annual production so that it can be compared to the PTO architecture proposed in this work.

This work is organized as follows. The proposed PTO architectures will be presented in Section 2.2. Then, the work to establish the design performance of the system design presented in [19] will be presented in Section 2.3. Next, the methods used to study the proposed PTO architectures are presented in Section 2.4. These methods include the mathematical models, the design optimization algorithm, and the method used to compare architectures to reference design. In Section 2.5, the results will be presented and discussed, including several example designs produced by the design optimization algorithm, results for the overall design performance of each PTO architecture, and comparisons between the design performance of each architectures. The comparisons

are made using, first, the performance of the system in [19] as a reference and, second, a reference design selected from the results of the design optimization algorithm used in this work. A set of conclusions about the choice in PTO architecture will be presented in Section 2.6.

2.2 Proposed Power Take-Off Architectures

The PTO architectures proposed in this work are motivated by two goals: maximizing the energy that is absorbed and transmitted to the RO membrane module to produce freshwater and maximizing the power density of the WEC-driven pump. The drawbacks of the baseline architecture shown in Figure 1.8 will be discussed along with proposed modifications that address these drawbacks. This discussion begins with how the design and operation of the baseline architecture affects wave energy capture and freshwater production and ends with a discussion of methods for improving power density.

The reaction forces placed on the WEC by the power take-off, referred to as the PTO load, serve an important role in determining the rate of wave energy capture by the WEC. Similarly, the pressure of the seawater fed to the RO module, along with the active surface area of the RO membrane, determines the rate of permeate production and the power it consumes. A drawback of the baseline system shown in Figure 1.8 is that, once the component sizes are fixed, the only variable available to modulate the load on the WEC and the production rate of the RO module is the pressure of the high-pressure rail. Both the power draw of the RO process and the power absorption of the wave energy harvesting process are solely dependent on this shared pressure level. For any given sea condition this would not be an issue since the pressure, displacement of the WEC-driven pump, and total membrane area in the RO module could be optimized in conjunction to maximize the system performance. However, sea conditions at a production site are variable and the system must perform in a variety of sea conditions.

The relationships between the system pressure in the PTO and (1) the power absorbed by the WEC and (2) the power consumed by the RO module are illustrated in Figure 2.1. The effect of the sea state and the effect of the size of the pump are illustrated by four separate curves. The average power absorbed by a WEC depends on the load that is placed on it by the PTO and has some maximum value. Different sea states offer different levels of power. Changing the pump displacement can shift the relationship between the pressure differential across the WEC-driven pump and power absorbed since the load on the WEC is the product of the pressure and displacement (plus losses). The effect of the total active membrane area, affected by the size and number of RO membrane elements comprising the RO membrane module is illustrated with two different curves. The permeate production rate of the RO process is approximately linear with respect to pressure, resulting in a quadratic relationship between the operating pressure and the power consumed. The production rate and power consumed scale proportionally with the active membrane surface area.

As suggested in Figure 2.1, the pressure offering maximum power absorption by the

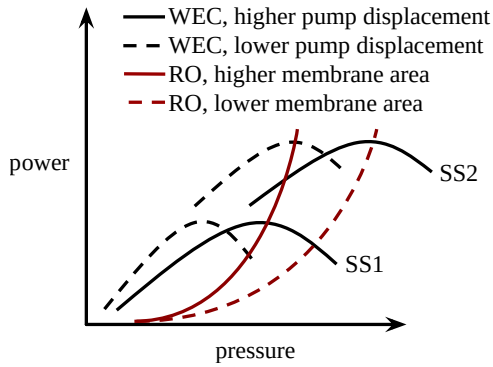

Figure 2.1: An Illustration of the relationships between the pressure differential across the WEC-driven pump and the average power absorbed by a WEC and the RO feed pressure and power consumed in RO process. Power absorption by the WEC is plotted for two sea states (SS1 and SS2) and two value for the WEC-driven pump displacement. Power consumed by the RO process is plotted for two values of total active membrane area.

WEC will not correspond to commensurate power consumption by the RO module in all sea states. However, if either the displacement of the WEC-driven pump or active RO membrane area is adjustable between sea states, these could be made to correspond. This motivates two potential features for the architecture of the PTO: (1) a WEC-driven pump with a variable displacement and (2) an RO system that can vary the active membrane area. Either of these approaches would provide an additional degree of freedom to the operation of the system and may provide greater performance across sea conditions.

Implementation of a variable displacement, WEC-driven pump instead of the fixed displacement pump is illustrated in Figure 2.2 as part of the baseline architecture. Note that the change from a fixed displacement pump to a variable displacement pump may require moving away from the linear cylinder pump architecture used by some PTOs (for example see [62]), to a low-speed, high-torque, rotary-type pump architecture like the design introduced in [63]. Alternatively, implementing the switch-mode system shown in Figure 2.3 provides the effect of a variable displacement pump displacement while not requiring any major change to the pump architecture. For this reason, a switch-mode pump may be a more economical choice. In the switch-mode system, the average rate of volume displaced to the high-pressure line is modulated by the duty cycle of the repetitive switching of the on/off switching valve (i.e., the proportion of time the valve is closed instead of open within a switching cycle).

Implementing a variable RO membrane area would consist of taking a portion of the pressure vessels in the RO module, which contain the RO membrane elements, out of operation or putting more into operation as the sea conditions change. Doing so changes the total active membrane area.

Sharing a common high-pressure rail between the WEC-driven pump, RO module, and hydraulic motor/generator brings about another disadvantage of the baseline system, which will be referred to as a parallel-type architecture. As mentioned above, the operating pressure of the RO module is constrained to pressures below 7 MPa or 8.3

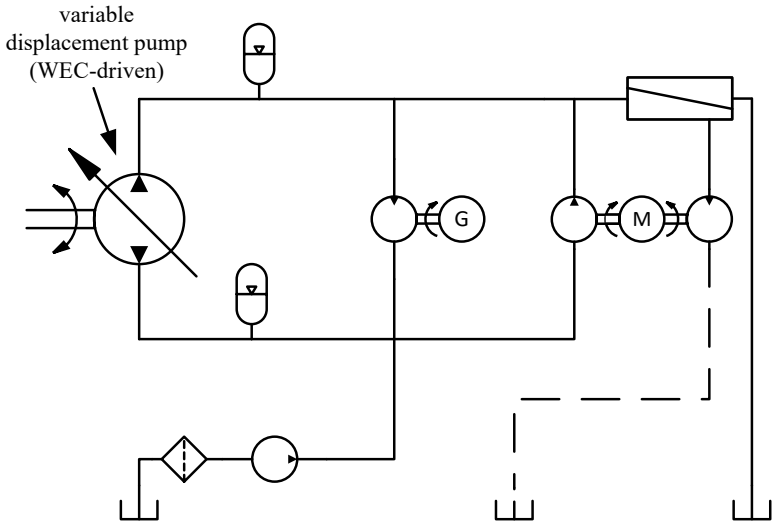

Figure 2.2: A parallel-type PTO architecture with a variable displacement, WEC-driven pump.

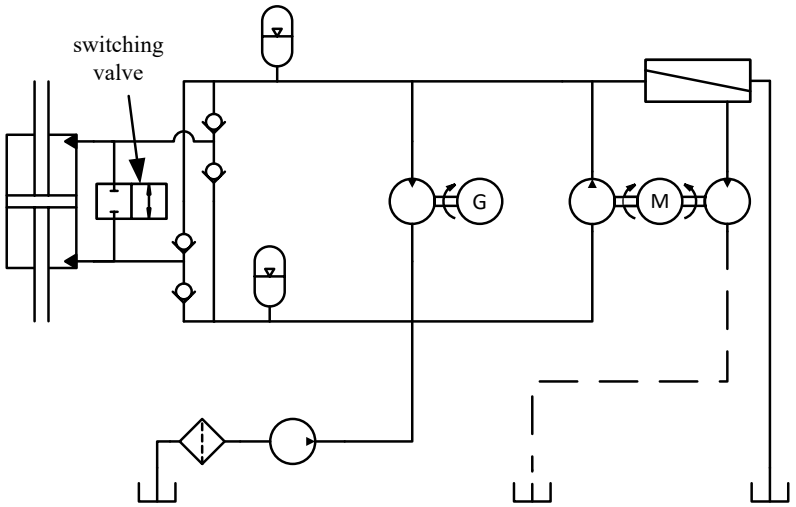

Figure 2.3: A parallel-type, switch-mode PTO architecture.

MPa (depending on the components selected). With a parallel-type architecture, the WEC-driven pump is limited to these same pressures. This is a relatively low operating pressure by conventional standards for hydraulic systems (where pressures of 20-40 MPa are common) and, therefore, the power density of the WEC-driven pump will be relatively poor. Since this is one of the most expensive components in the system, increasing its power density can have a significant impact on decreasing the cost of the plant as well as improving the ease of packaging components.

To accomplish a higher power density for the WEC-driven pump, a series-type architecture is proposed that places the electric generator's hydraulic motor in series with the WEC-driven pump and RO module, as shown in Figure 2.4. The load of the hydraulic motor driving the generator creates a pressure differential that sets the operating pressure of the WEC-driven pump above that of the RO module. At the same time, all of the flow from the pump is directed through the hydraulic motor and to the RO module, rather than being split between the two in the parallel-type architecture. This reduces the displacement required for the pump for a given power level, improving the power density. As with the parallel-type architecture, a series-type architecture can achieve the two degrees of freedom in the operation of the plant by including a variable displacement, WEC-driven pump, as illustrated in Figure 2.4, or an RO system with variable membrane area.

Another series-type PTO architecture, first proposed in [64], adds an on/off switching valve and check valve in the configuration shown in Figure 2.5 which is referred to as a switch-mode power transformer. This places a power transformer between the WEC-driven pump and RO module that can also generate electricity. Like the switch-mode scheme for variable displacement shown in Figure 2.3, switching of the on/off valve in the switch-mode power transformer modulates the average flow contributed by the WEC-driven pump to the RO module. When the valve is open, flow though the hydraulic motor is sourced from the high-pressure node at the WEC-driven pump. This

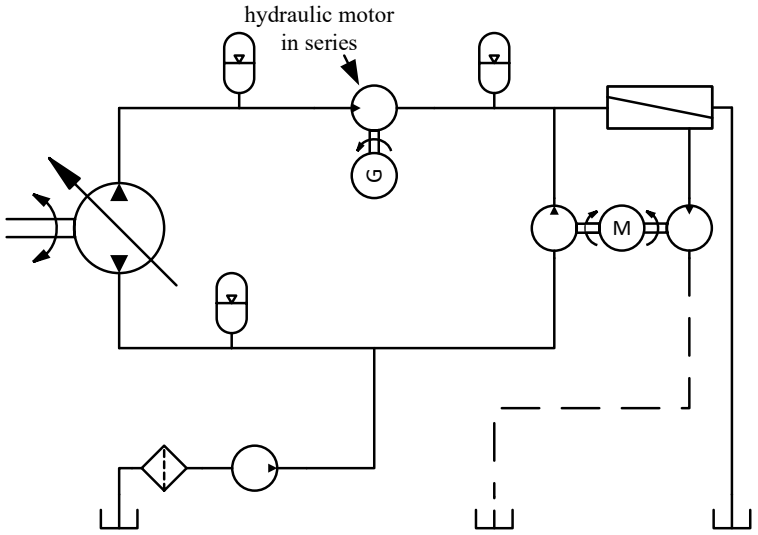

Figure 2.4: A series-type PTO architecture with a variable displacement, WEC-driven pump.

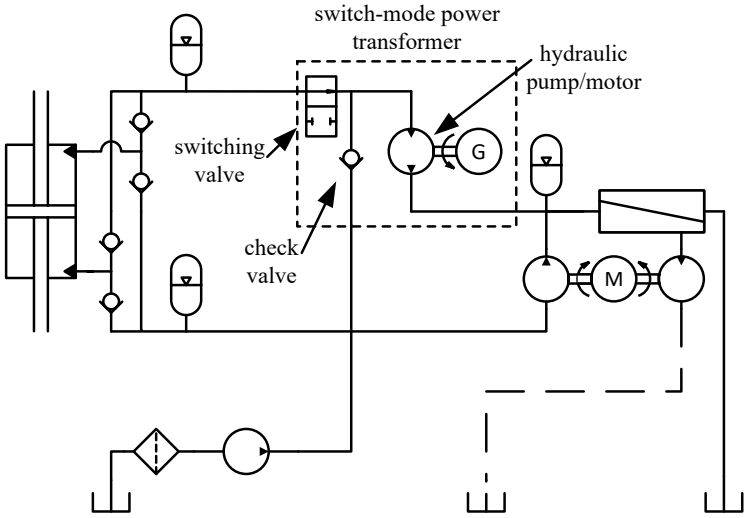

Figure 2.5: A series-type PTO architecture with a switch-mode power transformer.

accelerates the inertia of the rotating components of the hydraulic motor/pump [1] and generator, storing kinetic energy. When the valve is closed, flow is sourced from the low-pressure rail through the check valve. In this case, the inertia of the motor/pump and generator drive the hydraulic motor as a pump to drive flow to the RO module.

With the switch-mode power transformer in place, the WEC-driven pump can be downsized and operate at lower average flow rates and higher pressures than any of the other PTO architectures proposed above. This is so because the flow through the WEC-driven pump can be lower than the flow through the hydraulic motor/pump and RO module while delivering the same power as the pump in the other PTO architectures.

A fixed displacement, WEC-driven pump is suitable for this PTO architecture since the switch-mode power transformer already has the two degrees of freedom needed for independently managing both the wave energy harvesting process and the RO process; the average speed of the hydraulic motor/pump determines the RO feed flow rate, and the switching duty of the on/off valve controls the pressure at the WEC-driven pump.

2.3 Design Performance of the Yu and Jenne System as a Point of Reference

The system from [19] is examined in this section for the purpose of comparing its design performance with the PTO architectures proposed in Section 2.2.

Yu and Jenne evaluated the Oyster 1 designed and tested by the former Irish company Aquamarine Power for powering an RO process [19, 65]. The wave environment assume for their study is the based on data from a near-shore buoy at Humboldt Bay, CA [19]; the distribution for the probability of occurrence of sea conditions derived from this buoy are given in Figure 2.6. These data are derived using the methods based on work in [66].

[1] Because the hydraulic motor driving the generator is used as a motor and a pump in the switch mode power transformer, it will be referred to as the "motor/pump" throughout.

Significant wave height (m) \ Peak period (s)	5.22	6.38	7.54	8.7	9.86	11.02	12.18	13.34	14.5	15.66	16.82	17.98	19.14	20.3	21.5
0.25				0.02	0.03										
0.75	0.02	0.46	1.49	2.68	1.91	1.10	0.53	0.17	0.02						
1.25	0.01	0.59	4.11	5.56	4.48	2.74	1.28	0.67	0.33	0.07	0.02	0.02			
1.75		0.12	3.27	5.14	4.62	3.93	2.11	1.24	0.76	0.31	0.10	0.03			
2.25			0.92	5.25	3.68	4.14	2.87	1.31	0.84	0.42	0.20	0.08	0.02		
2.75			0.14	2.43	2.60	2.82	2.85	1.57	0.80	0.32	0.14	0.06	0.02		
3.25				0.45	1.54	1.47	1.96	1.42	0.79	0.32	0.11	0.04	0.02	0.01	0.01
3.75				0.05	0.49	0.63	1.08	1.01	0.63	0.29	0.10	0.05	0.02		
4.25					0.09	0.21	0.45	0.56	0.42	0.21	0.07	0.02	0.02		
4.75					0.02	0.08	0.12	0.26	0.27	0.19	0.07	0.02	0.01		
5.25						0.03	0.03	0.11	0.15	0.13	0.07	0.02			
5.75								0.02	0.07	0.05	0.05	0.02			
6.25									0.03	0.04	0.02	0.01			
6.75										0.02	0.02				

Figure 2.6: Joint probability of occurrence (percent) for sea conditions within bins centered at given values for significant wave height (0.5-meter bins) and peak period (1.6-second bins) (data from [19]). The transparency of the fill color follows the magnitude of values as a visual aid.

The component sizes and specifications for the pumping mechanism are not reported in the publication but their details have been obtained from the simulation files provided by the authors of [19]. The parameters used by that model are used to derive the WEC-driven pump displacement and installed RO membrane area for comparisons made in this work. Additionally, the results presented in did not account for the pressure limit of conventional RO systems and therefore they overestimate the potential annual production of the design. The issue of pressure limits was addressed later in [24] as part of a design study addressing pressure dynamics more generally but estimates for the annual freshwater production were not produced for that system. For a more accurate comparison in this study, the model used in [19] is modified to include a pressure relief valve set to limit the pressure at the RO feed inlet to 8 MPa. The estimated yearly average permeate production resulting from this modified model will serve as the reference for comparison rather than the results presented in [19].

The parameters for the pumping mechanism and RO module for the Yu and Jenne study were not reported in the publication; instead they have been obtained from the

simulation files shared by the study authors [19]. The analysis of the pumping mechanism used to derive a value for the WEC-driven pump displacement is presented in Section 2.3. The analysis of the RO module used to determine a value for the installed RO membrane area is presented in Section 2.3.

The model and simulations presented in [19] do not account for the pressure limits of conventional RO systems and, therefore, their results overestimate the potential annual production of the design. The issue of pressure limits was addressed later in [24] as part of a design study addressing pressure dynamics more generally, but estimates for the annual freshwater production were not produced for that system. For the comparisons made in this paper, the model used in [19] is modified to include a pressure relief valve set to limit the pressure at the RO feed inlet to 8 MPa. The estimated yearly average permeate production resulting from this modified model will serve as the reference for comparison, rather than the results presented in [19]. This modification to their model and the results the modified model produce are presented in Section 2.3.

Pump Displacement

Yu and Jenne [19] modeled the system as having the slider-crank pumping mechanism shown in Figure 2.7 with the parameters given in Table 2.1.

Table 2.1: Slider-crank parameters [19]

Parameter	**Value**	**Units**
Crank length, L_c	3	m
Rod length, L_r	5	m
Offset length, L_o	1.3	m
Piston area, A_p	0.18	m^2

In this design, the displacement of the pump is not constant with respect to position of the WEC. The displacement at a given position can be determined by multiplying the piston area by the ratio between the linear piston velocity and angular velocity of

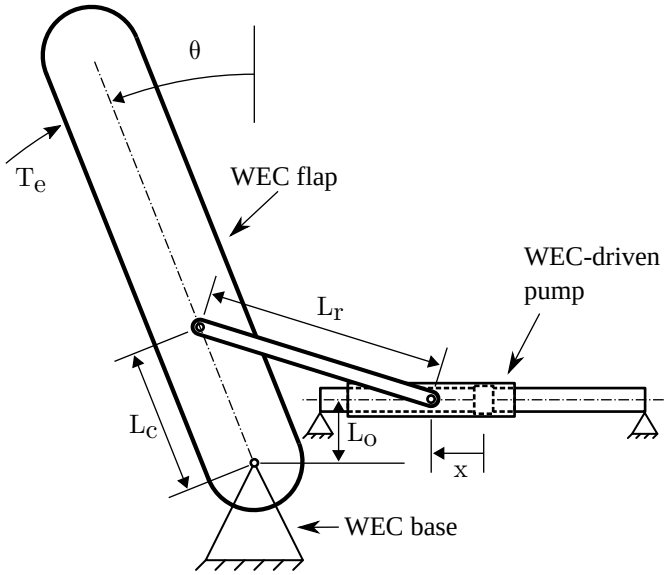

Figure 2.7: An illustration of the WEC-driven, slider-crank pump mechanism from [19]

the WEC. Equating the power input and power output of the mechanism reveals that this ratio is equivalent to the ratio between the torque on the crank and force on the piston. A static force analysis of the mechanisms gives the following expression for the displacement as a function of the WEC's position[2]:

$$D = A_p L_c \frac{\sin\left(\theta + \cos^{-1}\left(\frac{L_c\cos\theta - L_o}{L_r}\right)\right)}{\cos\left(\sin^{-1}\left(\frac{L_c\cos\theta - L_o}{L_r}\right)\right)} \tag{2.1}$$

The pump displacement with respect to the WEC motion about the upright position for this PTO design is 0.54 m^3/rad.

[2]This analysis would be carried out more efficiently using the instant centers method and Kennedy's rule but this formulation is adopted because this is how the WEC-Sim model from [19] has been formulated.

Reverse Osmosis Membrane Area

The permeate flow rate in Yu and Jenne's model was calculated using as the following relation:

$$q_{perm} = S_{ro} A_{perm} \left(p_f - p_{osm} \right) \tag{2.2}$$

where S_{ro} is the surface area of active membrane in the RO module, A_{perm} is a permeate flux coefficient for the RO module configuration, p_f is the pressure at the RO feed inlet, and p_{osm} is the osmotic pressure of the feedwater (i.e., the seawater) [19]. For the model used by [19], this relationship is parameterized with the product of the membrane area and permeate coefficient rather than specifying these parameters separately. The value used for this parameter is $5.56 \cdot 10^{-9}$ $m^3 s^{-1} Pa^{-1}$.

The value assumed for the permeate flux coefficient is based on the work in [24] and is representative of an RO module configuration with parallel sets of three 40-inch RO membrane elements in series. This work analyze this configuration of RO membrane elements using the design tool WAVE offered by FilmTec, which incorporates the concentration polarization effect and the effect of progressive concentration of the saltwater [67]. It found that a constant permeate flux coefficient is a reasonable assumption for the range of pressures considered [24]. The value found is $2.57 \cdot 10^{-12}$ $m^3 N^{-1} s^{-1}$. Using this permeate flux coefficient and the osmotic pressure assumed in both [19] and [24] (2.275 MPa), the equivalent value for the total membrane area of the RO module is 2162 m^2.

Modified Model with Pressure Relief Valve

A pressure relief valve was added to the Yu and Jenne model to account for a realistic pressure limit at the RO module and the model was exercised to give an updated estimate of the systems permeate production.

The pressure relief valve model added to the Yu and Jenne model considers a force balance in a poppet valve between a linear spring acting on the poppet and the static

pressure force on the valve face. Flow forces and inertia of the poppet are ignored. The flow is assumed to be turbulent and is modeled by the orifice equation. The orifice area is assumed to be proportional to the distance of the poppet from the valve seat. This model is parameterized by a valve coefficient, C and a cracking pressure, p_{cr}. The equation relating flow, q to the source pressure, p is

$$q = \frac{1}{C}\left(p^{\frac{3}{2}} - p_{cr}p^{\frac{1}{2}}\right) \tag{2.3}$$

The valve coefficient is determined by specifying a flow rate for a given cracking pressure and source pressure. For example, from a known limit pressure and peak flow rate, the valve can be designed to never allow the pressure to exceed that limit. This requires the cracking pressure to be set below that limit pressure.

The modified model was simulated using the same settings used by Yu and Jenne [19]. The simulation parameters for the pressure relief valve are a cracking pressure of 7.95 MPa and a valve coefficient of $1.41 \cdot 10^9$ $m^3 s^{-1} Pa^{-3/2}$. Figure 2.8 compares the results of the unmodified Yu and Jenne model and the model modified to include a pressure relief valve.

To recalculate the yearly average permeate production rate, the modified model was simulated using the same settings as in [19] and five different wave elevation signal realizations for each sea condition given in Figure 2.6. The average permeate production from each of the five simulations were averaged to give a single estimate. These are presented in Figure 2.9. The weighted-average production from these results is 1476 m^3/day. This is 17 percent less than the estimate of 1786 m^3/day presented by Yu and Jenne for the system without the pressure relief valve [19].

2.4 Methods

The remainder of this paper presents a design study that compares the optimal design performance of the PTO architectures proposed in Section 2.2. This section presents

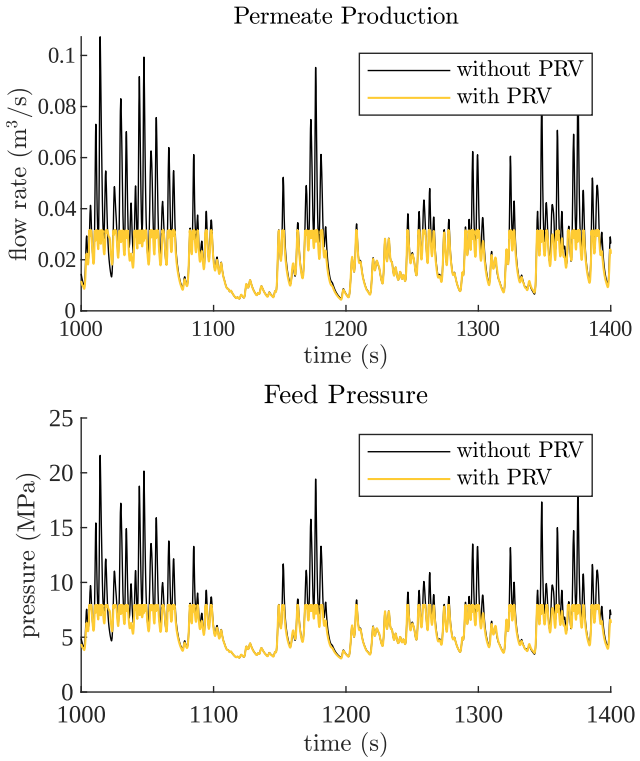

Figure 2.8: Simulation results for permeate flow rate (top) and RO feed pressure (bottom) with and without a pressure relief valve (PRV) for the sea condition having a 2.25-meter significant wave height and 8.7-second peak period.

the methods used for this design study.

The system is modeled by two-way coupled, static models of the PTO and WEC. Instead of using a dynamic model of the system and solving this numerically in the time domain, the flow rates and pressures in the system are assumed constant and a function of the average power input to the system. Hydrodynamic simulations of the WEC in the time domain are used to generate data sets, a priori, for each sea condition that relate the average power absorbed by the WEC to the constant magnitude reaction torque from the PTO. A continuous function is interpolated *in situ* from the *a priori* data sets and is coupled to the static model of the PTO. The power input to the PTO

Significant wave height (m) \ Peak period (s)	5.22	6.38	7.54	8.7	9.86	11.02	12.18	13.34	14.5	15.66	16.82	17.98	19.14	20.3	21.5
0.25				3	1										
0.75	299	384	428	447	442	426	395	361	321						
1.25	702	850	936	983	999	987	949	900	841	779	725	668			
1.75		1272	1360	1415	1439	1432	1399	1349	1290	1226	1166	1101			
2.25			1658	1711	1733	1727	1698	1663	1618	1566	1512	1450	1391		
2.75			1867	1913	1928	1921	1904	1888	1862	1822	1773	1713	1655		
3.25				2052	2061	2056	2055	2047	2035	2003	1963	1914	1862	1804	1748
3.75				2147	2156	2157	2155	2147	2144	2122	2092	2054	2014		
4.25					2224	2227	2232	2227	2208	2188	2170	2141	2114		
4.75					2269	2271	2277	2282	2265	2240	2221	2199	2176		
5.25						2303	2309	2319	2302	2283	2263	2240			
5.75								2344	2330	2307	2293	2269			
6.25									2347	2327	2311	2292			
6.75										2341	2326				

Figure 2.9: Average permeate production (cubic meters per day) by sea condition: Yu and Jenne design [19] with pressure relief valve. Fill color follows the magnitude of values.

results in a load on the WEC and *vice versa*. Given the models for the PTO presented in the following subsection, this two-way coupling of the static model is solved directly with no need for iterative solution methods.

The same WEC and wave environment assumed in [19] are assumed for this work. This WEC was chosen because it has been considered in other literature on ocean wave-powered RO desalination [11, 19, 24] and in modeling studies that included experimental validation [68]. Combined, these choices allow the results of this study to be compared to the design presented by Yu and Jenne [19]. The model used for the PTO is presented in Section 2.4.1. The model used for the WEC is presented in Section 2.4.2 along with validation of the model.

The design problem addressed by this study is treated as having multiple objectives. The data for the design performance of the PTO architectures consist of an estimated annual average rate of permeate production as a function of the maximum displacement of the WEC-driven pump and the installed membrane surface area in the RO module. These two component specifications, pump displacement and membrane area, serve the dual purposes of being objectives to be minimized and of being independent variables determining the permeate production. The optimal annual permeate production rate

for each combination of pump displacement and membrane area is determined by a single objective optimization of the system operation in each of the sea conditions given in Figure 2.6.

Because the overall design performance of each PTO architecture includes three objectives, there are no single optimal designs for each PTO architecture that can be used for rank ordering the architectures. Therefore, this design study uses a method of comparing the design performance to reference designs. A detailed formulation of the design problem, the method of obtaining the optimal permeate production as a function of component sizing, and the method of using reference designs as points of reference are presented in Section 2.4.3.

2.4.1 Power Take-Off Models

This section presents the models used to estimate the performance of the PTO. These models assume a static state of the system with constant flow rates and pressures and represent its average performance. This section begins with common aspects of the models for each PTO architecture, which include the behavior of the charge pump and the WEC-driven pump. The flow and pressure drop across the hydraulic motor/pump and the generation of electric power differ between the PTO architectures and are presented next. This section concludes with a specification of the parameters assumed for these models.

In all cases, the flow through the charge pump, q_c, is equal to the RO feed flow rate. The feed flow rate is the sum of the permeate and concentrate flow rates and is determined from the permeate flow rate, as in Equation 2.2, and a recovery ratio, Y, such that

$$q_c = \frac{q_{perm}}{Y} \tag{2.4}$$

The power consumed by the charge pump is given by

$$P_c = \frac{q_c p_c}{\eta_c \eta_m} \tag{2.5}$$

where p_c is the charge pressure, η_c is the efficiency of the charge pump, η_m is the efficiency of the electric motor driving it.

The pressure differential across the WEC-driven pump, Δp_w, is the difference between the high-pressure side of the pump, p_h, and the charge pressure:

$$\Delta p_w = p_h - p_c \tag{2.6}$$

The power absorbed by the WEC, P_w, is a function of the PTO torque and is determined by interpolating the data characterizing its time-averaged performance. The PTO torque is given by

$$T_c = \frac{D_w \left(p_h - p_c\right)}{\eta_w} \tag{2.7}$$

where D_w is the displacement of the WEC-driven pump per radian, p_h is the pressure at the outlet of the pump, and η_w is the combined efficiency of the WEC and WEC-driven pump.

The flow rate through the WEC-driven pump is a function of the power absorbed by the WEC and is given by

$$q_w = \frac{P_w \eta_w}{\Delta p_w} \tag{2.8}$$

The rest of the relations between pressure and flow rates are specific to each PTO architecture. For the parallel-type architectures, the high pressure at the WEC-driven pump is assumed to be equal to the RO feed pressure,

$$p_h = p_f \tag{2.9}$$

the pressure differential across the motor/pump is equal to the difference between the

RO feed pressure and the charge pressure,

$$\Delta p_{mp} = p_f - p_c \tag{2.10}$$

and the flow rate through the motor/pump is equal to the difference between the flow rates of the WEC-driven pump and the RO permeate,

$$q_{mp} = q_w - q_{perm} \tag{2.11}$$

For the series-type architecture without the switch-mode power transformer, the flow rates for the WEC-driven pump, the motor/pump, and permeate produced by the RO module are equal:

$$q_w = q_{mp} = q_{perm} \tag{2.12}$$

With the switch-mode power transformer, the switching duty, D determines the ratio between the flow rate coming from the WEC-driven pump and the flow rate through the hydraulic motor/pump such that

$$q_w = Dq_{mp} \tag{2.13}$$

Without the switch-mode power transformer, the pressure differential across the motor/pump is equal to the difference between the pressure at the WEC-driven pump and the RO feed:

$$\Delta p_{mp} = p_h - p_f \tag{2.14}$$

For the parallel-type architecture and series-type architecture without the switch-mode power transformer, the motor/pump only functions as a motor. In this case, the power generated by the hydraulic motor/pump and generator is

$$P_{gen} = \eta_{gen}\eta_{mp}q_{mp}\Delta p_{mp} \tag{2.15}$$

where η_{gen} is the efficiency of the electric generator, η_{mp} is the efficiency of the hydraulic motor/pump, q_{mp} is the flow rate through the hydraulic motor/pump, and Δp_{mp} is the difference in pressure between the inlet and outlet of the hydraulic motor/pump.

With the switch-mode power transformer, motor/pump alternated between motoring and pumping modes within a switching cycle. However, it is assumed that the power to drive the machine in the pumping mode comes from the stored kinetic energy of the rotor and that the electric generator is always in a mode of power generation. It is further assumed that throttling losses across the valve and switching losses arising from the compressible fluid volume switching between pressures are negligible. Under these assumptions, the electrical power generated is given by

$$P_{gen} = \eta_{gen} q_{mp} \left(D\eta_{mp} \left(p_h - p_f \right) - \frac{\left(1 - D \right) \left(p_f - p_c \right)}{\eta_{mp}} \right) \tag{2.16}$$

With 100 percent duty (i.e., $D = 1$), this becomes identical to Equation 2.15 applied for the series-type architecture without the switch-mode power transformer.

The parameters used in this study are given in Table 2.2. The permeate flux coefficient and osmotic pressure was selected to match the value used in Section 2.3 to analyze the system from [19]. The recovery ratio assumed matches the assumption from [24] on which the permeate flux coefficient is based. A charge pressure of 0.3 MPa was selected. The efficiency values assumed are typical for conventional components.

2.4.2 Wave Energy Converter Model

This section presents the dynamic WEC model that is used to inform the static, time-averaged characterization of the WEC performance that is coupled to the PTO models. This begins with a description of the equation of motion and the models for each force involved. The description of the model is followed by a specification of the parameters assumed for the model, how it was solved, and how it was used to inform the time-averaged characterization of the WEC. The section concludes with the validation of

Table 2.2: Power Take-Off parameters

Parameter	**Value**	**Units**
Permeate flux coefficient, A_{perm}	$2.57 \cdot 10^{-12}$	$m^3N^{-1}s^{-1}$
Osmotic pressure, p_{osm}	2.275	MPa
Recovery ratio, Y	0.25	-
Charge pressure, p_c	0.3	MPa
WEC and WEC-driven pump efficiency, combined, η_w	0.9	-
Hydraulic motor/pump efficiency, η_{mp}	0.9	-
Electric generator efficiency, η_{gen}	0.9	-
Charge pump efficiency, η_c	0.7	-
Electric motor efficiency, η_m	0.9	-

this model.

The equation of motion used to model the WEC is the Cummins equation, which uses an impulse response function to represent the time-history effects of the motion of ships and marine structures on the forcing by radiating waves [69]. Applied to an oscillating surge wave converter rigidly attached to the ocean floor, the Cummins equation is

$$(I + I_a)\,\ddot{\theta} + T_d + T_h + T_{rad} = T_e + T_{PTO} \tag{2.17}$$

where θ is the angular position of the WEC's flap (the position is taken to be zero when the flap is vertical and is positive when the flap leans toward shore), I is the inertia, of the WEC about its axis of rotation, I_a is the hydrodynamic added inertia, T_d is the torque from viscous damping (which is not considered in this study), T_h is the hydrostatic restoring force, T_{rad} is the torque due to waves radiating from the WEC, which are the result of the time history of the motion of the WEC, T_e is the torque resulting from the excitation by the wave elevation, and T_{PTO} is the reaction torque from the PTO's WEC-driven pump and the mechanical losses attributable to the WEC. The radiation damping torque, as suggested by Cummins, is represented by convolution

of an impulse response function such that

$$T_{rad} = \int_{-\infty}^{t} K\left(t-\tau\right)\dot{\theta}\left(\tau\right)d\tau \tag{2.18}$$

where $K\left(t\right)$ is the torque response on the WEC given a unit impulse in the angular velocity of WEC. Note that this assumes the amplitudes of the waves are small and therefore behave linearly. Since convolution integrals are computationally expensive, the radiation damping is instead modeled by a linear system which has the impulse response function approximating $K\left(t\right)$. The identification of this approximated model uses the algorithm presented in [70].

The wave excitation to the WEC is modeled as a linear frequency response that scales proportional with the wave amplitude. That is, given a sinusoidal wave profile passing the WEC, the excitation force is sinusoidal with the same frequency, an amplitude proportional to the wave amplitude dependent on frequency, and a shift in phase dependent on frequency. Realistic waves are not sinusoidal but can be represented by a trigonometric series. A finite series with frequency components is used such that

$$T_e\left(t\right) = \sum_{i=1}^{n} E\left(\omega_i\right) a\left(\omega_i\right) \sin\left(\omega_i t + \psi_e\left(\omega_i\right) + \psi_i\right) \tag{2.19}$$

where ω is the i-th frequency in the series, $E\left(\omega\right)$ is the frequency dependent coefficient of the excitation torque, $a\left(\omega\right)$ is the frequency dependent wave elevation amplitude, $\phi_e\left(\omega\right)$ is the frequency dependent phase shift between the wave elevation and the excitation force, and ϕ_i is the phase of the i-th frequency component in the constructed wave elevation signal, which is a randomly generated number between zero and 2π. Different wave elevation signals are generated by changing either the seed used for the random number generator or changing the discretization of the frequency domain. The discretization affects the quality of the signal, so random number generator seeds are used to construct unique wave elevation signals.

The wave elevation amplitude for each frequency component is calculated from an assumed power spectral density function, $S_w(\omega)$, describing realistic wave elevations, such that the amplitude of a frequency component is

$$a(\omega_i) = \sqrt{2S_w(\omega_i)\,\Delta\omega_i} \tag{2.20}$$

where $\Delta\omega_i$ is the bin width use for discretizing the frequency spectrum about the i-th frequency component. The Pierson-Moskowitz spectrum, which describes fully developed waves is used [33]. This is

$$S_w(\omega) = 5\pi^4 \frac{H_s^2}{T_p^4\omega^5} \exp\left(-\frac{20\pi^4}{T_p^4\omega^4}\right) \tag{2.21}$$

An equal-energy method is used to discretize the frequency spectrum, where the width of the bins is determined by the range of frequencies to be discretized and the number of frequencies making up the discretization such that the integral of the power spectral density function within each bin is equal. This method is preferred over a constant bin width because it generates a signal that does not repeat within any practical length of time. Details about implementation of this method are given in Appendix A, Section A.2.1.

The frequency response of the excitation torque and radiation damping impulse response function are determined by boundary-element-method-based frequency-domain potential flow solvers. For this study, the open-source solver NEMOH was used [71]. This program provides frequency dependent coefficients for the excitation force, added inertia, and a radiation damping impulse response function. The added mass and radiation damping impulse response function are inputs to the frequency-domain identification algorithm used to generate the linear system model of the radiation damping torque. The added mass, I_a, is equal to the high frequency asymptote for the frequency dependent added mass coefficients, when these are made is available [70].

The hydrostatic restoring torque is the torque due to the buoyancy less the torque

due to the weight of the flap such that

$$T_h = mgx_{cm} - V_{sub}\rho x_{cb} \tag{2.22}$$

where, for the torque due to weight, m is the mass of the flap, g is the acceleration due to gravity, and x_{cm} is the distance of the center of mass from the axis of rotation and orthogonal to the direction of gravity; and for the torque due to buoyancy, V_{sub} is the submerged volume of the flap, ρ is the density of the seawater, and x_{cb} is the distance of the centroid of the submerged volume from the axis of rotation and orthogonal to the direction of gravity. A simple model for the submerged volume, V_{sub}, assumes that the flap of the WEC is a thin, flat plate such that the submerged volume is

$$V_{sub} = L_t L_w L_{sub} \tag{2.23}$$

where L_t is the thickness of the flap, L_w is the width, and L_sub is the length of the submerged portion of the flap. A model for the submerged length of the flap, which assumes a high curvature of radius in the wave elevation compared to the motion of the flap, is given by

$$L_{sub} = \begin{cases} \frac{h+h_w(t)}{\cos\theta}, & \text{if } \cos\theta > h + h_w(t) \\ L_f, & \text{otherwise} \end{cases} \tag{2.24}$$

where L_f is the total length of the flap, h is the depth of the axis of rotation from the mean surface level, and $h_w(t)$ is the wave elevation as it deviates from the mean surface height. Like the excitation torque, the wave elevation is constructed from a discrete and finite trigonometric series such that,

$$h_w(t) = \sum_{i=1}^{n} a(\omega_i) \sin(\omega_i t + \psi_i) \tag{2.25}$$

The distances of the center of mass and centroid of the buoyancy from the axis of

rotation are given by

$$x_{cb} = \frac{L_{sub}}{2} \sin\theta \tag{2.26}$$

and

$$x_{cm} = \frac{L_f}{2} \sin\theta \tag{2.27}$$

With Coulomb damping, the torque from the PTO, T_{PTO}, is constant in magnitude, T_c, and opposes the motion of the WEC.

Simulations of the WEC with this Coulomb damping PTO were solved numerically using the forward Euler method. Convergence of the mean power absorption by the WEC was found with respect to the numerical solver time step, the length to the simulation, and the number of frequency components used to generate the wave elevation and excitation force. The simulations informing the characterization of the WEC were solved using a 0.01 s time step, a length of 2000 s, and with 1000 frequency components.[3] Initial conditions to the simulation were obtained using a 250 s simulation where the excitation force on the WEC was ramped from zero to its full value by multiplying the excitation torque by the following expression

$$\frac{1}{2} + \frac{1}{2}\cos\left(\pi + \frac{t}{T_{ramp}}\pi\right) \tag{2.28}$$

where t_{ramp} is the duration of the ramp period and the time t is zero at the beginning of the ramp period. This method was reported in [72] and is useful for avoiding excessive transient responses at the beginning of the simulations.

The parameters used in simulating the WEC are summarized in Table 2.3. Parameters of the WEC are summarized in Table 2.4. The results from ten simulations with different sets of random phases where averaged to produce the characterization of the average power absorption for the WEC in each sea state.

[3]These values were determined by convergence studies presented in Appendix A, Section A.2.

Table 2.3: Simulation parameters

Parameter	**Value**	**Units**
Start-up duration	250	s
Simulation duration (after start-up)	2000	s
Solver	fixed-step Euler method	-
Time step	0.01	s
Number of wave frequency components	1000	-
Random number generator seed (MATLAB function *rng()*)	3	-

Table 2.4: Wave energy converter (WEC) parameters

Parameter	**Value**	**Units**
WEC design	Oyster 1	-
WEC type	oscillating wave surge converter	-
Mass	127,000	kg
Moment of inertia	1,850,000	kg m^2
Length of flap from hinge	11	m
Center of mass from hinge	5	m
Width	18	m
Thickness	2	m
Hinge location above sea bed	2	m
Mean water depth	10.9	m

Model Validation

To validate the performance of this WEC model, its results were compared to results for the same geometry reported in [24] and experimental results reported in [68]. The results for each source used the same conditions in terms of sea conditions and PTO behavior and parameters. Both cases used a power take-off with linear damping, where the reaction force is proportional to velocity; this was replicated for the purpose of model validation.

The WEC with a linear damping PTO was tested with a damping coefficient of 50 $MNm{\cdot}s{\cdot}rad^{-1}$ and a sea condition having a significant wave height of 1.75 m and an energy period of 7 s (about 0.86 times the peak period). The experimental results in van't Hoff produced mean power absorption of 129 kW [68]. Yu and Jenne report that from ten simulations, each having unique wave elevation signal realizations, WEC-sim produced an average, mean power absorption of 147 kW with the 95 percent confidence interval between 137 kW and 159 kW [24]. The model developed in this paper was run for fifty different realizations and produced an average, mean power absorption of 147 kW with the 95 percent confidence interval between 128 kW and 166 kW. Although the confidence interval is wider for this model, the mean result matches the numerical simulation results from [24] and is within 12 percent of the experimental result obtained by van't Hoff.

2.4.3 Design Study Methods

A design problem is proposed, which includes the design objectives, a set of primary design variables, a set of operational parameters [4] that can be varied as a function of the sea condition, and constraints on the operation of the system. The design objectives include (1) maximizing the annual average permeate production, (2) minimizing the WEC-driven pump displacement, and (3) minimizing the total installed RO membrane area. The primary design variables are (1) the maximum WEC-driven pump displacement and (2) the total installed RO membrane area. The operational parameters are optimized for each sea condition and include (where applicable) (1) the nominal operating pressure at the control pressure node, (2) switching duty of the on/off switching valve, (3) adjusted pump displacement, and 4) active RO membrane area. The constraints placed on the operation of the system include (1) upper and lower limits to the pressure at the RO feed inlet (8 MPa and 4 MPa, respectively), (2) upper limit to the

[4] "Operational parameter" refers to a variable that is not fixed but can be adjusted as the plant operates, such as a control setpoint. This contrasts with "design variable" which refers to a variable that is fixed before the plant is installed and cannot be changed without changing or modifying components.

pressure at the WEC-driven pump outlet (30 MPa), and (3) a requirement that the system balances the electrical power consumption of the charge pump with electrical production by the generator in each sea condition. If these constraints are not met for a given sea condition, the system does not achieve operation for that sea condition.

The PTO architectures will be compared based on their performance in the three-design objective. These data are produced using the algorithm illustrated in Figure 2.10. The first stage of the design algorithm consists of optimizing the operational parameters for every combination of pump displacement and active RO membrane area in each sea condition. The second stage then accounts for cases where the PTO architecture allows for a variable pump displacement and/or variable RO membrane area. Every combination of pump displacement and active RO membrane area have already been evaluated in the first stage; therefore, the second stage searches those results for combinations having higher performance and a pump displacement and/or an active RO membrane area less than or equal to the combination being evaluated.

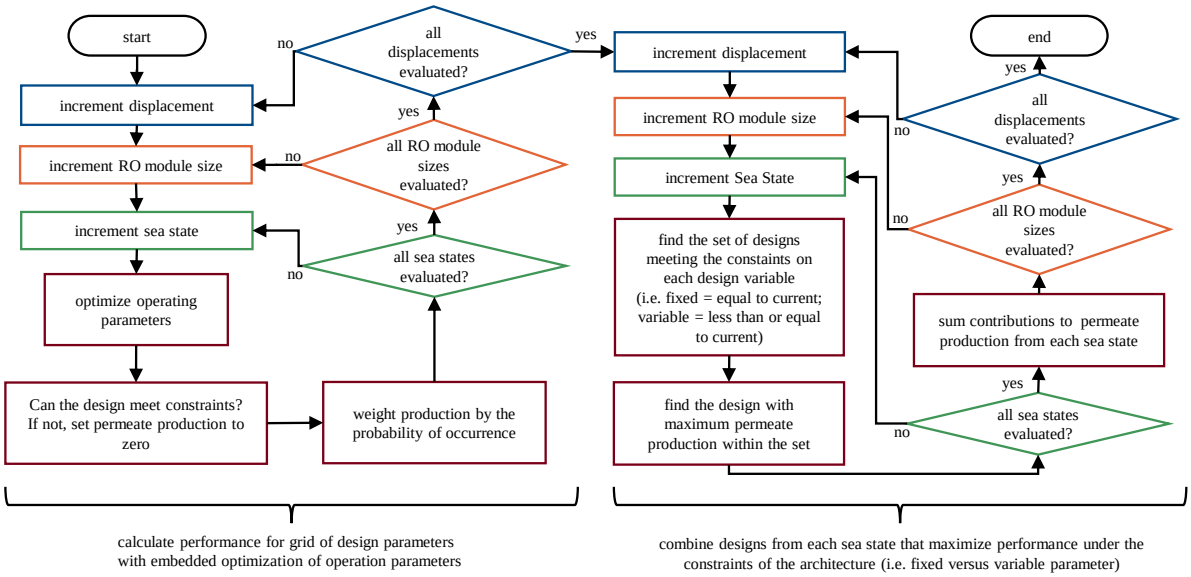

Figure 2.10: A design algorithm for optimizing PTO designs across a distribution of sea state

The results of the design studies are presented in Section 2.5 in the following ways. First, examples will be given for the operational parameters optimized for a selection of sea conditions. These are the operating parameters found for several selected combinations of PTO architecture, pump displacement, and installed membrane area. Second, results for the three design objectives are plotted for each PTO architecture in the form of contour plots with the annual average production as a function of the pump displacement and installed membrane area. Finally, comparisons between architectures are made using reference designs as points of reference. These reference designs are each specified by a single combination of pump displacement, membrane area, and permeate production. The comparison is made by evaluating the performance of each PTO architecture for the following three design cases:

- Case 1 – Find the lowest pump displacement that achieves the same permeate production as the reference design, while having an installed membrane area matching the reference design.
- Case 2 – Find lowest installed membrane area that achieves the same permeate production as the reference design, while having a pump displacement matching the reference design.
- Case 3 – Find the permeate production with a pump displacement and installed membrane area matching the reference design.

The reference designs used in the comparisons are based A) on the design from [19] as evaluated in Section 2.3 and B) on the baseline PTO architecture illustrated in Figure 1.8.

2.5 Results and Discussion

The following subsections present two comparisons of the design performance of the PTO architectures and a broad discussion about these results. Intermediary results, which

give a more detailed view of the data underlying these comparisons, are presented in Appendix B and include (1) results for the optimization of the operating parameters specific single PTO designs; this includes several select examples from the larger data set, and (2) the entire collection of results for the optimal annual permeate production rate as a function of pump displacement and installed RO membrane area; together these represent the objective space for this design problem.

For brevity, the PTO architectures are distinguished throughout this section using three-letter abbreviations that specify the type of architecture ("P" for the parallel-type architecture, "S" for series-type architecture, and "M" for the series-type architecture with the switch-mode power transformer), whether the WEC-driven pump has a fixed or variable displacement, and whether the active membrane area is fixed or variable ("F" for fixed and "V" for variable). For example, "P-FV" specifies the parallel-type architecture with a fixed-displacement pump and variable active membrane area.

The comparisons made of the performance for each PTO architecture use two reference designs, the specifications of which are given in Table 2.5. The first uses the design from [19] as a point of reference, based on the analysis presented in Section 2.3; this is referred to as reference design A. The second comparison assumes the parallel-type PTO with a fixed pump displacement (P-FF) with the performance obtained using the design algorithm and models presented in Section 2.4; this is referred to as reference design B.

2.5.1 Comparison to Reference Designs

The following results are two sets of comparisons made between the proposed PTO architectures. These use two reference designs as points of reference in the three design cases specified in Section 2.4.3.

Figure 2.11 presents the comparison of the proposed architectures using the reference design A as the point of reference. The most significant results from the three design cases are with improvement in the pump displacement for Case 1. With respect to this

Table 2.5: Reference design specifications

Design	**Pump displacement (m^3/rad)**	**Membrane area (m^2)**	**Annual average permeate production (m^3)**	**Source**
A	0.54	2162	1476	Design from [19] reevaluated in Section 2.3
B	0.23	3700	1518	Selected design with P-FF architecture

reference, the results for pump displacement show that (1) the parallel-type architectures offer 47–61 percent reduction in pump size, (2) the series-type architectures offer 60–74 percent reduction in pump size, and (3) the architectures with the switch-mode power transformer offer 87–92 percent reduction in pump size. Reduction in the total installed membrane area for design Case 2 is less significant but the results do show potential with the parallel-type architectures offering a 14–21 percent reduction. Of the series-type architectures, an advantage in installed membrane area is only achieved by the series-type architectures with a variable pump displacement (about 21 percent reduction). The trend in the results for permeate production in Case 3 are similar to the trend for the membrane area; the parallel-type architectures offer a 5–16 percent improvement in permeate production while only the series-type architectures with a variable pump displacement achieve an improvement in production (8 percent and 16 percent).

A strong Pareto improvement over reference design A is not demonstrated for the series-type architectures with a fixed pump displacement. However, this only highlights a drawback of this approach to comparing the architectures; inspection of Figures B.3a and B.3b show it is possible to simultaneously reduce the pump displacement and installed membrane area, while increasing the permeate production rate over reference design A. The pump displacement of reference design A is just not a favorable point of

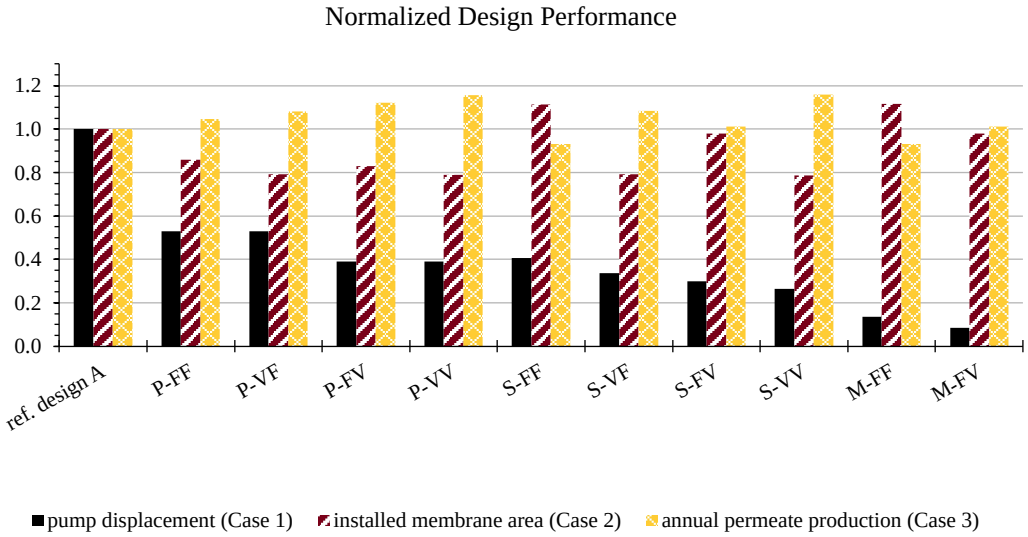

Figure 2.11: A comparison of PTO architecture performance normalized to the Yu and Jenne design [19] with a pressure relief valve (PRV) by design case. The references design has 0.54 cubic meter per radian pump displacement, 2162 square meter total installed membrane area, and 1476 cubic meter per day yearly average permeate production.

reference for demonstrating a strong Pareto improvement using this method of projecting the point of reference in the directions of the three axes.

While a strong Pareto improvement was not found relative to reference design A, reference design B offers a favorable point of reference for demonstrating strong Pareto improvement of the series-type architectures over the baseline parallel-type architecture. The results of this comparison are present in Figure 2.12. This comparison shows improvements in design performance in all cases except for the P-VF architecture which has nearly identical performance to the P-FF architecture. For Case 1, parallel-type architectures with a variable displacement pump offer a 25 percent reduction in pump size while the series-type architectures offer 29–49 percent and the switch-mode architectures offer 79–86 percent. For Case 2, parallel-type architectures with a variable active membrane area offer a 41 percent reduction in total installed membrane area while the series-type architectures offer 40–49 percent and the switch-mode architectures offer

44–48 percent. For Case 3, Parallel-type architectures with a variable active membrane area offer a 21 percent improvement in permeate production while the series-type architectures offer 16–38 percent and the switch-mode architectures offer 26–44 percent.

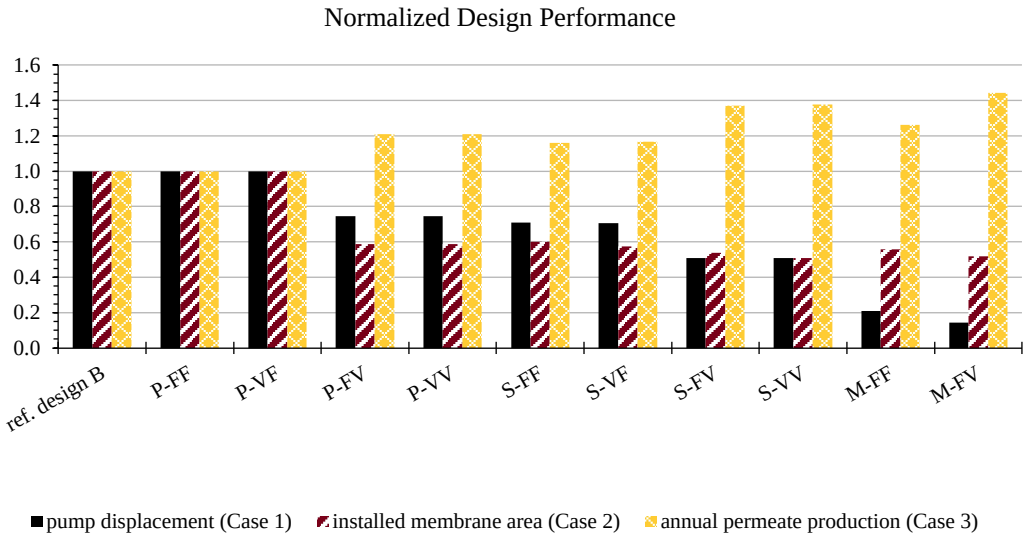

Figure 2.12: A comparison of PTO architecture performance normalized to a reference, a selected parallel-type PTO design with fixed displacement and fixed active membrane area (P-FF), by design case. The selected design has 0.23 cubic meter per radian pump displacement, 3700 square meter total installed membrane area, and 1518 cubic meter per day yearly average permeate production.

For assessing the significance of a variable displacement pump or variable active membrane area, it is more appropriate to compare the results within architecture types, between the fixed and variable counterparts. This analysis will focus on the comparisons made to reference design B. On the choice to include a variable pump displacement, the results show no significant effect to the design performance for any of the parallel-type architectures and only a minor effect on installed membrane area for the series-type architectures (about 5 percent reduction in Case 2). On the choice to vary the active membrane area between sea conditions, there are significant improvements regardless of the architecture. For Case 1, the pump displacement is reduced by 25–32 percent.

For Case 2, the parallel architecture achieve a reduction in installed membrane area of 41 percent while the series-type and switch-mode architectures achieve less significant reductions of 11 percent and 7 percent, respectively. Finally, for Case 3 improvements to the permeate production about 21 percent for the parallel-type architectures and 14–18 percent for the series-type and switch-mode architectures.

The results above assumed an upper bound for the pressure at the WEC-driven pump of 30 MPa. However, the effect of this upper bound is relevant to the detailed specification of components. While 30 MPa is widely achieved by state-of-the-art hydraulic systems, a limit of 20 MPa may be a more economical choice. Repeating the study presented above for an upper bound of 20 MPa at the WEC-driven pump outlet showed no significant effect to the design performance of the series-type architecture compared to reference design B, other than a 14 percent and 20 percent increase in the installed membrane area for the S-FF and S-FV architectures for design Case 2. However, the switch-mode architecture required significant increases in the WEC-driven pump size of 45 percent and 47 percent for the M-FF and M-FV architecture, respectively. The increase in installed membrane area is similar to the series-type architectures with increases of 19 percent and 18 percent, respectively.

2.5.2 Further Discussion

There are several significant findings from this design study. First, the results suggest that the benefits of a variable displacement pump are not significant despite providing a degree of freedom to the plant operation. A caveat is that this design study assumed constant displacement, pressure, and flow throughout the plant's operation in a given sea state. The constant reaction force on the WEC that results from that assumption is a Coulomb damping load strategy. Other strategies for loading the WEC, such as linear damping, could be enabled by a variable displacement pump despite pressures in the system being regulated to a constant nominal value. Those other load strategies may over perform the Coulomb damping strategy and prove some advantage for including

variable displacement as a feature of the WEC-driven pump.

Second, despite variable displacement not offering a significant improvement in system performance, the ability to vary the active membrane area did offer significant improvements. An important caveat is that this study assumed a continuously variable membrane area. Varying the active membrane area requires shutting down entire pressure vessels that each house a series of membrane elements and it is therefore a discrete process. Pressure vessels hold three to six membrane elements that each provide 30 to 40 m^2 of active membrane area. Varying the active membrane area in increments of 90 to 240 m^2 results in a change of 3–9 percent of the total installed area (assuming a total of 2750 m^2) and may limit performance gains. There are strategies for improving resolution of these kinds of digital system, as has been discussed for fluid power systems [73], such as including a variety in size or greater number of discrete elements. There are also drawbacks to increasing the number of times parts of the RO system are started up and shut down. This would add to the number of large magnitude stress cycles and would contribute to fatigue damage and wear. There is also an energy cost associated with startup and shutdown due to, for example, permeate needing to be rejected during this transition and membranes needing to be flushed out to equalize the osmotic potential across the membrane.

Third, there is a significant advantage in power density offered by the series-type architecture and the switch-mode power transformer. These architectures achieve higher pressures and lower flow rates at the WEC-driven pump by decoupling the pressures at the WEC-driven pump and the RO module and do this without adding significant components to the system. However, conventional hydraulic systems that achieve these higher pressures use oil as the working fluid. Using seawater with its lower viscosity may offer a challenge to lubricating the WEC-driven pump and the valves that are added for the switch-mode power transformer.

Finally, the static, time-averaged model used in this study, with its assumptions of constant pressure and flow rates throughout the system, is a relatively low fidelity

approach to modeling the system. This is especially notable considering that the performance of the reference design from [19] is estimated using dynamic simulations. The time-averaged models may have over-predicted the system's performance and inaccurately assessed constraints on its operation. Validation of these time-averaged models will be necessary for improving confidence in the conclusions from this work.

2.6 Conclusions

Several PTO architectures for wave-powered reverse osmosis were proposed. Variations in the architecture include the configuration of the system in a parallel-type or series-type arrangement, the addition of a switch-mode power transformer, and the ability to vary the WEC-driven pump displacement and active membrane area. These architectures were modeled under an assumption of constant pressure and flow in the system to provide a time-averaged estimate of their performance in a given sea condition. The time-averaged model of the PTO was coupled to a time-averaged characterization of the power absorbed by the WEC in a given sea condition as a function of the magnitude of a constant PTO load. A design study using this model considered the optimal performance of each architecture across a grid of values for the WEC-driven pump displacement and total installed RO membrane area. The operation of the plant was optimized in each sea condition within a large set describing the environment of Humboldt Bay, CA, giving an optimal, annual average rate of permeate production. The series-type architectures and the architectures with a switch-mode power transformer offered significant improvements to the power density of the WEC-driven pump with the switch-mode power transformer offering an order-of-magnitude improvement in power density; the series-type architecture without the switch-mode power transformer achieved improvements of 30–74 percent while the series-type PTO with the switch-mode power transformer achieved improvements of 70–92 percent. Under the

assumptions of the time-averaged model, variable displacement did not offer significant performance advantages for any of the architecture types. However, the ability to vary the active membrane area in different sea conditions from the total installed membrane area provided significant advantages in the design performance of the PTO with improvements in the range of 7–41 percent.

2.7 Data Availability

Data is available from the authors upon request. Custom software used is available at: `https://github.com/novaTehnika/2021-TimeAvePTOarchetectureStudy` (accessed 21 August 2023).

Chapter 3

Limits on the Range and Rate-of-Change in Power Take-Off Load: A Study Using Model Predictive Control

The content of this chapter was first presented in [74].

3.1 Introduction

In Chapter 2, several architectures for the PTO that follow a freshwater/electric-power co-production scheme were compared through the lens of a multi-objective design problem that considered production rates and component sizes as the performance metrics. This study included PTO architectures with either fixed or variable displacement WEC-driven pumps. A significant finding from this study is that variable displacement, as a feature of the WEC-driven pump, does not offer a significant improvement in the system's design performance over a fixed displacement. However, the scope of this finding

is recognized as being limited.

The limitation of the study is that it used time-averaged performance models of the system that assumed a constant load from the PTO on the WEC within a given sea state. This approach to load control is referred to as "Coulomb damping" due to the similarity to Coulomb's constant friction force model as opposed to the linear resistive damping often considered for WECs where the load is proportional to velocity. The average power absorbed by the WEC was characterized as a function of the Coulomb damping magnitude using a high-fidelity, hydrodynamic model of the WEC simulated in the time domain. The static, time-averaged power curve generated by this characterization of the WEC was then coupled to a static model of the PTO that assumed constant flow rates and pressures in the system. Under that modeling framework, the role of a variable displacement pump can only be to provide an additional degree of freedom toward achieving an optimal combination of the Coulomb damping magnitude and freshwater production rate. This modeling framework omits the potential for a controlled, moment-to-moment variation of the PTO load that enhances wave energy capture by adapting to the variations in the incoming waves.

A more robust comparison of PTO architectures should include their capacity for load control; it would be ideal to include an estimate for the upper bound in the performance that this capacity affords. Yet, this relies on the implementation of the load control scheme to direct changes in the PTO load. There are a variety of PTO load control schemes that have been proposed and a few studies comparing their performances [75, 76]. However, there is general dependence between the design of the PTO (with its non-ideal behavior and physical limitations) and the success of the load control scheme. Consequently, O'Sullivan and Lightbody [77] proposed that the model predictive control (MPC) framework be used to approximate an optimal PTO load control for the purpose of design studies that evaluate the design of a PTO.

Model predictive control is a popular optimal control method having origins in the

1970's [78]. The fundamental principles of MPC are the (1) use of a model to predict future behavior, (2) optimization of future control signals based on the model's performance predictions, and (3) the use of a receding time horizon for performing the optimization and implementing control signals. A significant advantage of model predictive control is that the optimization problem posed by the designer can include constraints on the system's behavior. One notable adaptation of MPC for wave energy conversion is that the typical control objective is to maximize either the energy absorbed by the WEC or the output of the PTO, while more traditional control system applications would aim to minimize tracking errors.

Model predictive control has been considered for the load control of WECs (see [79] for a recent, comprehensive review) and progress continues toward improving its implementations in terms of computational speed for real-time applications, prediction of future wave elevation, and the inclusion of system constraints [80]. Considering MPC as a means of providing optimal performance estimates in PTO design studies is supported by results in the literature, as suggested by O'Sullivan and Lightbody [77]. Coe et al. compared MPC to other load control methods and found it was the highest performing control method subject to a passivity constraint [76] (a PTO is passive when it only absorbs power rather than also feeding power back to the WEC). A complex conjugate control, which requires a reactive PTO load, was the only higher-performing method in their study; MPC was not tested in conditions where reactive PTO loads were allowed. When model predictive control was not subject to a passivity constraint, Hals et al. found that this control method was the highest performer [75].

The work presented here expands on the findings presented in Chapter 2 by examining the potential improvements to the average power absorption achieved with controlled, moment-to-moment variations of the PTO load. In addition, this work considers how practical limits on the PTO load variability affect power absorption. These constraints include (1) a maximum load, (2) a minimum load, and (3) a limit on the rate of load adjustment. For example, in the context of a constant-pressure-type PTO

with a WEC-driven pump having a variable displacement, these constraints translate to (1) the maximum displacement, (2) the minimum displacement, and (3) the speed that the pump can adjust the displacement. While constraints on the PTO load are not new (e.g., limits on the magnitude and the rate-of-change in the load are considered in [81, 82]), the constraints are assumed to be predetermined and are not studied for the effect of their inclusion. Instead, this work seeks to characterize how varying these constraints (i.e., their values) affects WEC performance. This makes the effect of their inclusion more transparent and can inform objectives in the design of PTOs (e.g., how responsive they are and what range of loads can be achieved).

As limits to the scope of this work, the study enforces the passivity of the PTO (i.e., power only flows in the direction, from the WEC to the PTO) and the continuity of the PTO load. The types of PTO load behavior being excluded from this study are (1) discrete PTO load changes, as in latching and declutching [83, 84, 85, 42], and digital, multi-chamber pumps [50, 86] and (2) reverse power flow, as seen with complex conjugate control. The types of hydraulic PTO architectures that are captured by this study are (1) constant-pressure-type PTOs with variable displacement WEC-driven pumps, (2) variable-pressure-type PTOs with fixed displacement WEC-driven pumps, and (3) variable-pressure-type PTOs with variable displacement WEC-driven pumps.

The implementation of MPC in wave energy conversion studies has typically framed the optimization as a quadratic programming problem, which requires discretized, linear system models [76, 87, 88, 81, 82]. In these cases, computational efficiency becomes a major concern for real-time control and is often traded off with performance. In contrast, this present study has no need for real-time implementation and, therefore, uses the same high-fidelity, nonlinear time domain model in the model predictive control as is used for simulating the 'true' system. The aim here is to estimate the upper bound in performance, not to achieve a practical, real-time control scheme.

In keeping with the study presented in Chapter 2, this work considers the Oyster 1 WEC and uses the historical data for the occurrence rate of sea conditions near

Humboldt Bay, CA, given in Figure 2.6, to weight average power capture performance across sea condition and provide estimates for annual average performance.

The remainder of this report is structured as follows. The following section, Section 3.2, presents the methods of the study, consisting of the dynamic model used for simulating the WEC, the implementation of model predictive control, and the structure of three design studies. This is followed by a presentation of the results from these three design studies in Section 3.3. Section 3.4 presents a discussion of the results. Conclusions drawn from this work and suggestions for future work are given in Section 3.5.

3.2 Methods

The methods for this work consist of three parts: the system model, the implementation of the model predictive control for the PTO load (forces between the WEC and PTO), and the structure of the design studies. The design studies for this work consider the effects of design requirements for the PTO on the average power absorption by the WEC using a constrained optimization of the PTO load on the WEC. Specifically, the design studies account for limits on the range of the PTO load and limits to the speed of load adjustment. These are implemented as constraints on the PTO load in the optimization problem within the model predictive control algorithm. In this work, the 'true' system and predictive model are the same time domain model simulating the hydrodynamics of the WEC. The hydrodynamic WEC model is presented in Chapter 2, Section 2.4.2. This studies implementation of model predictive control is presented in Sub-section 3.2.1. The methodologies of the design studies are presented in Sub-section 3.2.2.

3.2.1 Model Predictive Control

This work assumes the PTO load as the control signal generated by the model predictive control. The passivity of the PTO is enforced by defining the PTO load as the magnitude of the PTO's reaction force on the WEC, which opposes the WEC motion. Given that

the PTO load is a function of continuous states within the PTO system (e.g., the position of the displacement adjustment mechanism in a variable displacement pump or charge state of hydraulic accumulators), the PTO load is formulated as being continuous in the model predictive control; as such, the PTO load control signal is implemented as a linear interpolation between the discrete control updates rather than being held constant. For the flap-like OWSC device, the reaction force from the PTO is a torque on the WEC.

The formulation of the PTO load for optimization in the model predictive control framework is illustrated in Figure 3.1. In the model predictive control framework, the system has some history in the past, establishing the system state, and a future that will be determined based on future choices for the PTO load. At a given time, t_o, the algorithm is tasked with producing an optimal choice for the PTO load, $T(t)$, over the next control interval, $t = [t_o, t_o + \Delta t_c]$. That decision is based on predictions of the system behavior over some prediction horizon, $t = [t_o, t_o + t_p]$. To limit the size of the variable space, n discrete control points in time, $t = t_o + i\Delta t_c$ (where $i = 1, 2, \cdots, n$), are distributed equally throughout the control horizon, $t = [t_o, t_o + n\Delta t_c]$, distinguishing n control intervals. The PTO load at each control point, $T(t_o + i\Delta t_c)$, serves as a single variable within a constrained, multi-variable optimization problem, with the PTO load assuming a constant slope (i.e., the first derivative with respect to time) between control points, T_i'. After the optimal PTO load is determined for this control horizon, the system implements the PTO load for the immediate control interval, $t = [t_o, t_o + \Delta t_c]$. The system then evolves until the end of the control interval, $t = t_o + \Delta t_c$, and the process is repeated to predict the optimal PTO load over the new control horizon and determine the load to be implemented for the next control interval.

As illustrated in Figure 3.1, the PTO load is specified as being constant after the final control interval to complete the prediction horizon. In this work, the prediction horizon has been specified as being longer than the control horizon by 1.5 times the control period; that is, $t_p = t_c + 1.5\Delta t_c$. The intent of this practice is to provide additional influence of future system behavior on the selection of control inputs at a

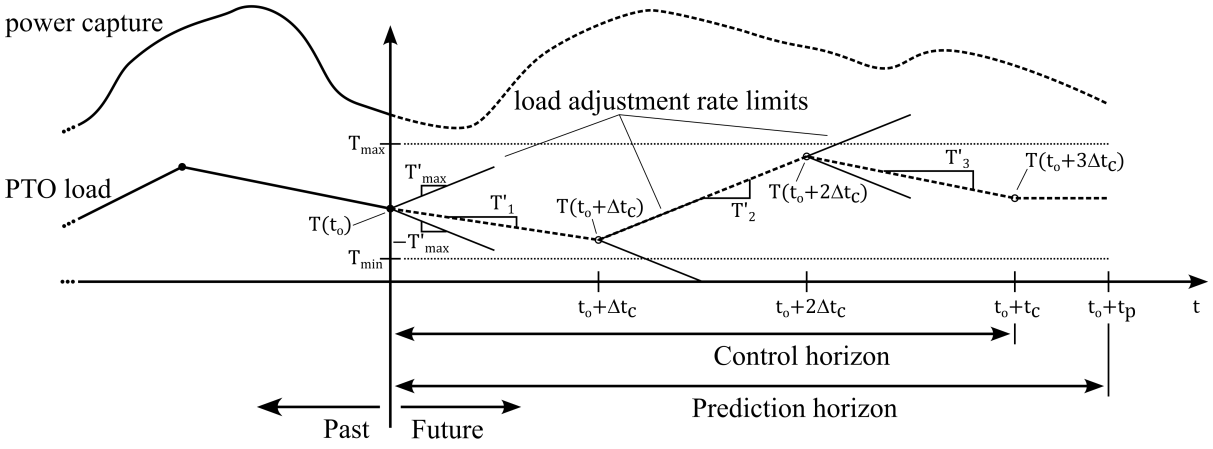

Figure 3.1: Illustration of the PTO load signal formulation for constrained optimization within the model-predictive control algorithm. In this example, the control horizon is three times the control update period.

lower computational cost than adding to the number of control points; this assumes that the computation of the system behavior over the interval $t = [t_o + t_c, t_o + t_p]$ is cheaper than the added dimensionality of the variable space in the optimization.

Limits on the PTO load are illustrated in Figure 3.1 as the maximum load, T_{max}, the minimum load, T_{min}, and a maximum magnitude for the rate-of-change in the PTO load, T'_{max}. Consequently, the optimization problem is as follows: select the variables $T\left(t_o + i\Delta t_c\right)$ that maximize the average power captured over the interval $t = [t_o, t_o + t_p]$, subject to the constraints $T_{min} \leq T\left(t_o + i\Delta t_c\right) \leq T_{max}$ and $|T'_i| \leq T'_{max}$.

The nonlinear, constrained optimization implemented in this work uses the interior-point method, as implemented by the function *fmincon()* provided with the computing software MATLAB. This algorithm requires initial values. The initial values provided for the start of the computations are all equal and are the average of the minimum and maximum torque; that is, $T\left(t_o + i\Delta t_c\right) = 0.5\left(T_{max} + T_{min}\right)$. This places the initial values at the center of the variable space meeting all constraints. Going forward from the first control update, the initial values provided to the optimization algorithm are

the optimal results from the prior control update. The initial value for torque at the end of each new control horizon is set equal to the initial value of the second to last control update period; that is, $T\left(t_o + n\Delta t_c\right) = T\left(t_o + \left(n-1\right)\Delta t_c\right)$. This follows from the assumed constant PTO load over the interval $t = [t_o + t_c, t_o + t_p]$.

Surrogate variables are used in place of the constraints given above. These serve as more practical descriptors of the PTO performance requirements and serve as the parameters varied in the design studies that follow. The minimum fractional load, f, is defined as a surrogate for the minimum load:

$$f = \frac{T_{min}}{T_{max}} \tag{3.1}$$

The minimum transition time between the minimum and maximum load value, t_L, is defined as a surrogate for the maximum rate-of-change in the load:

$$t_L = \frac{T_{max} - T_{min}}{T'_{max}} \tag{3.2}$$

3.2.2 Design Studies

Three design studies are presented in this work. The first varies the parameters of the model predictive control (the control update period, Δt_c, and the length of the control horizon, t_c) to determine their effects on the performance and to identify suitable values to be used in the second and third studies. This study only considers the performances of the WEC and PTO in a single sea state. The second and third studies vary values of the constraints on the PTO load to determine their effects on the performance.

The second study only considers the performance of the WEC and PTO in a single sea state, while the third study considers the yearly-average performance using historical data from Humboldt Bay, CA to weigh the performances from 114 distinct sea states, as presented in Figure 2.6. The constraints on the PTO load, as discussed above, include (1) the upper limit to the PTO load, T_{max}, (2) the lower limit to the PTO load, as a

fraction of the upper limit, f, and (3) the limit to the rate-of-change in the PTO load, as the minimum time required to adjust the load between extremes, t_L. The second study varies all three constraints while the third study assumes a specific value for the limit to the rate-of-change based on the results of the second study.

Results from the second and third studies are compared to results where Coulomb damping is used. The Coulomb damping results represent two cases. First, for a given maximum PTO load, the magnitude of the Coulomb damping is identical to the maximum load ('fixed Coulomb damping'). That is, $T(t) = T_{max}$. Second, an optimal choice for the Coulomb damping magnitude is made, subject to the same constraints as the model predictive control ('optimal Coulomb damping'). The optimization problem is posed as follows: select T_c, for which $T(t) = T_c$, maximizing the average power captured over the simulated time interval subject to the constraint $T_{min} \leq T_c \leq T_{max}$.

3.3 Results

The results of the three studies performed in this work are presented below. These include (1) a study on the performance of the MPC algorithm as a function of its parameters, namely the control update period and the length of the control horizon, (2) a study of the average WEC power absorption in a single sea state as a function of PTO load constraints, namely the maximum torque, the minimum fractional load, and the minimum load transition time, and (3) a study of the weighted average power absorption for the sea states presented in Figure 2.6, as a function of the maximum torque and the minimum fractional load. All results represent performance in an identical realization for the wave elevation in each given sea state. The results exclude a 250 s start-up duration and are averaged over 500 s of simulation time in the first study and 2000 s of simulation time in the second and third studies.

3.3.1 MPC Algorithm Parameter Study

Three cases are examined for a study on the MPC algorithm parameters, with each assuming different values for the PTO load constraints. The results presented in Figure 3.2 assume 5 MNm as the maximum torque, 0 as the minimum torque, and 5 s for the minimum transition time between the minimum and maximum torque. The other two studies assume the same except for a higher minimum torque of 3.75 MNm for results presented in Figure 3.3 and a longer control horizon of 20 s for the results presented in Figure 3.4. Each case assumes the same sea conditions, a significant wave height of 1.25 m and a peak period of 7.5 s.

The results are presented as contour plots with the contour lines being interpolated from a 10-by-10 grid of data points. Grid values are in the range of [3, 30] s for the length of the control horizon and [0.5 s, 3 s] for the control update period and are evenly spaced on a base-10 log scale. Because the control horizon is composed of a series of control update periods, its length is rounded up to the nearest integer multiple of the control update period length. In each case, data are missing for the corner conditions with a control horizon of 30 s and a control update period of less than 0.75 s; for these values, the calculations failed to complete within the time allotted for the computing resources.

In Figure 3.2, the performance of the WEC at absorbing energy is maximized near a control update period of 0.75 s and a control horizon time of 5 s (the maximum points from the grid study are 0.745 s and 6.46 s, respectively). In Figure 3.3, the maximum grid value is located at (0.61 s, 5.0 s). In Figure 3.4, it is (1.35 s, 10.78 s). Despite the differences in the location of the maximum grid value, the power capture results at these locations within each dataset are within 4 percent. This suggests that PTO load constraints do not have a significant coupling effect with the parameters of the model predictive control algorithm near these choices and that 0.75 s and 5 s for the update period and control horizon are suitable for the following studies.

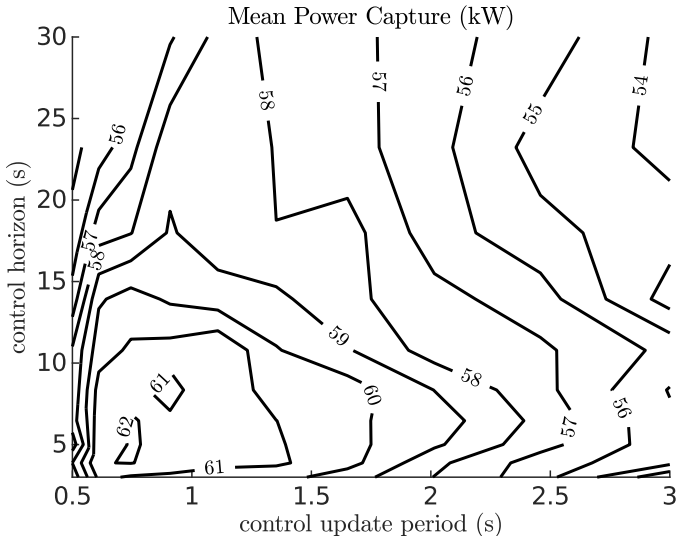

Figure 3.2: Model predictive control algorithm parameter study results: mean power capture assuming $T_{max} = 5$ MNm, $T_{min} = 0$, and $t_L = 5$ s.

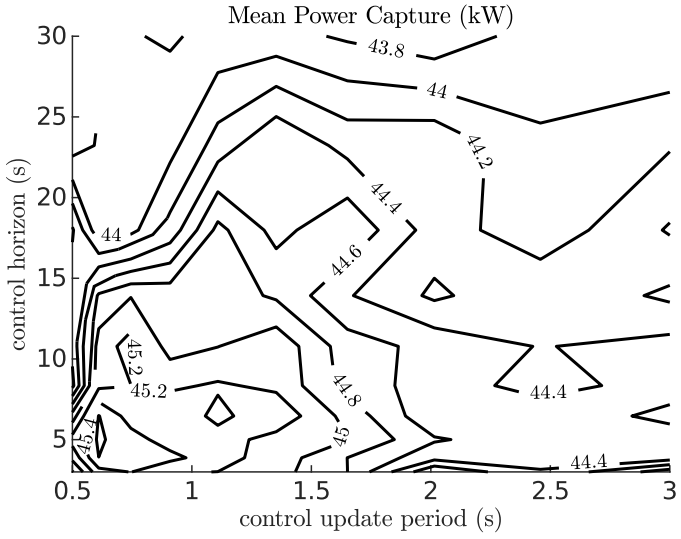

Figure 3.3: Model predictive control algorithm parameter study results: mean power capture assuming $T_{max} = 5$ MNm, $T_{min} = 3.75$ MNm, and $t_L = 5$ s.

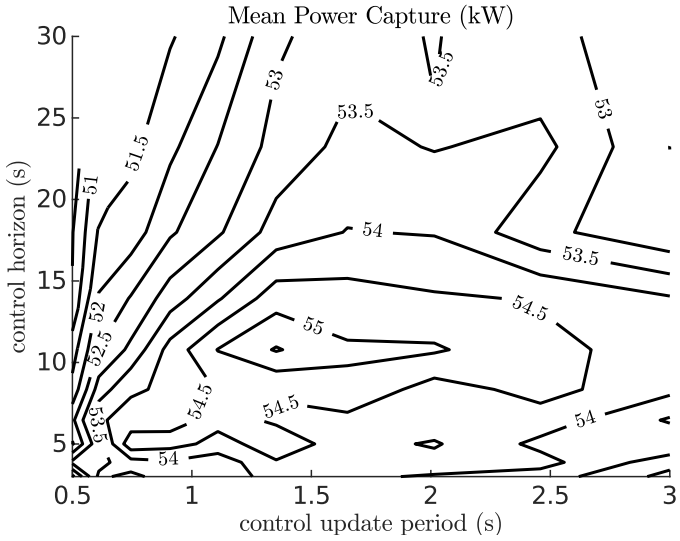

Figure 3.4: Model predictive control algorithm parameter study results: mean power capture assuming $T_{max} = 5$ MNm, $T_{min} = 0$, and $t_L = 20$ s.

The length of time required to perform the computations for the entire optimized and simulated time of 500 s was recorded for the case presented in Figure 3.2. These data are presented in Figure 3.5 and are based on the use of 3 processor cores on an AMD EPYC 7302P with 16 Gigabytes of RAM available and with the MATLAB function *fmincon()* executing function evaluations in parallel. Generally, the computational cost of the algorithm increases with an increasing time horizon and decreasing control update period as both increase the number of control points, n, being optimized in the MPC algorithm, and with a longer control horizon increasing the length of the simulations performed in evaluating the objective function. The compute time is on the order of tens of hours, which is about two orders of magnitude higher than the simulated time of 0.14 h (500 s).

3.3.2 Load Constraint Study: Single Sea State

The second study considers the same single sea state as in Section 3.3.1 (a significant wave of 1.25 m and a peak period of 7.5 s) but evaluates the influence of the maximum

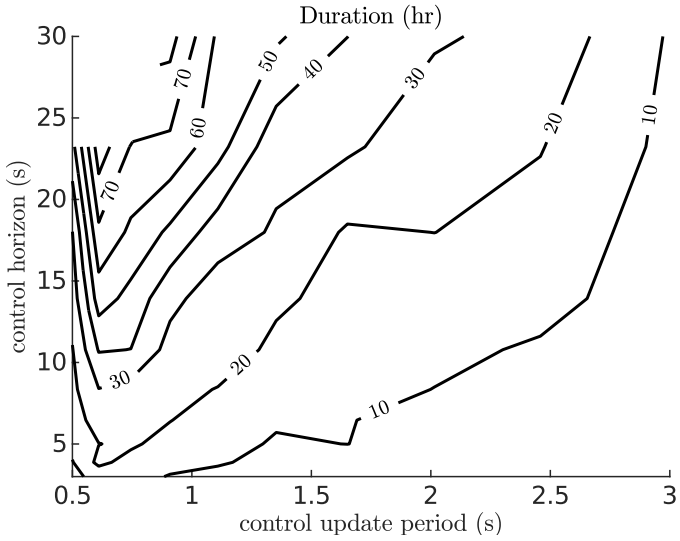

Figure 3.5: Model predictive control algorithm parameter study results: time consumption of the MPLS algorithm assuming $T_{max} = 5$ MNm, $T_{min} = 0$, and $t_L = 5$ s.

and minimum torques and the minimum load adjustment time on the WEC power absorption. The control update period and control horizon used for this study are 0.75 s and 5 s, respectively, based on the results of Section 3.3.1.

The results are plotted separately for four minimum fractional load values: 0, 0.25, 0.5, and 0.75 in Figures 3.6, 3.7, 3.8, and 3.9, respectively. Therefore, in each case, the mean power absorbed by the WEC is plotted against the maximum PTO torque and minimum load transition time. These results are compared against the performance of the WEC with Coulomb damping under the two conditions described in Section 3.2.2.

The power capture performance results are monotonic with respect to the minimum fractional load and the minimum load adjustment time but not with respect to the maximum load in all cases. Minimum load fraction values of 0 and 0.25 (Figures 3.6 and 3.7) provide a monotonically increasing power capture, within the tested values; however, with minimum load fractions of 0.5 and 0.75 (Figures 3.8 and 3.9), the mean power capture declines at very high values for the maximum torque. This trend is evident for the optimal Coulomb damping case as well.

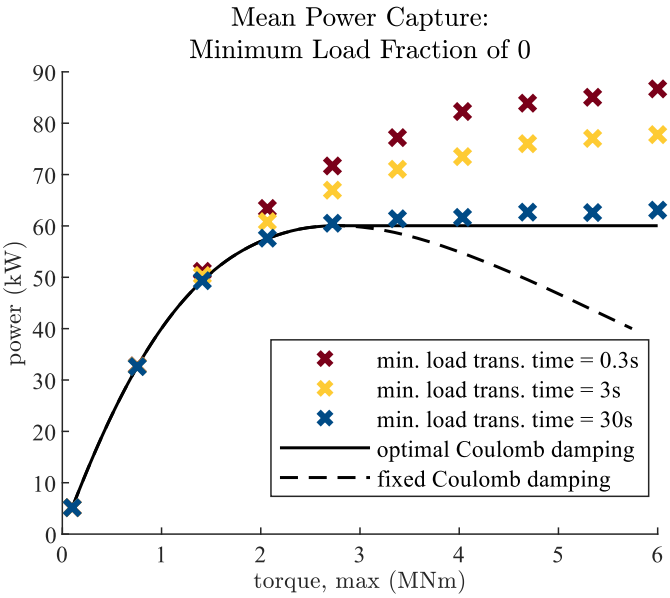

Figure 3.6: PTO load constraint study results: mean power capture with a minimum load fraction of 0.

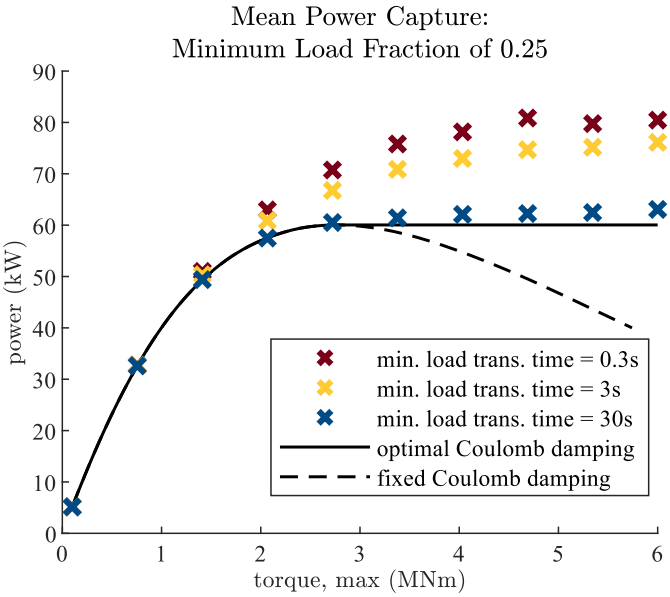

Figure 3.7: PTO load constraint study results: mean power capture with a minimum load fraction of 0.25.

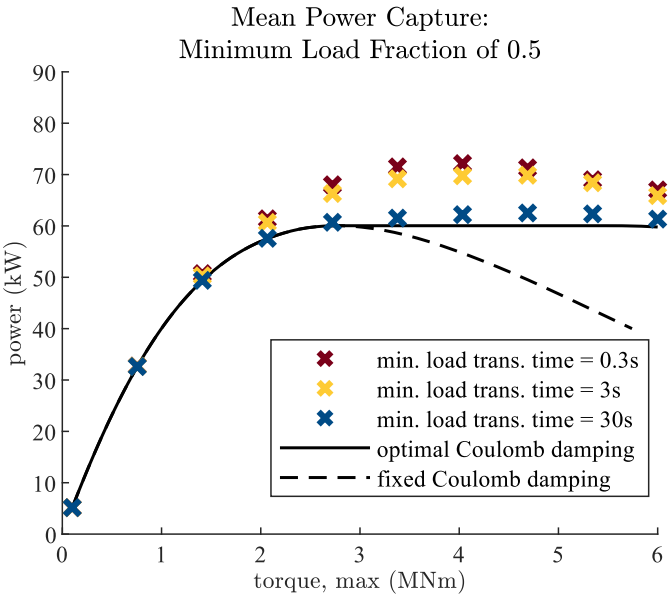

Figure 3.8: PTO load constraint study results: mean power capture with a minimum load fraction of 0.5.

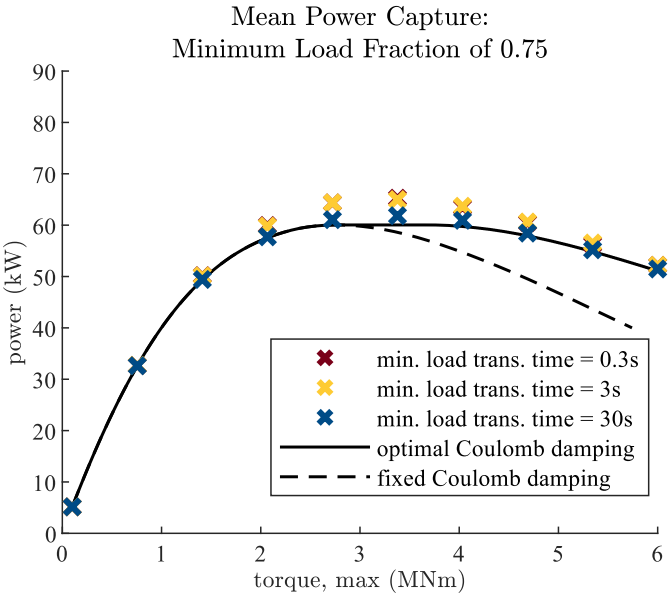

Figure 3.9: PTO load constraint study results: mean power capture with a minimum load fraction of 0.75.

The fastest load transition time of 0.3 s provides the greatest improvements in performance. The more moderate minimum load transition time of 3 s provides 56–77 percent of this improvement (for maximum torque values above 2 MNm); in a different framing, a transition time of 0.3 s performs 4–12 percent higher than a 3 s transition time. The longest transition time considered, 30 s, provides very little improvement in performance over the optimal Coulomb damping, if any.

Considering a minimum load fraction of 0 and the fastest response time of the PTO tested, the potential improvement over Coulomb damping is about 20 percent without increasing the maximum load capability of the PTO above the optimal Coulomb damping load of about 2.72 MNm. For higher maximum load values, the model predictive control outperforms the optimal Coulomb damping by up to 45 percent. For a minimum fractional load of 0.25, the potential improvements are reduced to about 11 percent and 30 percent, respectively. With a minimum load fraction of 0.5, there is improvement of up to only 20 percent over the optimal Coulomb damping. With a value of 0.75, the improvement is only up to 9 percent.

With respect to the maximum rate of load adjustment, faster rates of load adjustment improve mean power capture, but with only moderate improvement between minimum load transition times of 3 s and 0.3 s. The power capture is also improved by a wider range in the load achievable by PTO, provided primarily by lower minimum fractional load values.

3.3.3 Load Constraint Study: Yearly Average Performance

The third study investigates the weighted average WEC power absorption throughout a year using the same parameters for the MPC algorithm as the study in a single sea state. It also assumes a minimum load transition time of 3 s (based on this being only marginally lower performing than for the faster transition time of 0.3 s). Therefore, the power capture results, presented in Figure 3.10, are presented as functions only of the maximum load and minimum load fractions.

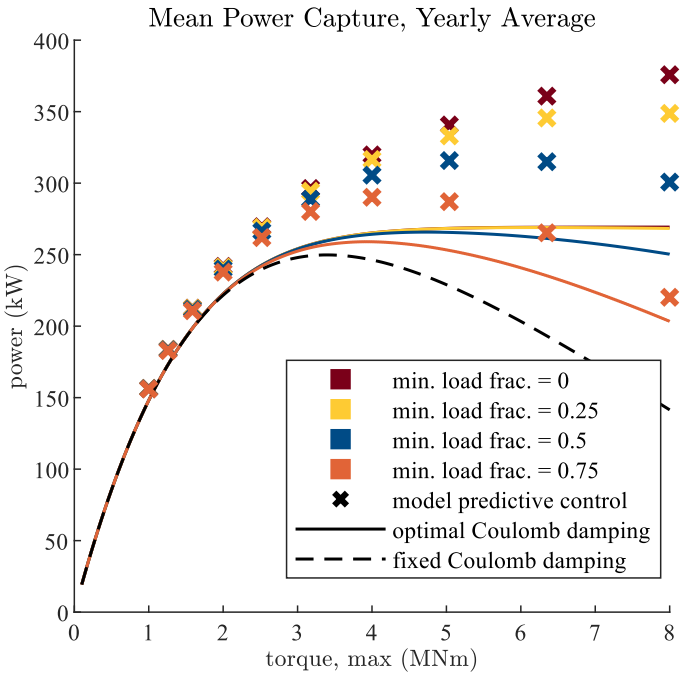

Figure 3.10: PTO load constraint study results: yearly average power capture assuming a maximum rate-of-change between load limits of 3 s.

The results obtained using the model predictive control are distinguished by color based on the minimum fractional load limit. These results are compared against the Coulomb damping results under the two conditions, as before. The results for the fixed Coulomb damping load case (i.e., the load is identical to the maximum load across all sea conditions) are plotted with a black dashed line. For optimal Coulomb damping, where the Coulomb damping is subject to the same constraints on the load as the model predictive control, results are plotted as a solid line with the color corresponding to the minimum load fraction.

The results show similar trends as for the performance in a single sea state but with less improvement (improvements are approximately two-thirds as high as for the performance in a single sea state). With a minimum load fraction of 0, the load control provides a 12 percent improvement with a maximum torque of 4 MNm and up to 29

percent at 8 MNm. With a minimum load fraction of 0.25, the improvements are in the range of 11 percent with a maximum torque of 4 MNm and up to 20 percent at 8 MNm. A minimum load fraction of 0.5 provides 5 percent improvement with a maximum torque of 4 MNm, and up to 9 percent with a maximum load of 5 MNm. Again, a minimum load fraction of 0.75 provides little improvement, and at higher maximum torque values, the performance is worse than the optimal Coulomb damping, which is likely due to poor performance of the optimization within the model predictive control in these cases.

3.4 Discussion

The results of these studies provide important insight into the design trade-offs in the PTO design. As expected, a capacity for adjusting the load on the WEC on a moment-to-moment basis is shown to provide significant improvements over holding the PTO load constant within a given sea state. Furthermore, the results identify the degree to which the limits on the PTO load magnitude and response time affect the performance of this load control.

Results show that a larger range of adjustment in the PTO load improves power capture, generally. However, a minimum load fraction of 0.25 appears to be a good target for PTO performance, being a point of diminishing returns. With a minimum load of zero, the moment-to-moment load control achieved a 29 percent improvement over optimal Coulomb damping; however, compared to performance with a minimum load fraction of 0.25, a minimum load of zero provides less than 1 percent greater performance at a maximum load of 4 MNm and up to 7 percent above that.

Performance improvements seen for a single sea state suggest that the speed of load adjustment between limits by the PTO should be at least as fast as a few seconds. A faster response on the order of a fraction of a second would further enhance the performance by about 5–12 percent while a slow response on the order of tens of seconds would provide no significant improvement over Coulomb damping.

An important case to consider involves implementing load control for a PTO that is designed based on optimal Coulomb damping. A PTO designed for a maximum torque of 4 MNm serves as a good reference for this case. With this reference design, moment-to-moment load control with a moderate load adjustment time of 3 s could provide up to a 12 percent improvement in the system performance, based on the results presented in Figure 3.10.

As an alternative, the PTO could be designed with moment-to-moment load control in mind. In this case, the plant performance could be improved up to about 29 percent. However, this would require the PTO to be capable of producing these higher loads, accompanied by a greater cost. For example, the maximum displacement of a WEC-driven pump size would need to be doubled to access the 29 percent improvement. Generally, the cost of a pump would be approximately proportional to its displacement. Therefore, the increased cost of the pump may outweigh the improved power capture.

Although the architecture of the PTO is not explored explicitly in this study, the results are highly relevant to the issue of choosing an architecture. The choice of architecture is a primary factor in determining the degree to which the PTO load can be varied and how quickly changes in the load can be implemented. For example, the parallel-type architecture studied in Chapter 2 on PTO architectures for wave-powered reverse osmosis has the outlet of the WEC-driven pump feeding the same pressure rail from which the RO module sources feedwater. With a fixed pump displacement, the load provided by the PTO is constrained by the pressure limits of the RO module (about 4–8 MPa), giving a minimum fractional load of 50 percent. Furthermore, with the WEC-driven pump sharing a pressure rail with the RO module, a high degree of capacitance is required to meet the limits on pressure variability at the RO module. That capacitance extends the time scale with which the load can be adjusted. Considering that the flow ripple from the WEC-driven pump, generated by the excitation of the waves, has a period of 3-10 s, a time constant on the order of several seconds to tens of seconds should be expected for a pressure response in this system. Such a time constant

would be outside the recommended speed capability for the moment-to-moment load control. Alternatively, implementing a variable displacement pump in such a system would increase the speed at which the load could be adjusted and could offer a greater range in the PTO load.

Finally, this study relied on a specific implementation of model predictive control that is computationally expensive and could not be implemented for real-time control, as shown by the results in Figure 3.5. Rather than providing an estimate for the potential performance of more efficient implementations of MPC, these results serve the purpose of estimating the maximum potential performance levels achievable regardless of the control method implemented. Although, the results presented here are in line with those found in [82], which compared an efficient MPC implementation to linear resistive damping control. In that work, the authors found that MPC achieved 40–60 percent greater average power capture than linear resistive damping. This level of improvement is in line with the 45 percent maximum improvement achieved in the single sea state performance in this work. However, comparing these results is not a definitive comparison between the two implementations of MPC because (1) linear resistive damping and Coulomb damping are not the same, (2) the authors did not optimize the resistive damping rate for irregular wave conditions, and (3) the WEC types used are different (a buoy versus an OWSC).

3.5 Conclusions

Model predictive control of the PTO load on a WEC was used in this study to estimate the performance advantage of controlled, moment-to-moment variation in the load over a Coulomb damping scheme. Along with this, the advantage was characterized based on PTO capabilities and the constraints on the load it applies to the WEC. The PTO performance was framed in terms of constraints on the range of the load and the speed at which the load could be adjusted. The average power captured by the WEC was

characterized as a function of these constraints, with results provided for both single sea state performance and yearly average performance, calculated as a weighted average across a realistic distribution of sea states. For single sea state performance, moment-to-moment load control achieved an improvement between 10 percent and 45 percent over an optimal Coulomb damping load. The improvement in yearly average performance was slightly lower, ranging between 11 percent and 29 percent. Therefore, these results show that there is a significant advantage offered by controlled, moment-to-moment adjustment of the PTO load. Further, the results suggest that the PTO should be able to adjust the load to at least 50 percent of its maximum load, and that the capability to adjust down to 0–25 percent is a worthwhile target. The results also suggest that the PTO should be able to adjust the load between extremes within a few seconds, while faster adjustment, on the order of 0.1–1 s could provide an additional 4–12 percent improvement. That there is an advantage with moment-to-moment conrtrol of the load counters the conclusion made in Chapter 2 that variable displacement, as a feature of the WEC-driven pump, offers no performance advantage; this study shows that it would.

The PTO load was formulated under the assumption that the PTO is passive and provides a load that is continuous in time. Future work may consider different formulations of the PTO load for similar studies, such as those involving reactive control or discrete changes in load. This would be important for considering how PTO performance affects the effectiveness of these types of load variations and for comparing different types of load variations.

Future work should also consider the effect of energy losses in the PTO, as the improved power capture by the WEC may be counteracted by increased losses in the PTO. For example, variable displacement hydraulic pumps and motors typically have lower efficiency at fractional displacements. While losses in the PTO were not considered in this work, the methods used could be modified to include them.

3.6 Data Availability

Data and custom software used are available at: `https://github.com/novaTehnika/2022-ConstrainedLoadControlStudy` (accessed 11 June 2023).

Chapter 4

Dynamic System Performance: Meeting Constraints on Pressure Variation

4.1 Introduction

In addition to the issue of productivity considered in Chapters 2 and 3, conversion of wave energy presents a challenge to the longevity of components. The wave energy conversion process is a characteristically variable process as it involves absorbing power under the force of slow, irregular waves with a high degree of variation. For example, the ratio between the peak and mean power absorbed by a WEC has been estimated to be anywhere between 7:1 and 58:1, depending on the system design and control scheme [20, 21]. In contrast, the conventional RO process is characteristically steady, with changes to operation being made very slowly and only as feedwater temperature changes or the membranes accumulate debris. In fact, several sources recommend that start-up and shut-down of RO systems should be performed relatively slowly, with a rate-of-change in pressure less than 70 kPa per second, to avoid mechanical damage to

the membrane and membrane housing [28, 23, 25].

The recommended limit to the rate-of-change in feed pressure is of particular interest in this work because it is a dominate constraint in sizing accumulator volumes. This constraint is specified for start-up and shut-down and extension to normal operation is not made explicit by the literature. However, in normal operation of conventional RO systems, the pressure is held nearly constant, so it is understandable that an explicit statement would not be made. Furthermore, the value of the constraint seems to not be substantiated in any literature. The lack of clarity on this issue suggests that the constraint may be conservative, simply based on experience, and/or that the underlying mechanisms of failure motivating the constraint are not well understood. However, both [28] and [23] claim that this constraint relates to mechanical damage to the membrane and membrane housing and suggest compaction of the membrane and cracking on the housing to be modes of failure.

Early work on wave-powered RO systems has dismissed this constraint. In the work by Folley et al., the constraint was acknowledged but neglected for lack of substantiation in literature and based on an argument that more robust RO system components would be produced if a wave-powered RO industry created the demand [29].

Recent, work by Sitterly et al. [89] and Das et al. [90] have acknowledged a potential for the pressure variations in wave-powered RO system to harm RO membranes. Both works studied the effect of pressure variation using an experimental system with pressure being controlled. Sitterly et al. controlled pressures to match numerical results of a wave-powered RO system model presented in [24]. As part of their analysis, the authors compared the performance of the RO module before and after the membrane elements were subjected to the pressure variation experiments. They reported a decrease in membrane permeability of 7.4 percent and a decrease in water flux of 18.4 percent. It is important to note that this change came after a standard break-in procedure where membrane compaction is expected. The authors hypothesized that the pressure variation drove additional compaction that would not have occurred otherwise.

The conclusion was that the pressure variation did not have significant effects on the membrane performance and integrity. However, from a system-level perspective, having membrane productivity decline 18.4 percent is substantial.

Das et al. [90] controlled pressure in two ways: first as sinusoidal variations between 35 and 65 bar and then in as rectified sinusoidal functions with pressure varying between 0 and 70 bar. Membrane integrity tests showed no significant change after the simple sinusoidal pressure tests. However, after the more extreme rectified sinusoidal tests, the membrane integrity tests showed a two to four times increase in the salinity of the permeate suggesting significant degradation of the membranes' integrity.

This paper addresses the design impacts associated with meeting the pressure rate-of-change constraint on several alternative PTO architectures, taking the system illustrated in Figure 1.8 as a the baseline. Design performance is evaluated by two design metrics: the total volume of accumulators deployed and the amount of power lost during operation. The baseline architecture is also evaluate without the rate-of-change constraint enforced. Each architecture is modeled mathematically and numerically simulated to estimate their performance. Grid studies are used to find optimal values for the design parameters relevant to each architecture.

The proposed architectures are described in the following section, Section 4.2. The methods of this study are described in Section 4.3 and include the mathematical models, the method of solving the models, and procedure for optimizing and comparing the design performance of each architecture. The results of the study are presented in Section 4.4 and are followed by a discussion in Section 4.5. Conclusions drawn from the study and suggestions for future work are presented in Section 4.6.

4.2 Proposed Power Take-Off Architectures

The baseline architecture for this design study, shown in Figure 1.8, includes a first-order low-pass filter in the form of a single high-pressure accumulator. A second-order

low-pass filter is easily constructed with the addition of a resistive element and a second accumulator as shown in Figure 4.1. The resistive element could be a passive element or an actively controlled valve. The passive element accomplishes the formation of a second-order low-pass filter while an actively controlled valve provides the opportunity of controlling the flow to the RO feed inlet and thereby rate-of-change in pressure. Both approaches reduces the total accumulator volume required to meet the pressure rate-of-change constraint.

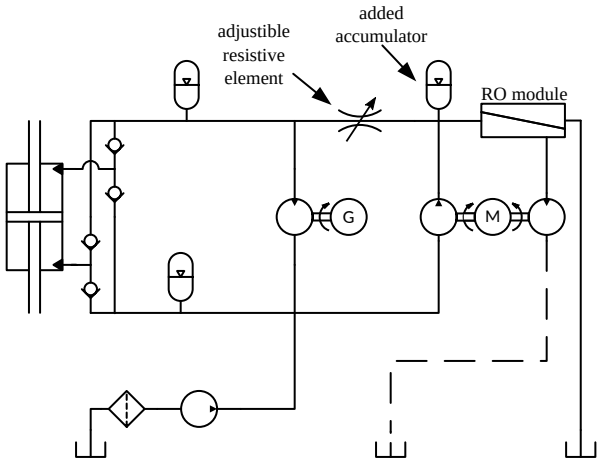

Figure 4.1: A parallel-type power take-off architecture having a resistive element and additional accumulator bank for enhanced reduction of pressure variation.

A third alternative is the series-type PTO architecture proposed in Section 2.2 and illustrated in Figure 2.4. In this architecture, the hydraulic motor of the parallel-type architecture is placed in series with the WEC-driven pump and RO module. This way the hydraulic motor, which can operate as either a motor or a pump, has direct control of the flow reaching the RO feed inlet from the WEC-driven pump.

4.3 Methods

The goals of this work are to (1) understand how the selection of architecture influences the required accumulator volume and energy losses in the system when the rate-of-change constraint is enforced and (2) understand how volume requirements compare when the constraint is not enforced. The metric assumed for energy losses is the average power losses associated with managing the pressure variation; specifically, the losses from the activation of pressure relief valves at the outlet of the WEC-driven pump and the feed inlet of the RO module, the power losses from the hydraulic motor and electric generator, and throttling losses of the resistive element.

Numerical models of the system are used to simulate the system and perform a grid search to identify optimal performing designs for each PTO architecture. The design variables considered in the grid search (where applicable) are the total high-pressure accumulator volume, the proportion of volume placed at the RO feed inlet (versus the outlet of the WEC-driven pump), and the resistance of the resistive element.

To identify the cost of the constraint to the design performance, the optimal design performance for the baseline architecture is evaluated with and without enforcing the constraint on pressure rate-of-change.

As is considered for the studies in Chapters 2 and 3, the hypothetical system being considered is one installed in the nearshore environment at Humboldt Bay, CA and which is being driven by the Oyster 1. The displacement of the WEC-driven pump and RO membrane area are selected based on the design study presented in Chapter 2. The parameters are selected from the parallel-type and series-type PTO architecture having a fixed pump displacement and fixed RO membrane area and are based on having the same RO membrane area and annual rate of freshwater production.

A single sea condition is evaluated which is selected from the sea states specified for the Wave-to-Water Prize competition [91]. The selected sea state from that set, having a significant wave height of 2.64 m and a peak period of 9.86 s, contributes the most to

the annual available wave energy and when taken as a corner condition (maximum sea height and wave period), accounts for approximately half of the available wave energy annually (this is based on data given in Figure 2.6 for the rate of occurrence of sea states with a weighting by the available wave power where the available power is proportional to the peak wave period and the significant wave height squared).

The following subsections present the mathematical models used to simulate the WEC and proposed PTO architectures, the control methods, the method of solving the numerical problem of simulating the system, and the procedures used to carry out the design study.

4.3.1 Modeling

The WEC/PTO system is modeled as being a dynamic system, described by a set of ordinary differential equations. The WEC and PTO subsystem models are coupled. The velocity of the WEC is an input to the PTO subsystem model and the reaction torque of the WEC-driven pump is an input to the WEC subsystem model. The model of the Oyster 1 WEC, developed in Section 2.4.2, is used in here. The dynamic model developed for the PTO is given in the following subsection, Section 4.3.1, and is followed by specification of the control methods in Section 4.3.1.

Power Take-Off Model

Each PTO architecture shares several components that are modeled identically. The differences between the PTO models are in the parameter values of the model (specifically the WEC-driven pump displacement and the hydraulic motor displacement), the flow connections, and the control algorithms applied.

A schematic showing the modeled variables and node connections for the parallel-type PTO architectures is given in Figure 4.2. This schematic accounts for the baseline architecture as well as the passive and active pressure ripple filtering architecture. For

the baseline architecture, the added resistive element and additional accumulator associated with the pressure p_f are excluded.

The low-pressure branch, which includes the charge pump and low-pressure accumulator were included in the model but are not described here because they have little effect on the behavior of the high-pressure branch. The pressure of the low-pressure branch in every simulation was approximately constant at 0.44 MPa. Instead, this part of the system is discussed in Appendix C, Section C.3.

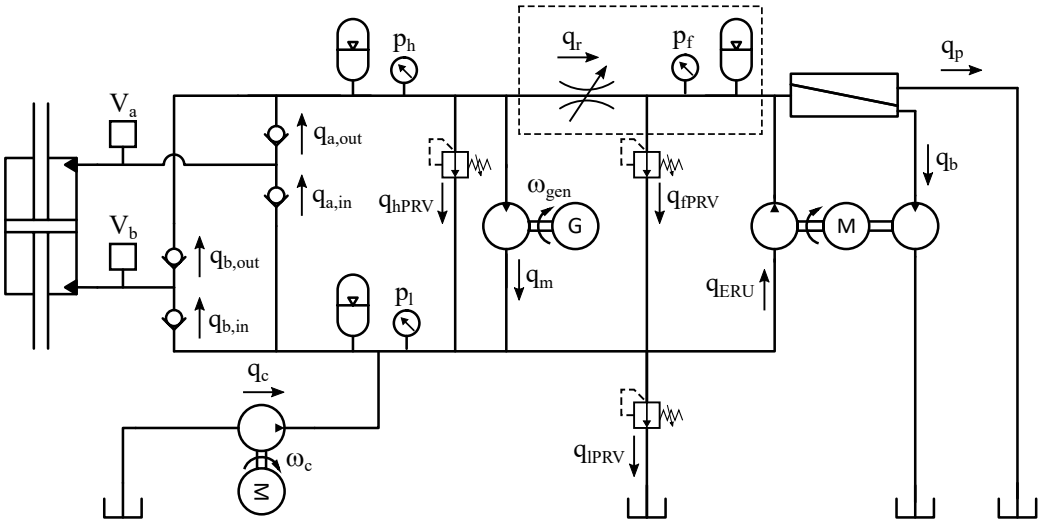

Figure 4.2: Modeling schematic for parallel-type power take-offs. An optional resistive element and additional accumulator bank are indicated with box with dashed lines.

A schematic showing the modeled variables and node connections for the series-type PTO architectures is given in Figure 4.3. For the series-type PTO architecture, the hydraulic motor discharges to RO feed inlet instead of the low-pressure branch.

The state variables for these PTO models are the pressures at nodes having compressible volumes and the integral of the error for a proportional-integral pressure regulating controller determining the shaft speed of the electric generator.

The derivatives of pressure states are a function of the capacitance of the node, the net flow into the node, and changes to the fluid volume. The capacitance is generally

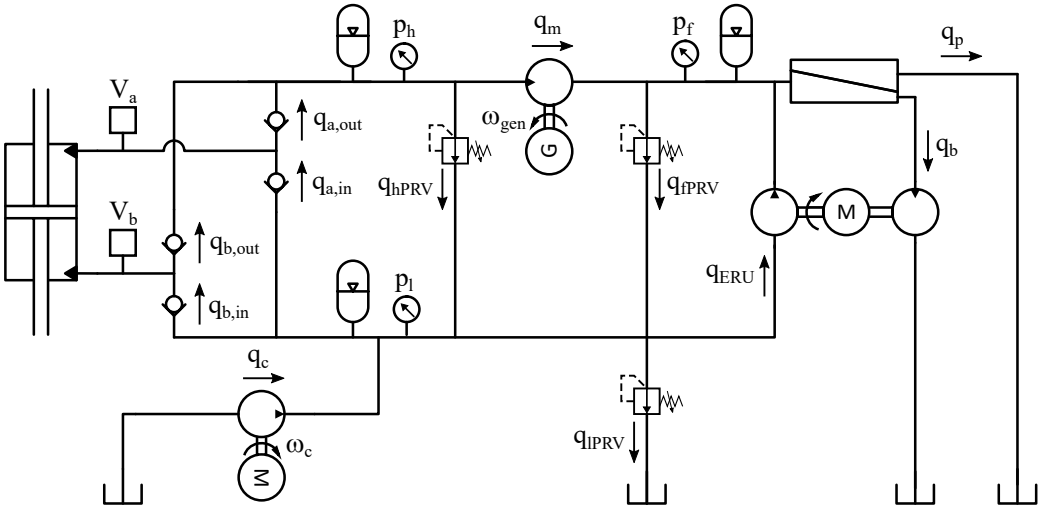

Figure 4.3: Modeling schematic for the series-type power take-off.

nonlinear and a function of the pressure of the node. Generically, the state equation for the pressure nodes is

$$C_i\left(p_i\right)\frac{dp_i}{dt} = \sum q_{in} - \sum q_{out} - \frac{dV_i}{dt} \tag{4.1}$$

where p_i is the pressure of node i, $C_i\left(\cdot\right)$ is the nonlinear function describing the capacitance of the node as a function of pressure, q_{in} and q_{out} are flowrates into and out from the node, respectively, and V_i is the volume of the node.

The two types of capacitive elements are included: compressible fluid volumes and ideal gas volumes. The pumping chambers of the WEC-driven pump are modeled as volumes of compressible fluid, with capacitance

$$C_{f,i} = \frac{V_i}{\beta_{eff}} \tag{4.2}$$

where β_{eff} is the effective bulk modulus of the fluid mixture. The working fluid is assumed to be a mixture of seawater and entrained gas with the properties given in

Table 4.1. The seawater is assumed to be linearly compressible while the entrained gas is modeled as an ideal gas compressed isothermally. Isothermal compression is assumed due to the wave frequencies being relatively slow (i.e., on the order of a second) and entrained gas bubbles being small. This gives an effective bulk modulus that is a function of the pressure such that

$$\beta_{eff}\left(p_i\right) = \frac{\beta}{1 + \beta\alpha_o \frac{p_o}{p_i^2}} \tag{4.3}$$

where β is the bulk modulus of the working fluid without entrained air and α_o is the entrained air volume fraction at the reference pressure p_o. The volume of each pumping chamber is a function of the WEC position and is assumed to change proportionally with the position of the WEC. The maximum extent of the WEC-driven pump is assumed to be at $\pm\pi/2$ radians from the vertical position of the flap-type WEC. An additional dead volume, equal to 10 percent of the total swept volume, is added to each pumping chamber to account for non-swept volume such as porting and piping.

Table 4.1: Working fluid parameters

Parameter	Value	Units
Density,ρ	1025	kg/m^3
Viscosity, dynamic, μ	$9.4{\cdot}10^{-4}$	Pa·s
Bulk modulus,β	$2.2{\cdot}10^{9}$	Pa
Entrained air fraction (at 1 atm), α	0.0001	-
Atmospheric pressure	101300	Pa

The accumulators are modeled as being ideal gas volumes being compressed isothermally (again because of the slow variation in pressures excited by the low-frequency WEC motion). The capacitance of an isothermally compressed volume of ideal gas is

$$C_{g,i}\left(p_i\right) = V_{c,i}\frac{p_{c,i}}{p_i^2} \tag{4.4}$$

where p_c and $V_{c,i}$ are reference values for pressure and volume of the gas at node i. In

the case of accumulators, these are the charge pressure and charge volume. For $p_i < p_{c,i}$, $C_{g,i}(p_i) = 0$. An additional compressed fluid volume is assumed to contribute to the capacitance of the pressure node with a volume equal to 1 percent of the charge volume for the accumulator.

Two types of valves are included in the system: the check valve of the WEC-driven pump and pressure relief valves. The flow through the resistive element of the pressure filter and the check valves of the WEC-driven is modeled as flow through an orifice such that

$$q_i(\Delta p_i) = k_{v,i} \frac{\Delta p_i}{|\Delta p_i|} \sqrt{\Delta p_i} \tag{4.5}$$

where $k_{v,i}$ is a flow coefficient for valve i, Δp_i is the difference between the upstream and downstream pressure. There is no flow though the check valves when the pressure differential is below the cracking pressure and there is a pressure margin over which the area of the valve increases with the pressure differential until it is fully open. For the margin regime, the flow coefficient for the check valves are assumed to vary linearly with the pressure difference between zero and the maximum value. Parameters for the check valves are given in Table 4.2 (justification for the flow coefficient is provided by a grid study presented in Appendix C, Section C.1. The model developed in Chapter 2, Section 2.3 is used to model the pressure relief valves. Parameters for the pressure relief valves are given in Table 4.3.

Table 4.2: WEC-driven pump check valve parameters

Parameter	Value	Units
Cracking pressure	$1{\cdot}10^5$	Pa
Margin to fully open	$1{\cdot}10^5$	Pa
Flow coefficient, inlet	15.18	$\mathrm{L/Pa^{1/2}}$
Flow coefficient, outlet	15.18	$\mathrm{L/Pa^{1/2}}$

Mechanical and flow losses of the hydraulic motor are modeled using the McCandlish-Dory model with constant coefficients [92] and fixed displacement. The flow rate through

Table 4.3: Pressure relief valve parameters

Parameter	Value	Units
PRV at WEC-driven pump outlet		
Cracking pressure, $p_{cr,hPRV}$	$20{\cdot}10^6$	Pa
Coefficient, $C_{prv,hPRV}$	$2.2361{\cdot}10^9$	$\mathrm{Pa}^{3/2}{\cdot}\mathrm{s/m}^3$
PRV at RO feed inlet		
Cracking pressure, $p_{cr,fPRV}$	$8.3{\cdot}10^6$	Pa
Coefficient, $C_{prv,fPRV}$	$1.4405{\cdot}10^9$	$\mathrm{Pa}^{3/2}{\cdot}\mathrm{s/m}^3$

the pump/motor is modeled as

$$q_m = D_m \omega_m \left(1 - \lambda \left(C_s \frac{|\Delta p|}{\mu |\omega_m|} + \frac{\Delta p_i}{\beta} \left(V_r + 1\right)\right)\right) \tag{4.6}$$

where D_m is the volumetric displacement per radian, ω_m is the shaft speed in radians per second, μ is the dynamic viscosity of the working fluid. The degree of laminar leakage loss is captured by the coefficient C_s and the degree of losses due to compressibility are captured by V_r. The variable λ has magnitude of one and is positive when the machine is in the pumping mode and negative when it is in the motoring mode. The torque of the motor and generator are modeled as

$$T_m = D_m \Delta p \left(1 + \lambda \left(C_v \frac{\mu |\omega_m|}{|\Delta p|} + C_f\right)\right) \tag{4.7}$$

where the degree of viscous torque loss is captured by C_v and coulomb friction losses are captured by C_f.

The WEC-driven pump and electric generator are assumed to have a fixed efficiency with values in Table 4.4. The WEC-driven pump displacement is derived from results in Chapter 2. The displacement of the hydraulic motor was chosen for the parallel-type architecture based on a grid study considering the performance of the pressure regulation and the power losses of the motor, generator, and pressure relief valves; this

study is presented in Appendix C, Section C.2. For the series-type architecture, it was chosen to provide the flowrate required to achieve steady operation of the RO module at 8 MPa.

Table 4.4: WEC-driven pump, hydraulic motor and generator parameters.

Parameter	Parallel-type | Series-type	Units
WEC-driven pump		
Displacement	0.23 | 0.163	m^3/rad
Efficiency, mechanical	0.9	-
Hydraulic motor & generator		
Generator efficiency	0.9	-
Maximum speed	1750	rpm
Motor displacement,	1000 | 2300	cc/rev
Laminar flow loss coefficient, C_s	$3.0554 \cdot 10^{-10}$	-
Volume ratio, V_r	1.103	-
Viscous torque loss coefficient, C_v	$7.1755 \cdot 10^{5}$	-
Coulomb torque loss coefficient, C_f	0.0259	-

The rate of permeate production by the RO module is modeled by Equation 2.2. The ERU is assumed to maintain a constant recovery ratio in the RO process of 25 percent. Mechanical and volumetric losses from the ERU's hydraulic motor and pump are modeled with constant efficiency. The electric motor makes up for the difference in torque between the hydraulic motor and pump. The hydraulic motor and pump are assumed to have the same volumetric displacement. Parameters used for the RO module and ERU are given in Table 4.5.

Control

There are two control schemes implemented for the PTO subsystem. First, the hydraulic motor and generator are used to regulate the RO feed pressure using a feed-back control loop. Second, the flow coefficient for the active resistive element is used to limit the rate of change in feed pressure. In this case, the flow coefficient is prescribed by feed-forward

Table 4.5: Reverse osmosis module and energy recovery unit (ERU) parameters

Parameter	Value	Units
Membrane area, S_{ro}	3,700	m^3
Permeability coefficient, A_{perm}	$2.57 \cdot 10^{-12}$	$m^3/(N \cdot s)$
Recovery ratio	0.25	-
ERU Volumetric efficiency	0.95	-
ERU Mechanical efficiency	0.95	-
ERU Mechanical efficiency	0.95	-

control.

Proportional-integral control is used for pressure regulation. The error is the difference between the pressure at the RO feed inlet and the nominal set point. The control signal is a nominal shaft speed for the generator. For the parallel-type PTO architectures, only the proportional term is used. The proportional and integral terms are both used for the series-type PTO architecture. The value for the proportional gain in both cases is $5 \cdot 10^{-4}$ rad/s/Pa. The integral gain is $5 \cdot 10^{-6}$ rad/s^2/Pa.

For the parallel-type PTO architectures, only the proportional term is used. The proportional and integral terms are used for the series-type PTO architecture. The value for the proportional gain in both cases is $5 \cdot 10^{-4}$ rad/s/Pa. The integral gain is $5 \cdot 10^{-6}$ rad/s^2/Pa.

The feed-forward control specifying the flow coefficient of the resistive element is based on a model for the pressure node capacitance and the flowrates associated with the RO module. In practice, the model would have to estimate these values and may include an observer that is informed by sensor measurements. For this study, these values are calculated by reversing the calculations given above. The feed-forward control identifies an ideal flow coefficient based on a positive rate of change in feed pressure equal to the prescribed limit. The flow coefficient command is bound by an upper bound attributed

to the size of the valve. The ideal flow coefficient is

$$k_{v,ideal} = \frac{p_h - p_f}{|p_h - p_f|} \frac{C_f\left(p_f\right) + q_f - q_{ERU,f}}{\sqrt{p_h - p_f}} \tag{4.8}$$

4.3.2 Numerical Solution

These models are solved using the Euler method with a time-step of 0.05 ms. This time step was selected based on convergence of a mass and energy balance in the study presented in Appendix A, Section A.2.2. Similarly, the length of time simulated is based on the convergence study presented Appendix A, Section A.2.3 which considers the power captured by the WEC, permeate produced by the PTO, and the peak rate-of-change in feed pressure. The simulations are 2250 s long with only the last 2000 s contributing to the performance calculations.

4.3.3 Design Studies

The PTO architectures are compared based on power losses and the total accumulator volume. The Pareto front is approximated using a multi-variable grid study. The pressure rate-of-change constraint is enforced through eligibility to the Pareto optimal set.

The variables of each grid study are specified in Table 4.6. Total volume refers to the total volume for the high-pressure accumulators. The distribution of volume between the accumulator upstream and downstream is indicated by the proportion of the total volume placed at the RO feed inlet. Along with the range of values, the number of grid points and the distribution scheme for the grid points are specified. Two grid point distribution schemes are used; a constant spacing between grid points and a base-10 log-scale spacing.

Table 4.6: Grid study parameters: bounds, number of grid points and spacing scheme

PTO architecture	Total volume (L)	Portion at RO feed	Flow coefficient ($L/s/kPa^{1/2}$)
Baseline	500-30,000 (80/log-10)	-	-
Passive element, with constraint	5,000-15,000 (10/log-10)	0.2-0.35 (10/equal)	0.1-15 (40/log-10)
Passive element, without constraint	1,000-15,000 (80/log-10)	0.05-0.9 (10/equal)	0.1-30 (20/log-10)
Active element	5,000-15,000 (10/log-10)	0.01-0.99 (40/equal)	40 (1/-)
Series-type	1,000-15,000 20/log-10)	0.01-0.95 (40/log-10)	-

4.4 Results

In this section, results are presented from the grid study for the baseline case, a comparison of the Pareto optimal performance results for each PTO architecture, and time-series results for the proposed PTO architecture with representative selections of design parameters.

Grid study results for the influence of accumulator volume on the peak rate-of-change in feed pressure and mean power loss for the baseline PTO architecture are given in Figure 4.4. The mean power losses include the pressure relief valves and the hydraulic motor and generator and are normalized to the mean power capture by the WEC. The lowest total high-pressure accumulator volume meeting the constraint on the pressure rate-of-change is 17,600 liters. Above 3,000 liters of accumulator volume, power losses are near constant at about 2.8 percent. The pressure relief valves are not used in this range, only the hydraulic motor and generator contribute to these losses. Below 3.000 liters, the pressure relief valve at the RO feed inlet is activated and increases the losses up to 5.5 percent with 500 liters of accumulator volume.

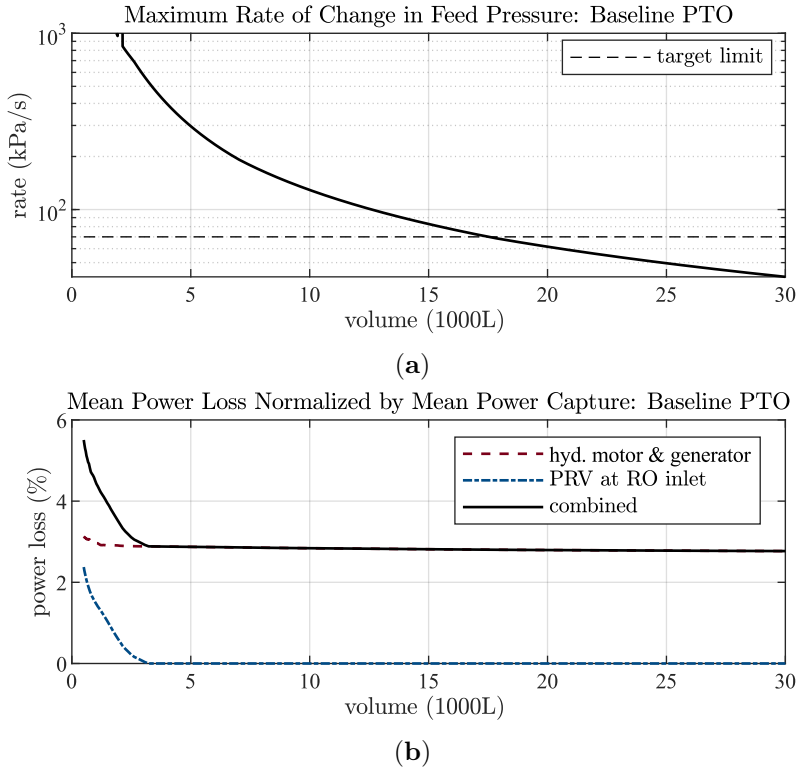

Figure 4.4: Grid study results for the baseline PTO architecture: rate of change in feed pressure (a) and power loss (b)

The Pareto optimal performance for all the PTO architectures is given in Figure 4.5. This figure shows the power losses as a function of the total accumulator volume. Results for the baseline architecture are given without regard for the pressure rate-of-change constraint (indicated by "no constraint" in the legend). However, the minimum volume needed to meat the constraint is indicated with a vertical dashed line.

These data show a clear ranking in the performance of the architectures. First, the parallel-type architecture with the additional resistive-capacitive network performs better with an active element than a passive element. Second, for accumulator volumes less than 8,000 liters, the series-type architecture outperforms the parallel-type architecture. However, above about 8,000 liters, the power losses are greater for the series type architecture; this is due to the losses of the hydraulic motor being greater in the series

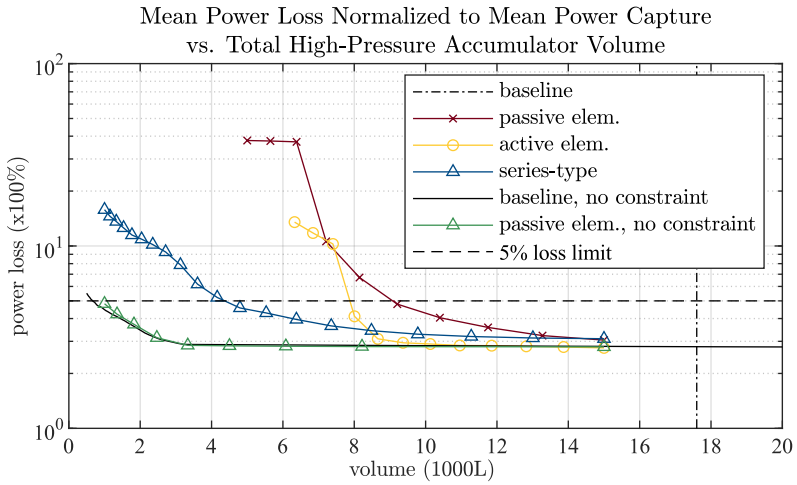

Figure 4.5: Comparison of design performance of each PTO architecture.

configuration, at 3.1 percent, than in the parallel configuration at 2.8 percent. Third, when the pressure rate-of-change constraint is not enforced, the baseline outperforms all cases where the constraint is enforced.

To compare required accumulator volume between the architectures, a value of 5 percent loss is considered, which is just less than double the power loss of the baseline architecture with 17,600 liters. At 5 percent combined power loss, the parallel-type architecture requires 9,090 liters with a passive resistive element and 7,920 liters with an active element. The series-type architecture requires 4,370 liters. Respectively, these values account for reductions in the required volume from the baseline of 48 percent, 55 percent, and 75 percent. When the pressure rate-of-change constraint is not observed, the baseline architecture requires 670 liters to achieve 5 percent combined power loss. This is 96 percent less volume than is required to meet the rate-of-change constraint.

Permeate production has been left out as a performance metric in this study since, by design, the permeate rate should be consistent for all cases. This is confirmed by the results shown in Figure 4.6, which presents the mean permeate production rates for the same Pareto optimal PTO designs for which the data in Figure 4.5 are found. The permeate results are between 1850 and 1900 m3/daym (within 3 percent difference) for

each design meeting the 5-percent combined loss. The baseline produced 1870 m^3/day when meeting the constraint and 1890 m^3/day without. The parallel-type produced 1860 m^3/day with the passive pressure filter and 1900 m^3/day with a the active pressure filter. The series-type produced 1850 m^3/day. The notable exceptions are with the parallel-type PTO with a passive resistive element having lower accumulator volumes; however, from Figure 4.5, these cases have greater than the 5 percent combined power loss chosen for a relative comparison.

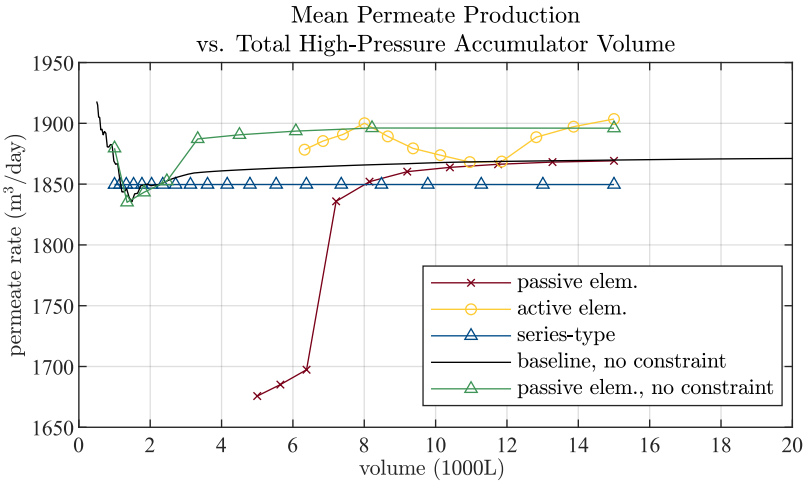

Figure 4.6: Comparison of permeate production for Pareto optimal results from each PTO architecture.

Time-series results related to pressure variation illustrate the behavior of these systems. These are presented for the designs meeting the 5-percent combined loss. First, results for the parallel-type architecture with a passive resistive element and 9,090 liters of total volume are given in Figure 4.7. The other design parameter values for this case are a flow coefficient of 4.06 L/s/$kPa^{1/2}$ and 28.3 percent of the accumulator volume at the RO feed inlet. These results show (1) pressure at the two accumulator banks, (2) the behavior of the hydraulic motor responding to the difference between the nominal RO feed pressure and the actual pressure, and (3) the rate-of-change in feed pressure compared to the target limit of 70 kPa/s. Two observation are notable. First, there is

only a small difference in pressure between the two accumulators (i.e., about 0.14 MPa on average). Second, the rate-of change in pressure approaches the peak of 70 kPa/s for only a small fraction of time within the 2000 s simulation. For comparison, the 97th and 99th-percentile values of the rate-of-change magnitude are indicated and are 38 and 48 kPa/s, respectively.

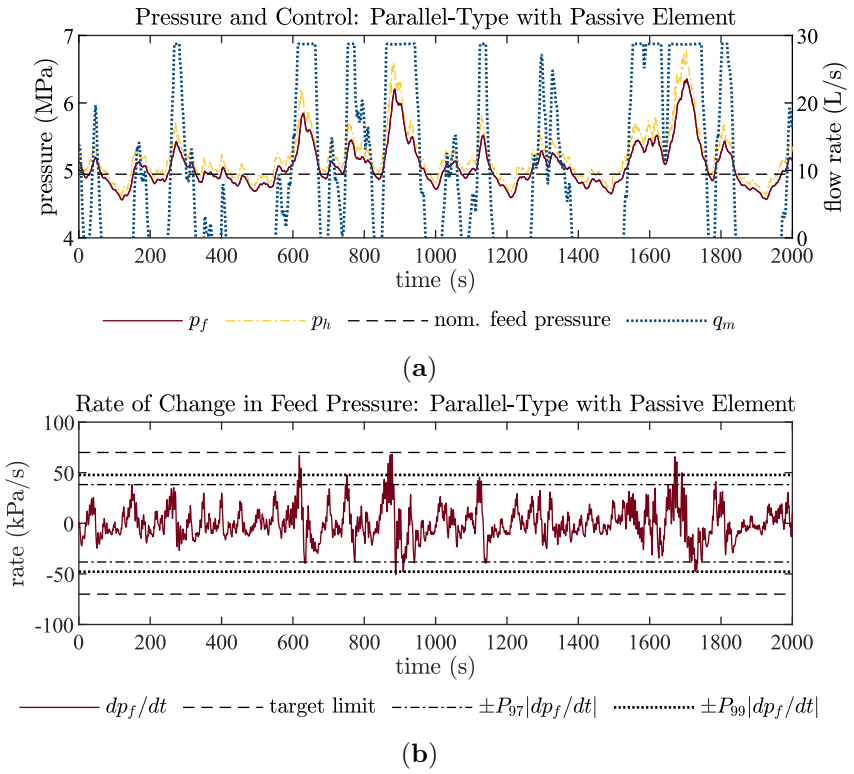

Figure 4.7: Time-series results related to pressure variation for the parallel-type architecture with a passive resistive element: pressure and hydraulic motor flow rates (a) and rate-of-change in RO feed pressure (b).

Results for the parallel-type architecture with an active resistive element and 7,920 liters of total volume are given in Figure 4.8. This design has 94.7 percent of the accumulator volume at the RO feed inlet. These results include (1) the pressure at the two accumulators, (2) the rate-of-change in feed pressure, and (3) the flow coefficient of the resistive element compared to the value determined from the feed-forward control

law. A notable observation is that several instances are shown where the pressure upstream of the resistive element peaks to extreme valves, yet these values are still well below the pressure relief valve setting of 20 MPa. Another is that the rate-of-change in feed pressure and the valve coefficient command signal have higher frequency content that is not seen with the passive element. Finally, the feed-forward command signal for the flow coefficient has a mean value (543 L/s/kPa$^{1/2}$) that is an order of magnitude greater than the maximum value (saturation limit) of 40 L/s/kPa$^{1/2}$ that was chosen.

Finally, time-series result or the series-type architecture having 4370 liters of total accumulator volume are given in Figure 4.9. This design has 1.12 percent of the accumulator volume placed at the RO feed inlet. These results include the pressure at the RO feed inlet and the pressure upstream of the hydraulic motor. The rate-of-change is not presented because it is near zero, being under direct control by the hydraulic motor. The RO feed pressure is controlled well and is nearly constant while the upstream pressure varies significantly. It is notable that the upstream pressure falls below the RO feed pressure for several periods within the simulation. In these cases, the hydraulic motor is in a pumping mode.

4.5 Discussion

The results of this study suggest the series-type architecture is a superior design to the parallel-type architecture with respect to controlling the pressure variation at the RO module. This is in addition to this architecture using a 29 percent smaller WEC-driven pump, based on the results of the study presented in Chapter 2. However, if the parallel-type type architecture is chosen, adding a resistive-capacitive network to form a second-order low-pass filter can reduce the total accumulator volume by about half.

The results of this study also show that there is a significant cost associated with enforcing the 70 kPa/s constraint on the RO feed pressure rate-of-change. Treating the constraint as a hard limit in this study showed that an order of magnitude more

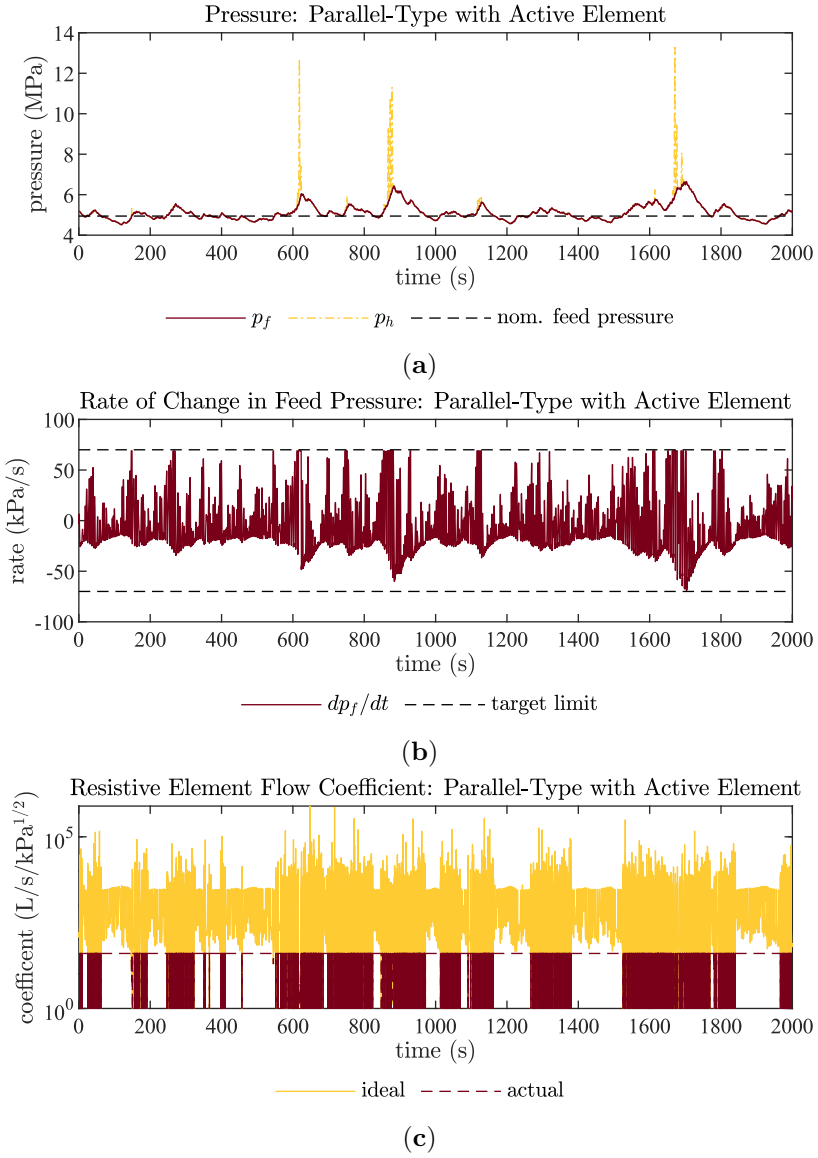

Figure 4.8: Time-series results related to pressure variation for the parallel-type architecture with an active resistive element: pressure (a), rate-of-change in RO feed pressure (b), and flow coefficient of the resistive element (c).

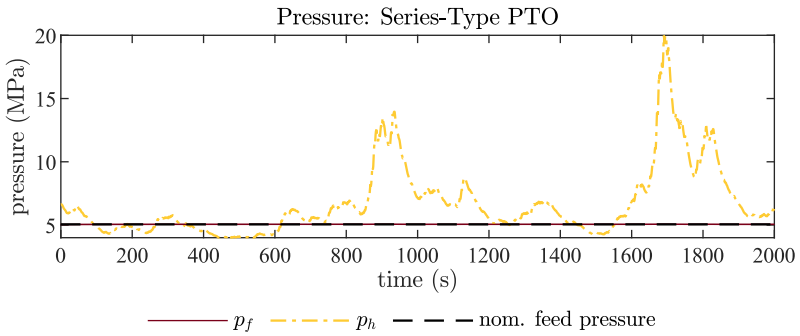

Figure 4.9: Timeseries results for pressure for the series-type PTO architecture.

accumulator volume is required than would be deployed otherwise. Yet the need for this constraint appears to be not well understood. Future work is needed to clarify what should be the constraints placed on the variation in pressure for wave-powered RO systems. Clarity on this issue will contribute significantly to our ability to design a robust and cost-effective system.

A specific recommendation would be to clarify whether the rate-of-change in pressure contributes to mechanical failure or just degraded performance, whether that mechanism is accumulative, and to what degree. It was noted that the portion of time where peak rate-of-change is observed for the parallel-architecture is relatively small and that that the 97th and 99th-percentile values for the rate-of-change are significantly lower than the peak. This highlights the fact that taking the limit of 70 kPa/s as a hard limit may be overly conservative. If a mechanism of failure or performance degradation is cumulative, a probabilistic distribution for the rate-of-change may be a more appropriate feature to consider in the design of these systems. If so, the system may tolerate a greater degree of pressure variation and require significantly less accumulator volume than observed in this study.

A trend in how accumulator volume is distributed in the system is illustrated by the study. Although the data are not given for all Pareto optimal results, the designs selected for comparison are representative of the trends between each architecture. Due

to the direct control of flow at the RO feed inlet, very little accumulator volume, (i.e., 1.12 percent) is placed at the RO feed inlet. In contrast, 28.3 percent of the volume is place at the RO feed inlet with the passive resistive element and 94.7 percent with the active resistive element. The active resistive element case is at the other extreme from the series-type PTO. This may be driven by the cases where the rate-of-change is negative, as in Figure 4.8b at about 1700 s. In these cases, the resistive element is unable to force an increase in flow. This is where the active resistive element is limited; it is capable of retarding flow but not driving flow.

There may be room to further reduce the accumulator volume required by these systems. This study has assumed an accumulator charge pressure of 4 MPa regardless of the use case. The capacitance of an accumulator is greatly affected by charge pressure with it being more advantageous to have the charge pressure close to the operating pressure. Attention to this margin may yield a reduction in the required volume. This is especially notable for the series-type architecture where the upstream pressure is expected to be greater than the RO feed pressure. However, there likely needs to be a significant margin to accommodate the high level of flow and pressure variation in these systems. Another opportunity for reduced accumulator volumes is with higher working pressure limits since the pressure relief valves drive the increased power losses at low accumulator volumes.

A limitation of this study is that the design of this system was only examined for a single sea condition. The sea condition that was selected was argued to be a reasonable corner condition, but there is a motivation to extend that corner condition to higher energy sea states. This would require greater accumulator volumes than found in this study because of the higher peak power input to the system. Generally, the accumulator volume requirement is dominated by relatively infrequent sea conditions. A trade-off between production and component size requirements needs to be negotiated. This adds further motivation for clarifying and justifying the constraint. If the constraint were to be relaxed, this trade-off could be shifted toward higher production and lower

accumulator volume requirements.

4.6 Conclusions

This study used numerical models to simulate the dynamics of a wave-powered RO system with a variety of power take-off architectures. A constraint found within the RO industry for the operation of an RO system is that the rate-of-change in feed pressure should not exceed 70 kPa/s. However, it is not clear what the mechanism of failure is that motivates the constraint. This study highlights the significance of this constraint in the design of a wave-powered RO system and the influence the power take-off architecture has on meeting this constraint. The results of this study showed that the constraint on the rate-of-change in feed pressure requires an order of magnitude greater high-pressure accumulator volume for the baseline system than if the constraint was not enforced. Furthermore, improvements over the baseline architecture were demonstrated for three proposed architects. The study found that the addition of a resistive-capacitive network in the hydraulic circuit reduced the required high-pressure accumulator volume by 48 percent when the resistive element was passive and 55 percent when the resistive element was actively controlled through feed-forward control. The study also found that a series-type architecture, where a hydraulic motor is placed in series with the RO module, provides a reduction of about 75 percent in required accumulator volume while also requiring a 29 percent smaller WEC-driven pump.

4.7 Data Availability

Custom software used in this study is available at: `https://github.com/novaTehnika/2023-DynPTOModelDesignStudies` (accessed 17 February 2024).

Chapter 5

Pipeline Model Fidelity for Wave Energy System Models

The content of this chapter was first presented in [93].

5.1 Introduction

Ocean wave-powered, reverse osmosis (RO) systems with hydraulic power take-offs (PTOs), like conventional desalination plants, are likely to included long pipelines. However, prior published work has not considered the effects that pipelines may have on the dynamics of wave energy PTOs. This chapter presents a study comparing pipeline modeling techniques in the context of a generic, constant pressure hydraulic PTO, like is shown in Figure 1.5a, in normal operation. The study is conducted to (1) reveal the significance of various attributes of long pipelines and (2) recommend pipeline modeling techniques for use in system models that are built to estimate metrics like power loss and variation in pressure under normal operation of the plant.

5.1.1 Background

The wave energy conversion process is a characteristically variable process, whereas conventional RO processes are characteristically steady. Some constraints on the dynamic behavior of the PTO must be considered to avoid damage to RO system components that are conventionally designed for steady operation. Membrane manufactures specify a variety of constraints that would limit the dynamic fluctuation of an RO system such as a limited range of operating pressure (e.g., 4–8 MPa) and a maximum rate-of-change in pressure (70 kPa per second) [28, 23, 25]. Other constraints may develop as the design of these system matures and failure mechanisms of RO components are better understood, such as fatigue limits on the RO membrane which has yet to be characterized [94].

Although prior modeling and design analyses given in the literature may be adequate for initial estimates of performance, the model fidelity may be inadequate for performing effective design without accounting for pipeline dynamics. In fact, no published work on wave energy converters has considered the presence of long pipelines despite these being a likely feature. This includes both wave-powered RO [13, 51] and electrical power producing systems [52] that have a hydraulic PTO.

To illustrate the scale of pipelines and their excitations in wave-energy systems, consider the electric power producing prototype plant built by Aquamarine Power, called Oyster 1 [52]. This WEC was placed 500 meters offshore while its turbine and electric generator were placed onshore. These two parts of the plant were connected by 500-meter-long, high-pressure and low-pressure pipelines. Depending on the geography of the seabed, the pipeline may be anywhere between 300 and 1500 meters long [51]. In addition, the pulsations generated by the WEC-driven pumps would typically fall in the range of three to ten seconds (half the peak wave period which is typically 6–20 s). For these conditions, the wavelengths of the pressure waves traveling in the working fluid approach the same order of distance as the length of the pipeline (considering wave

speeds 800–1500 m/s). At this scale, the pipeline dynamics may have important effects on plant performance and on the pressure variation at the RO module. Therefore, it is important to know what models for pressure and flow though pipelines are adequate for effective system design.

5.1.2 Pipeline Classification, Modeling Techniques, and Guidelines

The spectrum of pipeline modeling techniques includes a variety of lumped parameter and distributed parameter methods. Lumped parameter methods lump the resistive, inertive, and capacitive effects of the pipeline into discrete elements arranged as shown in Figure 5.1 for short, medium, and long lines (pipelines). Resistance is often described by the Darcy-Weisbach equation while the inertia and capacitance effects are described by the relevant ordinary differential equations (ODEs). Distributed parameter models account for the wave delay explicitly and are either direct solutions or approximation of to the partial differential equations (PDEs) for one-dimensional flow.

As suggested by Figure 5.1, lumped parameter models are classified by the length of pipe they can model. Short lines are adequately described by their flow resistance, while the effects of medium lines are better characterized by the configuration of lumped capacitive, resistive, and inertive elements shown for the medium line model in Figure 5.1. This configuration of elements for the medium line model has been referred to as the nominal π [95] and is referred to as a π-lumps here. Long lines are best described by distributed parameter models with the continuously distributed nature of the resistance, capacitance, and inertance accounting for the finite speed of pressure waves: however, an approach to approximating the distributed nature of the pipeline is to model the pipeline as a series of N π-lumps as shown in Figure 5.1 for the long line model [96].

Distributed parameter methods are diverse and a subject of study for many researchers [97], including comparative studies that focus on efficiency and accuracy [98, 99]. The most familiar methods to the wider engineering community might be the numerical approaches of finite-difference and finite-volume methods. Some advanced

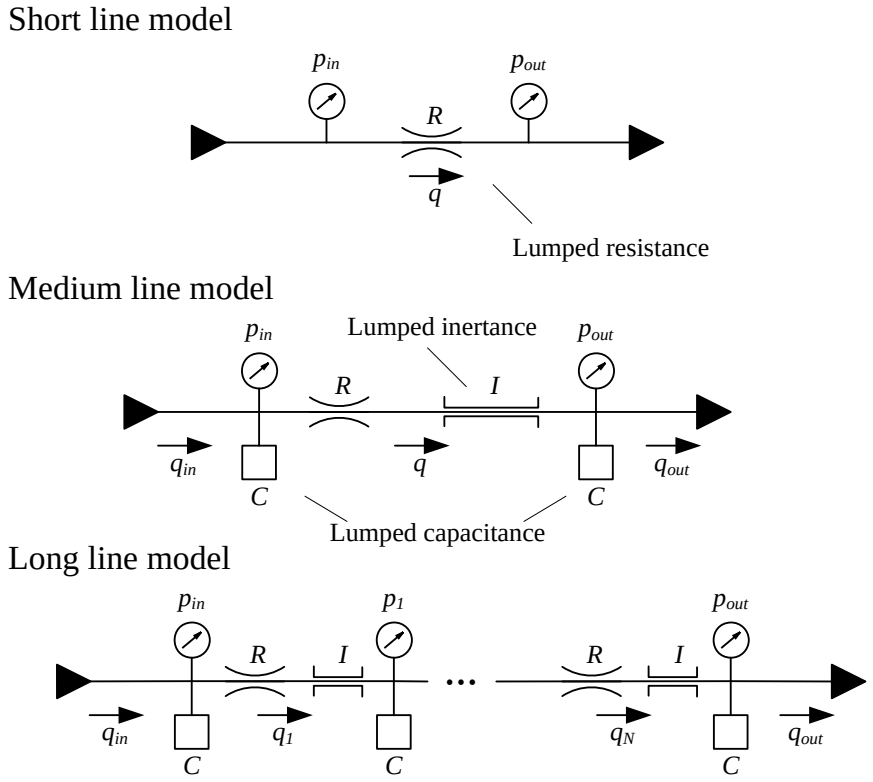

Figure 5.1: Lumped parameter pipeline model configurations having resistive (R), capacitive (C), and inertive (I) properties: (Top) short line, (middle) medium line, and (bottom) the long line, N π-lump model

one-dimensional, finite-volume, Godunov-type schemes offer a high degree of efficiency, accuracy, and flexibility [100, 101]. Other methods like modal approximation [98] and the transmission line model [102, 103] are efficient and have been subject to developments aimed at improving accuracy and robustness. However, these are restricted to linear, constant parameter cases.

Methods using the Method of Characteristics (MOC) have been well regarded for their accuracy, efficiency, and ease of implementation [97, 104]. These have also been modified and used to capture a high degree of nonlinearity, including cavitation and

column separation [105, 106]. Using the MOC, the system of PDEs describing one-dimensional flow in a pipeline are reduced to a system of ODEs valid along positive and negative characteristics. In many implementations, the system of ODEs is integrated analytically along the characteristics to give an explicit system of equations for the next time step of a simulation. The drawback of this method is that it is restricted to a fixed time step solution. To couple the pipeline model based on the MOC to variable time step solvers or to model pipe networks that include pipelines of variable length, require methods like interpolation.

The most common implementation of the MOC-based pipeline models assumes a fixed speed of sound and neglects the effect of the fluid velocity on the wave speed. The MOC method can also be augmented with the discrete gas cavity model (DGCM) to account for the effects of entrained air on the speed of sound in the fluid and can be used to capture cavitation in the pipeline [105, 106].

There are several guidelines provided in literature to guide the selection of pipeline models (i.e., lumped versus distributed parameter). Wylie and Streeter [106] recommend distributed parameter models for all transient problems but conceded that when computational cost is a concern, lumped parameter models (short and medium lines) may be adequate for pipelines whose lengths are less than 4 percent of the wavelengths of the pipeline excitations. That is where the wavelength (L_w) is determined from speed of sound in the fluid (a) and the frequency of the excitation (f_e) such that

$$L_w = \frac{a}{f_e} \tag{5.1}$$

For the analysis of electrical power lines, which are analogous to fluid filled pipelines, Grainger and Stevenson [95] also recommend a classification based on line lengths such that short line models are used for lines shorter than $0.016L_w$ and medium line models are used for longer lines, up to $0.046L_w$; otherwise the lumped, long line model or distributed parameter models should be used. Finally, Watton [96] recommends an

order-of-magnitude comparison of time constants within the problem under consideration.

The context of recommendations for modeling practice should be considered. Early work on pipeline transients, on which [106] is largely based, is focused on analysis of waterhammer events arising from transient inducing events like sudden valve closures and pump start-up, possibly in piping networks. The analysis in [95] is focused on electrical power systems that operated nominally under highly regular alternating current, may be disturbed by similarly strong transients, and must meet the constraints on power quality placed on electrical-grid infrastructure. Watton [96] is concerned with conventional fluid power problems, much of which is oriented towards feedback control of the system [98] (for which modal analysis is the favored approach). The strength of transients in each case are different and analysis is oriented toward different concerns and design methods.

The context of wave energy is different in several ways from those in which the guidelines above originate, suggesting that different guidelines might be more appropriate. Yet, these differences are in contradiction with each other and it is not clear how these guidelines should be treated for wave energy systems. (1) Waves forcing the system are best characterized by a continuous distribution of frequency components spanning about two orders of magnitude (e.g., Equation 2.21) rather than simple sinusoidal signals or by step and ramp inputs. This wide range in excitation frequency suggests that the peak frequency of the waves might not suffice for evaluating the length of the pipeline. (2) The degree to which power smoothing is necessary for these systems would result in weaker transients compared to transients like those excited by sudden valve closure. Design metrics might be captured well enough by lower fidelity models where transients are relatively weak, even if the exciting frequency is near the natural frequency of the pipeline. (3) Finally, the fragility of a conventional RO membrane elements and the extreme constraints which manufactures place on their use suggests that even weak transients may be important, and that higher model accuracy is needed.

With these contradicting observations, it is not clear whether the modeling guidelines found in the literature are applicable to the analysis of hydraulic PTO designs considered for wave energy applications. Therefore, this work compares results of the relevant modeling techniques in the context of a simple, but representative, hydraulic PTO circuit. Several metrics are considered that have the potential to highlight the effects of pressure variation and wave delay. The following section, Section 5.2, describes the methods used in this study and is followed by the formulation of the mathematical models considered and their implementation in Section 5.3. The results of the study are presented in Section 5.4. A discussion of the results is given in Section 5.5. Conclusions from the study are given in Section 5.6.

5.2 Methods

This study considers the performance of five different pipeline models in the context of a hydraulic PTO for wave-energy conversion. Several design cases are considered in which important system parameters are varied, such as accumulator capacitance and pipeline length. This section describes the system in Sub-section 5.2.1, the design cases in Sub-section 5.2.2, and the pipeline models in Sub-section 5.2.3. Sub-section 5.2.4 specifies the variables considered to be appropriate metrics for hydraulic PTOs in wave energy systems and by which the performance of the pipeline models are compared.

5.2.1 The System

The PTO system considered has the WEC driving a pump offshore and the load on the system (e.g., a RO module) located onshore. The PTO's hydraulic circuit is shown in Figure 5.2. This circuit includes (1) a WEC-driven, (2) low and high-pressure pipelines, (3) a load resistance, (4) a low-pressure accumulator (LHA) at inlet of the pump, (5) a high-pressure accumulator (HPA) at the outlet of the pump, and (6) a HPA at the high-pressure node of the load resistance. The low-pressure node of the load resistance

has a fixed pressure that replicates the case that a kinetic charge pump is acting to maintain a fixed, elevated pressure in the low-pressure branch of the circuit.

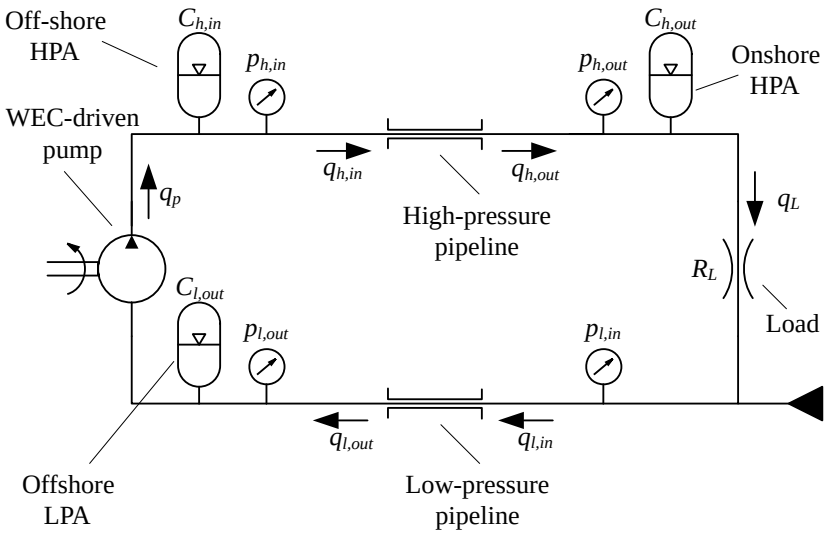

Figure 5.2: Schematic of the PTO hydraulic circuit with modeling variables

5.2.2 Design Cases

The system parameters values, specified by design case, are given in Table 5.1. The design cases are described as follows:

- A through D – Four cases with increasing capacitance (as if increasing accumulator volume) with the HPAs offshore and onshore having equal capacitance and pipelines having a length about 25 percent of the peak input wavelength (i.e., 1000 meters).

- E and F – Two cases identical to case B but with the total HPA capacitance unevenly distributed between offshore and onshore.

- G though I – Three cases identical to cases B, E, and F, respectively, but with shorter pipelines which have a length about 2 percent of the peak input wavelength (i.e., 100 meters).
- J – One case identical to case B where the entrained air content is increased.
- K – One case where the length of the pipeline is approximately half the length of the peak input wavelength (i.e., 2200 meters), in which case the line frequency is equal to the peak input frequency.

For all design cases, the peak wave period is 6 s, the load resistance and pump flow parameter X_p are set to give a nominal pressure in the high-pressure branch of 6 MPa with a 100-kW average load power. (Details about X_p are given in Section 5.3.2). The fixed pressure at the low-pressure side of the load is varied based on the capacitance of the LPA so that the pressure at the inlet of the pump does not fall below 0.5 MPa. Finally, as a reference, the capacitance values given in Table 5.1 are translated to equivalent initial charge volumes for isothermally expanding, ideal gas under the conditions specified in the table.

5.2.3 Pipeline Models

The five pipeline models tested are:

1. Short line model – only the flow resistance of the pipeline is modeled.
2. Medium line model – a single nominal π-lump is used to model the flow resistance, capacitance, and inertia of the fluid in the pipeline.
3. N π-lump model – a network of N nominal π-lumps are used to approximate the distributed nature of the flow resistance, capacitance, and inertia of the fluid in the pipeline. The value N is chosen to give segment lengths as close to but less than 4 percent of the peak input wave length.

Table 5.1: Design case parameters

	A	B	C	D	E	F	G	H	I	J	K
Working Fluid: Water											
Density (kg/m^3)	1023										
Viscosity (Pa.s)	9.4×10^{-4}										
Bulk modulus (GPa)	2.2										
Air volume fraction at 101.3 kPa	0.0001									0.001	1×10^{-7}
Pump Flow											
X_q (m^3)	0.103										
Peak wave period,	6										
Load											
Resistance (Pa.s/m^3)	2.83×10^8										
Tank Pressure (MPa)	1.8	1.35	1.1	0.95	1.35						
Low-pressure high-pressure pipelines											
Length (m)	1000						100			1000	2200
Diameter (m)	0.15						0.1			0.15	
Offshore low-pressure accumulator											
Capacitance (mm^3/Pa)	100	200	400	800	200						
Charge volume equivalent at 0.5 MPa with charge pressure at 0.15 MPa (L)	167	333	667	1333	333						
Offshore high-pressure accumulator											
Capacitance (mm^3/Pa)	50	100	200	400	10	190	100	10	190	100	
Charge volume equivalent at 6 MPa with 4 MPa charge pressure (L)	450	900	1800	3600	90	1710	900	90	1710	900	
Onshore high-pressure accumulator											
Capacitance (mm^3/Pa)	50	100	200	400	190	10	100	190	10	100	
Charge volume equivalent at 6 MPa with 4 MPa charge pressure (L)	450	900	1800	3600	1710	90	900	1710	90	900	

4. Method of Characteristics with constant properties and fixed grid (fMOC) – the Method of Characteristics is used to obtain an explicit solution to the pressure and flow in a fixed, staggered grid.

5. Discrete gas cavity model using the Method of Characteristics (DGCM) – the fMOC is augmented with discrete gas volumes at nodes in a fixed staggered grid to capture the effects of entrained air in the working fluid.

5.2.4 Metrics

The metrics that are compared between pipeline models are:

- The average power loss in each pipeline
- The standard deviation of the pressure in each accumulator
- The peak rate-of-change in pressure in the onshore HPA. The 99.7-percentile value will be used due to the stochastic nature of the problem
- The mean and standard deviation of the pressure differential across the WEC-driven pump

These choices give an account of the variables that a system designer would be concerned about in the analysis of a hydraulic WEC PTO. The rate-of-change in pressure is specific to the design of wave-powered RO systems where manufactures have placed constraints on the rate-of-change in pressure in the RO module. The mean pressure in the accumulators is ignored because the differences are insignificant. However, wave delay effects could affect the mean pressure differential across the WEC-driven pump, and therefore it is reported to test this notion.

5.3 Modeling

The following mathematical models were used to simulate the plant shown in Figure 5.2. The nomenclature follows from that schematic. Sub-section 5.3.1 reports the simple elements of the system. Sub-section 5.3.2 presents the development of a pump flow model that reflects the WEC motion in irregular waves. Sub-section 5.3.3 presents the pipeline models. Implementation of the model is specified in Sub-section 5.3.4.

5.3.1 System Model

The pressure nodes are governed by the capacitance of the accumulators as described in Equation 4.1. Capcitance is assumed constant. The flow rate through the load is governed by the resistance such that

$$R_L q_{load} = p_{h,out} - p_{l,in} \tag{5.2}$$

where the subscripts "in" and "out" refer to the inflow and outflow.

5.3.2 Pump Flow

To replicate the flow from a WEC-driven pump, the pump flow is constructed from an inverse Fourier transformation of a spectral density function (PSD) developed here and based on Equation 2.21. This transformation is used to generate a predetermined pump flow as a function of time. This method neglects the effects of the system pressures variation on the WEC load; however, the purpose of this simplified approach, rather than simulating a WEC in the time domain, is to keep the inputs to the PTO the same between models.

To simplify generation and scaling of an input to the PTO model, the concept of a response amplitude operator (RAO) is used. The RAO, given as $R(\omega)$, is a transfer function relating the amplitude of motion of a wave excited body to the amplitude of

the wave elevation, where ω is the wave frequency. This is defined by

$$S_R(\omega) = R(\omega)^2 S_w(\omega) \tag{5.3}$$

where S_w is the wave elevation PSD and S_r is the PSD for the WEC position.

A pump flow can be found as follows. With the motion of the WEC coupled the pump, the velocity of the pump is found from the derivative of the WEC position such that

$$\dot{\Theta}(\omega) = j\omega\Theta(\omega) = j\omega S(\omega) \tag{5.4}$$

Considering that the pump flow is proportional to the pump velocity,

$$Q_p(\omega) = D\dot{\Theta}(\omega) \tag{5.5}$$

where D is the pump displacement. Then, defining a wave elevation PSD normalized to the significant wave height,

$$\hat{S}(\omega) = \frac{S_w(\omega)}{H_s^2} \tag{5.6}$$

and defining a pump flow magnitude parameter,

$$X_q(\omega) = DR(\omega) H_s\sqrt{2} \tag{5.7}$$

provides the following expression for pump flow in the time domain, where the PSD for the pump flow is transformed to the time domain using a summation of sinusoids.

$$q_s(t) = \left| \sum_{i=1}^{n} \left(X_q(\omega) \sqrt{\omega_i^2 \hat{S}(\omega_i) \Delta\omega} \right) \sin(\omega_i t + \psi_i) \right| \tag{5.8}$$

The phase of each frequency component, ψ_i, is random and distributed uniformly between $-\pi$ and π. The bin sizing of the PSD for each frequency component is $\Delta\omega$ and is constant. While $R(\omega)$ represents the dynamic response of the WEC, and therefore,

$X_q(\omega)$ would generally be a function of wave frequency, only constant values for X_q are considered in this work. Therefore, the frequency content of the input to the PTO is only a function of the wave elevation PDF while a realistic WEC response may be more narrowly distributed.

5.3.3 Lumped Parameter Pipeline Models

The lumped parameter models are composed of lumped resistive, capacitive, and inertive elements. Using the Darcy-Weisbach equation, the pressure differential of the resistance elements is

$$p_{in} - p_{out} = Rq \tag{5.9}$$

where R is the resistance parameter and is given by

$$R = fRe\frac{2\mu L}{\pi d^4} \tag{5.10}$$

where μ is the dynamic viscosity of the fluid, d is the internal diameter of the pipeline, L is the length of the pipeline, and the f is the friction factor. The friction factor is a function of the Reynolds number, Re, and is modeled for laminar and turbulent flow using the Blasius correlation for the turbulent regime and a linear interpolation in the transitional flow regime. This gives

$$f = \begin{cases} \frac{64}{Re} & \text{if} \quad Re <= Re_1 \\ f(Re_1) + \frac{f(Re_2)-f(Re_1)}{Re_2-Re_1}(Re - Re_1) & \text{if} \quad Re_1 < Re < Re_2 \\ 0.316Re^{-\frac{1}{4}} & \text{if} \quad Re >= Re_2 \end{cases} \tag{5.11}$$

where the parameters Re_1 and Re_2 are bounds for the linearly interpolated transitional range for the Reynolds number. These are taken as 2300 and 4500, respectively.

The lumped fluid volumes are modeled as isothermally compressed mixtures of the

working fluid and entrained air. The gas is modeled as an ideal gas. The expression for capacitance given in Equation 4.2 with the effective bulk modulus given by Equation 4.3.

For inertial elements,

$$I\frac{dq}{dt} = (p_{in} - p_{out}) \tag{5.12}$$

where I is the inertance of the lumped fluid given by

$$I = \frac{\rho L}{AN} \tag{5.13}$$

Here, ρ is the density of the fluid, L is the length of the pipeline, and A is the cross-sectional flow area of the pipeline.

5.3.4 Distributed Parameter Pipeline Models

The distributed parameter models are found using the Method of Characteristics with the assumption of a fixed wave speed and a negligible effect of the fluid velocity on the wave speed. The formulations that follow are mathematical identical to the formulations given in [106] except for the use of pressure instead of head, which is a more convenient formulation for fluid power systems.

The computational grid spacing, illustrated in Figure 5.3 is governed by

$$\frac{\Delta x}{\Delta t} = a \tag{5.14}$$

where Δx is the step size in space and Δt is the step size in time. Assuming thick walled pipe the wave speed is given by

$$a = \sqrt{\frac{\beta_{eff}}{\rho}} \tag{5.15}$$

where the effective bulk modulus is given by Equation 4.3.

The compatibility equations resulting from the Method of Characteristics for the fMOC model give an explicit system of equations used to solve for the pressure and flow

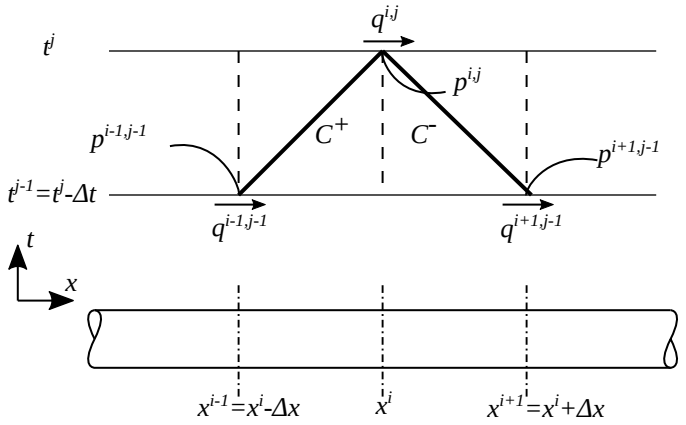

Figure 5.3: Computational grid illustration for the fMOC model

at the i-th node in space and j-th node in time based on the prior time step, $j-1$. These are

$$C^+ : p^{i,j} = C_P - B_P q^{i,j} \tag{5.16}$$

$$C^- : p^{i,j} = C_M + B_M q^{i,j} \tag{5.17}$$

where

$$C_P = p^{i-1,j-1} + \frac{a\rho}{A} q^{i-1,j-1} \tag{5.18}$$

$$B_P = \frac{a\rho}{A} + \rho \frac{f\Delta x}{2dA^2} |q^{i-1,j-1}| \tag{5.19}$$

$$C_M = p^{i+1,j-1} - \frac{a\rho}{A} q^{i+1,j-1} \tag{5.20}$$

$$B_M = \frac{a\rho}{A} + \rho \frac{f\Delta x}{2dA^2} |q^{i+1,j-1}| \tag{5.21}$$

The DGCM follows a similar form and implementation but includes the gas volume at each node, V_g, in the continuity equation and involves a flow rate upstream, q_u, and

downstream, q_d, from the node rather than a single flow rate through each node. This is demonstrated as part of the DGCM computational grid illustrated in Figure 5.4.

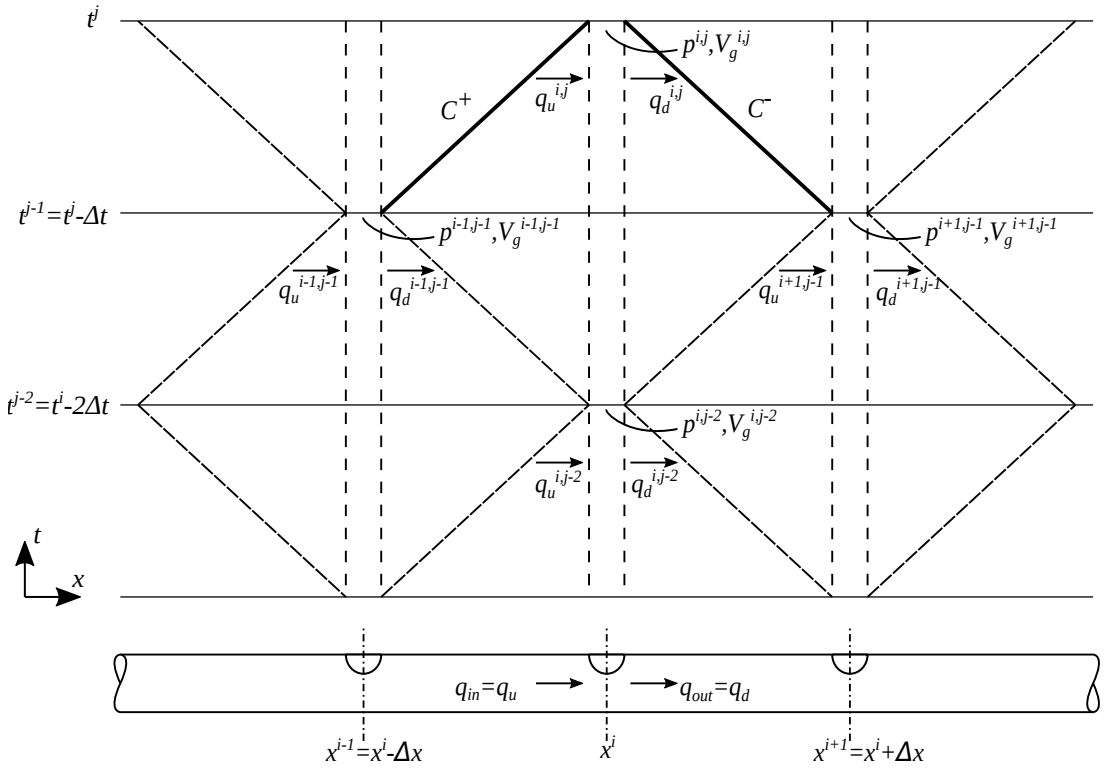

Figure 5.4: Computational grid illustration for the DGCM model

The continuity equation is integrated numerically with a weighting factor, ψ, such that $0.5 < \psi <= 1$. This gives

$$V_g^{i,j} = V_g^{i,j-2} + \left[\psi\left(q_d^{i,j} - q_u^{i,j}\right) + (1-\psi)\left(q_d^{i,j-2} - q_u^{i,j-2}\right)\right] 2\Delta t \tag{5.22}$$

The gas volume at the pressure node is related to the pressure such that

$$V_g^{i,j} = \frac{\alpha_o p_o V}{p^{i,j} - p_v} = \frac{C_1}{p^{i,j} - p_v} \tag{5.23}$$

where p_v is the vapor pressure of the working fluid, $C_1 = \alpha_o p_o V$, and V is the volume of one reach of the pipeline. This assumes isothermal compression.

The compatibility equations resulting from the Method of Characteristics for the DGCM are

$$C^+ : p^{i,j} = C_P - B_P q_u^{i,j} \tag{5.24}$$

$$C^- : p^{i,j} = C_M + B_M q_d^{i,j} \tag{5.25}$$

where Equations. 5.18, 5.19, 5.20, and 5.21 become

$$C_P = p^{i-1,j-1} + \frac{a\rho}{A} q_d^{i-1,j-1} \tag{5.26}$$

$$B_P = \frac{a\rho}{A} + \rho \frac{f\Delta x}{2dA^2} |q_d^{i-1,j-1}| \tag{5.27}$$

$$C_M = p^{i+1,j-1} - \frac{a\rho}{A} q_u^{i+1,j-1} \tag{5.28}$$

$$B_M = \frac{a\rho}{A} + \rho \frac{f\Delta x}{2dA^2} |q_u^{i+1,j-1}| \tag{5.29}$$

The solution is completed through manipulation of Equation 5.23 giving the solutions for pressure

$$p^{i,j} - p_v = -B_1 \left(1 + \sqrt{1 + B_B}\right) \tag{5.30}$$

if $B_1 < 0$ and

$$p^{i,j} - p_v = -B_1 \left(1 - \sqrt{1 + B_B}\right) \tag{5.31}$$

if $B_1 > 0$, where

$$B_B = \frac{C_1}{B_1^2} \tag{5.32}$$

$$B_1 = -B_2 \left(B_P C_M + B_M C_P + B_2 B_M B_P B_v \right) + \frac{p_v}{2} \tag{5.33}$$

$$C_4 = \frac{B_2 C_1 B_M B_P}{\psi \Delta t} \tag{5.34}$$

$$B_2 = \frac{1}{2\left(B_P + B_M\right)} \tag{5.35}$$

$$B_v = \frac{1}{\psi} \left(\frac{V_g}{2\Delta t} + (1-\psi) \left(q_d^{i,j-2} - q_u^{i,j-2} \right) \right) \tag{5.36}$$

Inaccuracy from the numerical evaluation of the square root can be problematic when $|B_B| << 1$. However, problems can be avoided with linearization of Equations. 5.30 and 5.31, such that

$$p^{i.j} - p_v = -2B_1 - \frac{C_4}{2B_1} \tag{5.37}$$

if $B_1 < 0$ and

$$p^{i.j} - p_v = fracC_4 2B_1 \tag{5.38}$$

if $B_1 > 0$. Wylie recommends this linearization be used when $|B_B| < 0.001$ [106].

5.3.5 Model Implementation

The system is simulated using a variable time step, variable order, Runga-Kutta numerical solver intended for stiff systems. The solver used is built into MATLAB (i.e., the function "ode15s"). The relative and absolute error tolerances that parameterize the solver are chosen based on a convergence study presented in Appendix A, Section A.4.1 using the medium line model.

The fMOC and DGCM models are solved on a fixed time step; therefore, the maximum step size for the variable time step solver was set to the smallest fixed time step used for the MOC solutions. Between the fixed time steps, the last solution from the pipeline model is used rather than extrapolations of the data from prior time steps. The number of segments used for these models is based on convergence studies presented in Appendix A, Section A.4.2.

Table 5.2: Simulation parameters by design case

	Design case										
	A	B	C	D	E	F	G	H	I	J	K
Simulation											
Time span	1200										
Solver error tolerance, ode15s()											
Relative	1.00E-06										
Absolute											
Pump flow, inverse fourier transformation											
Wave frequency range (rad/s)	[0.1, 10]										
Frequency bin size (rad/s)	0.005										
Random number generator seed (MATLAB function rng())	2										
Pipeline segments											
N π-lumps	6						3			6	13
fMOC	50						10	50	10	50	100
DGCM											

The number of pipeline segments in the N π-lump model were chosen to give pipeline segment lengths that are just less than 4 percent as long as the wavelength having twice the frequency of the peak wave frequency.

The simulation parameters are given in Table 5.2 and are case dependent, in general.

5.4 Results

In this section, the results of each model are compared against the results of the DGCM. This model is assumed to be the more accurate model in the set as it offers the highest fidelity and is documented to give accurate results. Where error is reported, it is calculated as

$$Error = 100\% \frac{result - DCGMresult}{DCGMresult} \tag{5.39}$$

To demonstrate the behavior of these systems, the flow and pressure results for case B are plotted in Figure 5.5 and Figure 5.6, respectively. These results are obtained using

the DGCM pipeline model. Data are shown for a 100 second portion of the total 1200 second simulation. The flow rates shown in Figure 5.5 include the flow rate for the WEC-driven pump, the load, and at the inlet and outlet of each pipe.

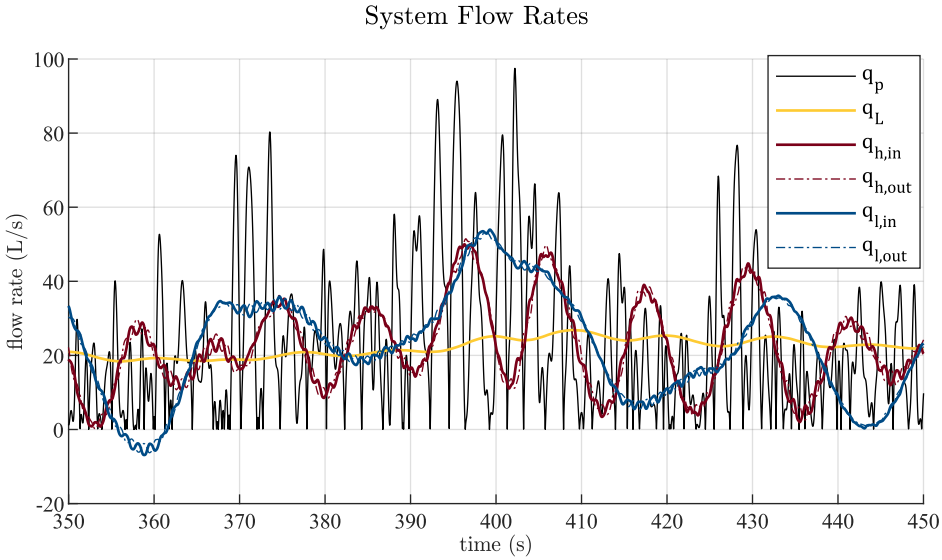

Figure 5.5: Results for flow rate within the system using the DGCM for design case B

The flow rates shown in Figure 5.5 show a considerable reduction in the variation of flow rate from between the pump and the load. However, the flow through the pipelines are still highly variable, with the flow through the low-pressure pipeline even reversing direction at around 360 s. At these flow rates, the Reynolds number is on the order of 100,000 and in the turbulent regime; combined with nonlinear resistance in the turbulent regime, this fluctuation would lead to an increase in the power loss in the pipeline. It is also interesting to point out that major variations in flow rate occur at very long time scales, about 10–20 s for the high-pressure pipeline and about 40 second for the low-pressure pipeline. The frequencies are about two orders of magnitude lower than the pipeline frequency and may be resonant frequencies of the system.

The pressures shown in Figure 5.6 are also highly variable, spanning a range of 3 MPa within the 100 s period, and show evidence of the inertive effects of the pipeline.

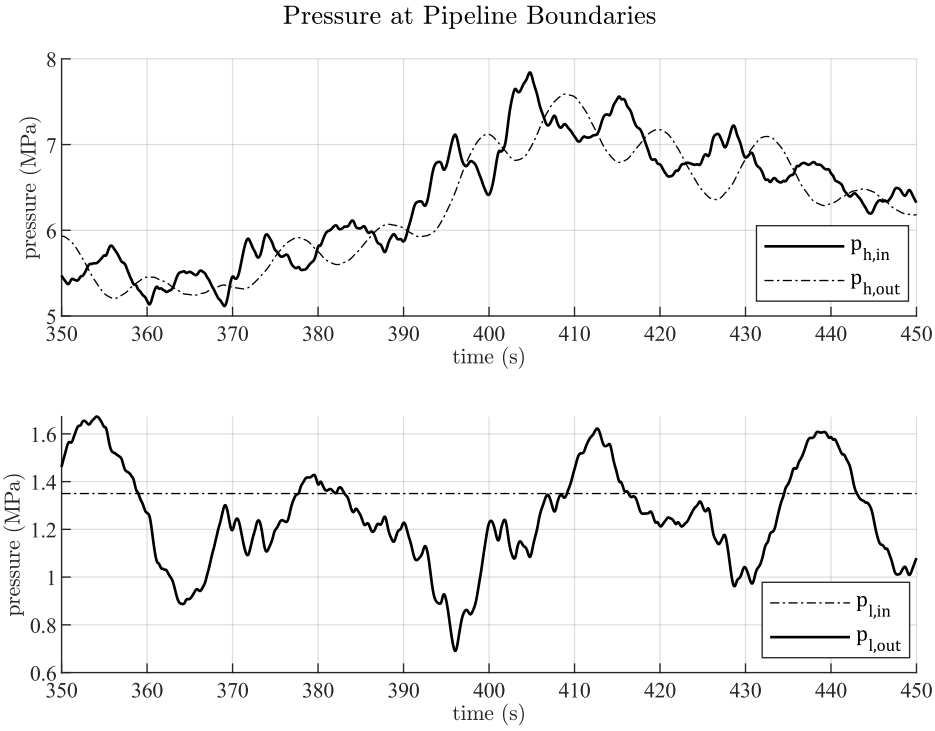

Figure 5.6: Results for pressure at the pipeline boundaries using the DGCM for design case B: (Top) high-pressure pipeline and (bottom) low-pressure pipeline

The inertive effects are especially apparent in the low-pressure pipeline where the outlet pressure rises above the inlet pressure.

Results are also given for the distribution of pressure in Figure 5.7 over a period of two seconds. These results are for case K, where it is possible for a resonant condition to arise. These data show an instance where the pressure variation within the pipeline is greater than the pressure variation at the boundaries. This behavior may have significant implications for the fatigue life of the pipeline.

The N π-lump model gives results for pressure and flow within the pipe as well. Figure 5.8 compares these to the DGCM at three points in time during the same period for case K. There is some error, but the results match reasonably well as both models are capturing the same pressure waves in the pipeline.

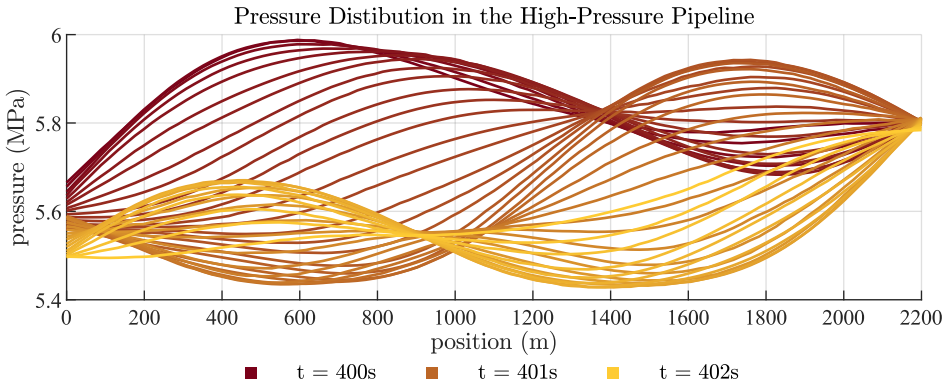

Figure 5.7: Results for the pressure distribution along the high-pressure pipeline using the DGCM for design case K. Data are plotted over two seconds in intervals of 0.05 s beginning at 400 s.

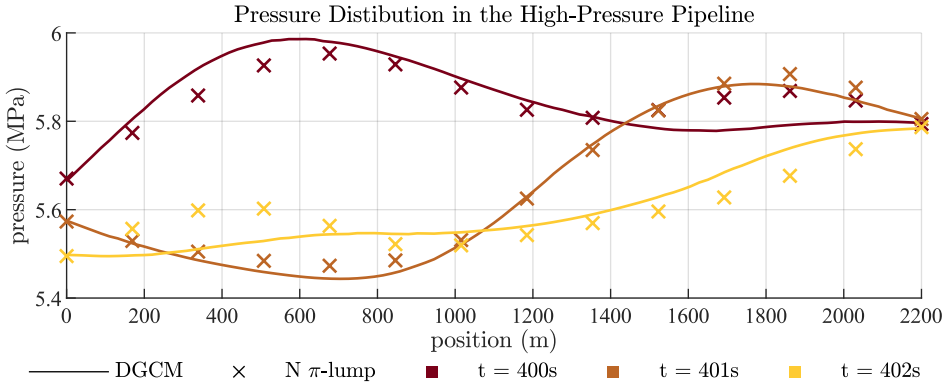

Figure 5.8: Comparison of DGCM and N π-lump model results for pressure distribution along the high-pressure pipeline. Results are for design case K.

Moving on to the design metrics, Figure 5.9 and Figure 5.10 give model results for the mean power loss in the low and high-pressure pipelines, respectively. Note that the sets of cases E, F and J and G, H, and I have identical parameters for the low-pressure pipeline, and therefore, only cases E and G are displayed from these sets in Figure 5.9. The error in results from the short line model are significant with up to a 22 percent under-prediction for the power loss in the low-pressure pipeline and 74 percent under-prediction for the high-pressure pipeline. All other models give good agreement with the DGCM. There is an exception with the high-pressure pipeline losses in design case E, where the capacitance at the pump outlet is lowest of all cases. In this case, the medium line model results over-predict the losses by 13 percent. The N π-lump model also gives higher error in design case E than in other cases but this is only about 1.9 percent error.

The standard deviations in pressure at the three accumulators are given in Figure 5.11, Figure 5.12, and Figure 5.13. Again, parameters for the low-pressure branch

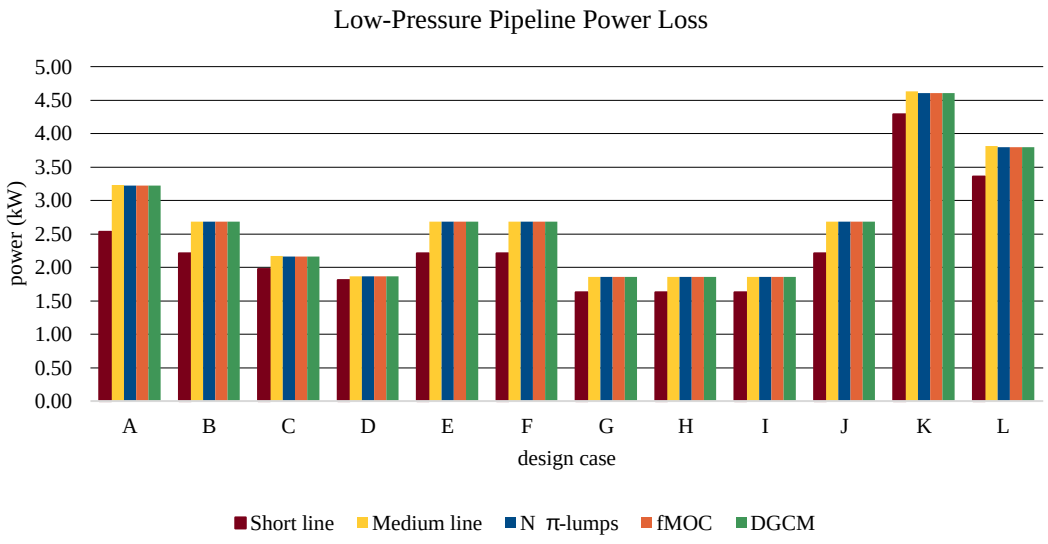

Figure 5.9: Model results for mean power loss in the low-pressure pipeline by design case

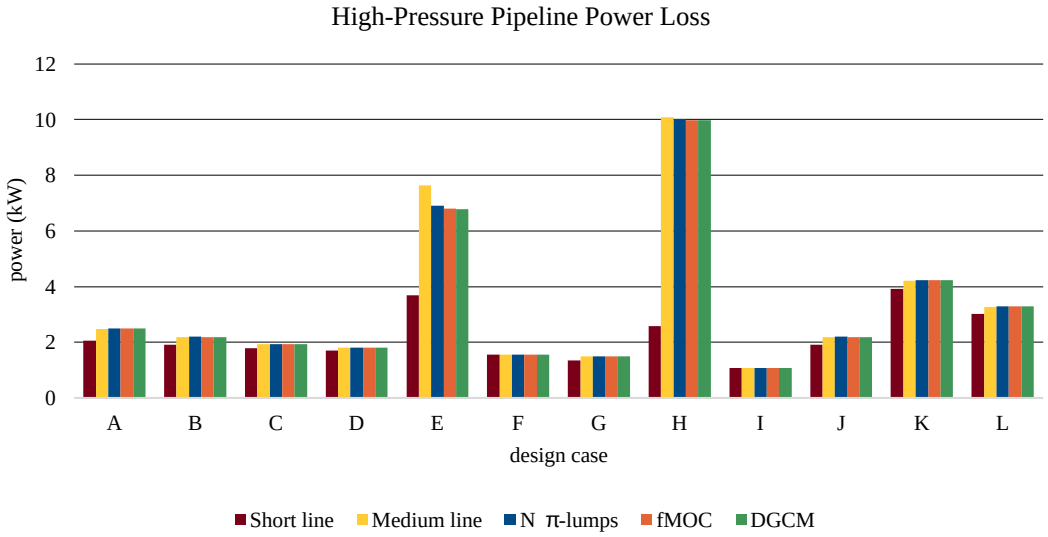

Figure 5.10: Model results for mean power loss in the high-pressure pipeline by design case

of the circuit are repeated; repeated cases are left out of Figure 5.11. As with the power loss results, the performance of the short line model is poor in predicting the variation in pressure in the offshore LPA compared to all other models, with it under-predicting the variation by up to 77 percent compared the DGCM. The medium line model over-predicts the variation but only with it being up to 2.4 percent in error while the rest of the models are in good agreement with the DGCM with less than 1 percent error.

The results for the standard deviation in the pressure in the HPAs is remarkably different than for the LPA. In many cases, the medium line and N π-lump model perform worse than the short line model in predicting the variation in pressure. Notable exceptions are design cases E and H where the variation in the offshore HPA is under-predicted by the short line model by 65 percent and 61 percent, respectively. However, even in design case E, the medium line model and N π-lump models give poorer results, over-predicting the variation by 29 and 4.4 percent error, respectively. The agreement of the models on the variation in pressure in the onshore HPA is relatively better than

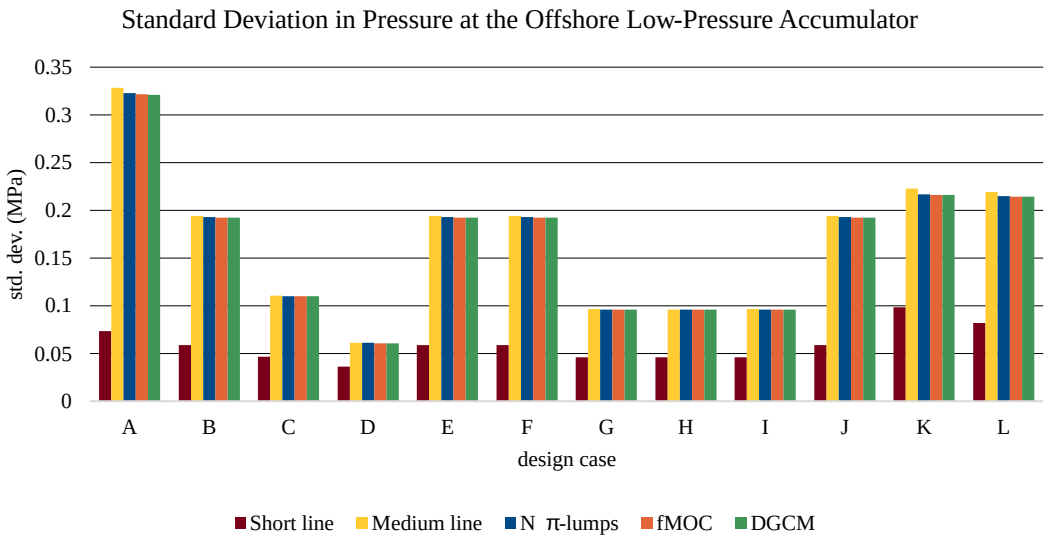

Figure 5.11: Model results for standard deviation in pressure in the offshore LPA

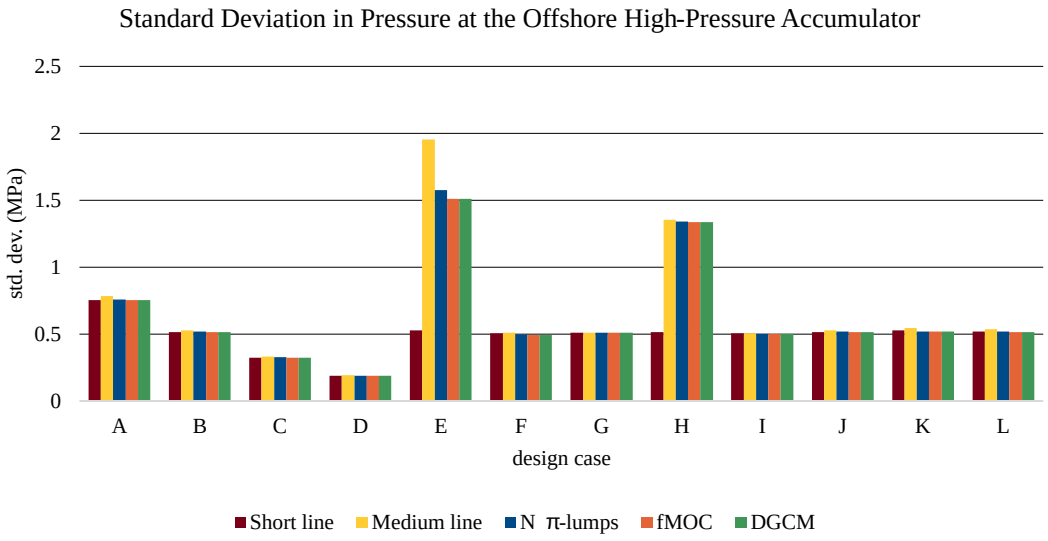

Figure 5.12: Model results for standard deviation in pressure in the offshore HPA

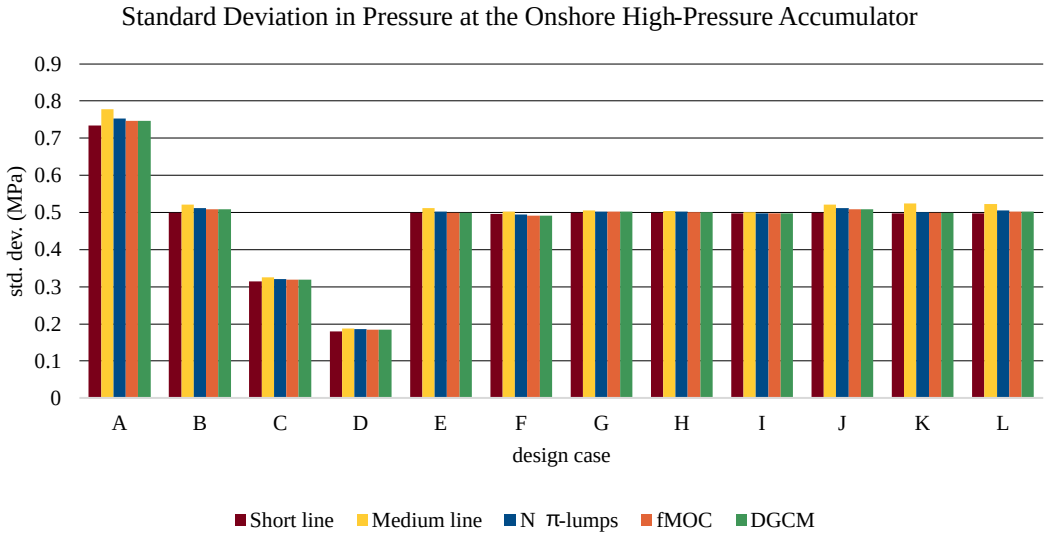

Figure 5.13: Model results for standard deviation in pressure in the onshore HPA

for the onshore HPA with a magnitude of error less than 3 percent from the short line model, less than 6 percent from the medium line model, and less that 1 percent error from the N π-lump model. The medium line model constantly over-predicts the variation across design cases and is clearly the worst performer overall.

Figure 5.14 compares the results for the peak rate of pressure change at the onshore HPA. The short line gives poor agreement with the DGCM while the other models give more favorable results. The medium line model results are typically in the range of 1 to 4 percent error. The N π-lump model gives less than 1 percent error in all cases except case B with 1.5 percent error and case F with -7 percent error.

Finally, Figure 5.15 and Figure 5.16 give results for the mean and standard deviation in the pressure differential across the WEC-driven pump, respectively. The agreement between models is very good in all cases with less than 0.2 percent error from the short line model and less than 0.05 percent error for all other models. The error for the variation in the pressure differential is relatively higher, as expected from previous results for pressure variation. Although, despite the very high error in the variation

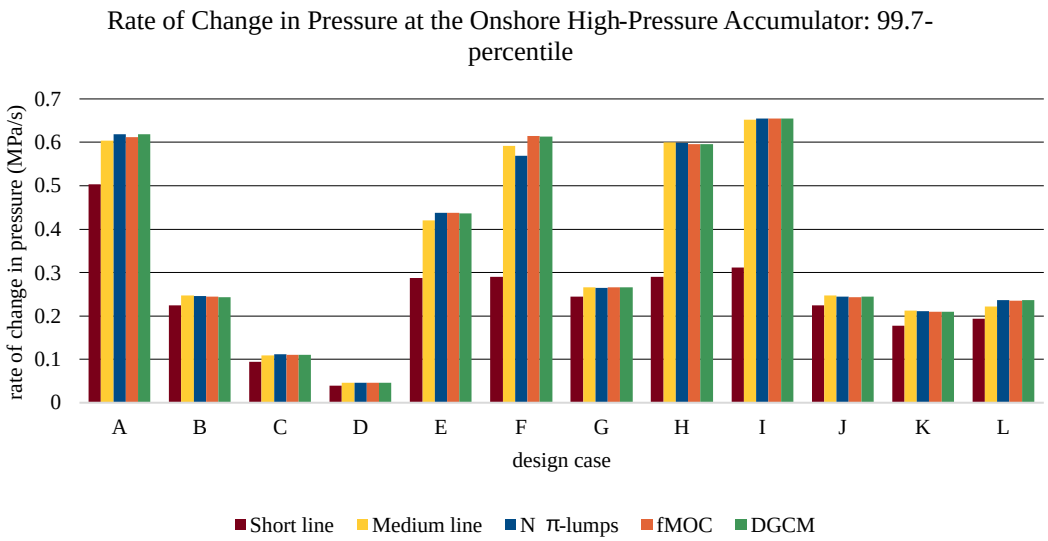

Figure 5.14: Model results for peak rate of change in pressure in the onshore HPA (99.7-percentile)

in the offshore LPA pressure shown in Figure 5.11, the magnitude of the error for all models, in all cases is less than 8 percent. The medium line model over-predicts the variation by up to 5.1 percent while the magnitude of the N π-lump model error is below 1 percent for all cases.

5.5 Discussion

The results of this study suggest that the short line model is not sufficient for design analysis. The model gives results that are up to 77 percent in error and the magnitude of error is consistently an order of magnitude higher than the other lumped parameter models. In addition, metrics are consistently under-predicted, meaning the model would not be a conservative choice for design analysis.

The medium line model gives reasonably good agreement with the DGCM results with errors typically less that 5 percent in magnitude. However, it is susceptible to giving higher error in cases where the capacitance at the WEC-driven pump is low

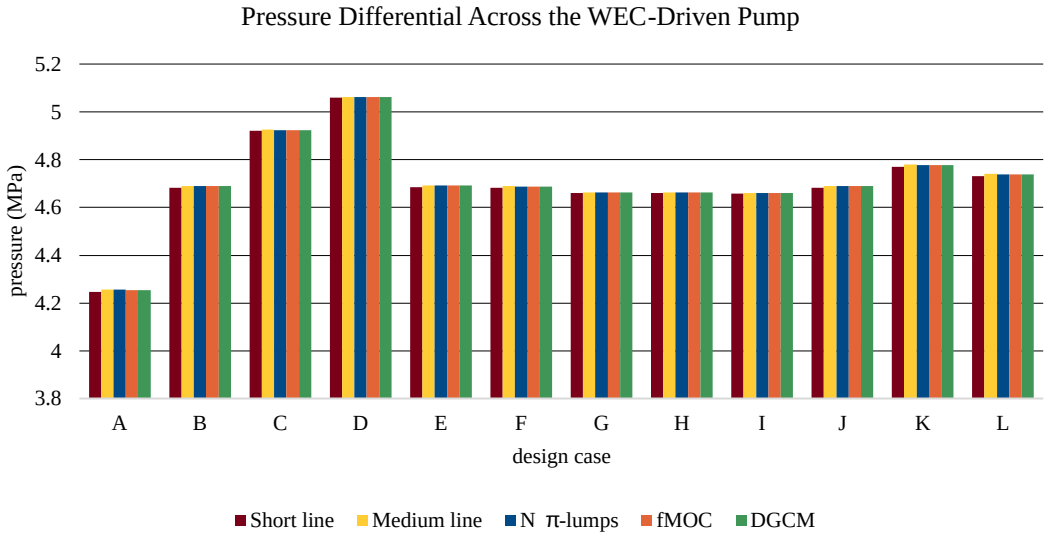

Figure 5.15: Model results for mean pressure differential across the WEC-driven pump

(e.g., design cases E and H). The N π-lump model is less susceptible in these cases

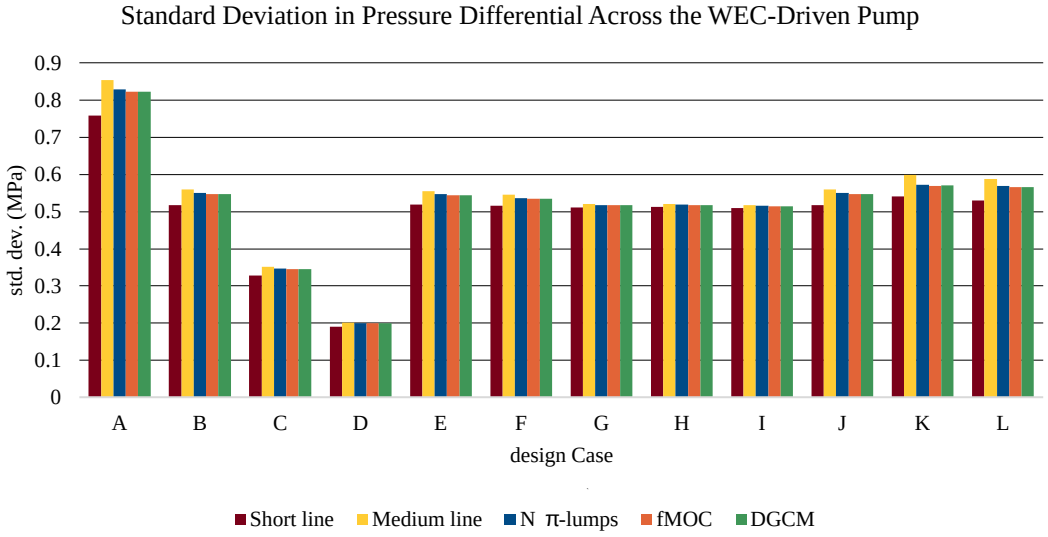

Figure 5.16: Model results for standard deviation in pressure differential across the WEC-driven pump

and gives about 5 percent error in pressure variation. For this study, the number of segments were selected to give segment lengths less than or equal to 4 percent of the dominate wavelength. More segments would likely improve its performance; however, the 4-percent rule-of-thumb appears to be sufficient for most cases.

The results from the fMOC and DGCM are in very good agreement in all cases, suggesting that the pressure dependency of the bulk modulus for fluids having entrained air is not significant at the pressures considered for these simulations. The sensitivity of the bulk modulus to pressure when entrained air is present increases significantly at lower pressures but it is not reasonable to expect that these systems are intentionally designed to operate at such low pressures. Therefore, the fMOC is expected to be adequate for analyses of stronger transients that require high accuracy. If very low pressures and/or cavitation are expected, then one should consider the DGCM.

It was noted that pressure variation within the pipeline seems to exceed the pressure variation at the boundaries. This is significant since fatigue analysis using pressure variations at the boundaries may over-predict the fatigue life of the pipeline. The N π-lump, fMOC, and DGCM could be used to give more accurate accounts of stress fluctuation within the pipeline. N π-lump was found to be in reasonable agreement with the DGCM for the pressure distribution within the pipeline and might be sufficient for this purpose; although it would be prudent to compare fatigue calculation between models to validate this claim. It would also be prudent to perform studies on convergence of fatigue metrics as a function of the number of pipeline segments.

The adequacy of the N π-lump model for predicting the given design metrics is significant for wave energy developers because available software tools (e.g., MATLAB's Simscape Fluids) may only implement lumped parameter pipeline models. With the development of WEC-Sim by the National Renewable Energy Lab [55] being carried out in MATLAB and Simulink, system modelers and designers could readily use the Simscape Fluid's implementation of the N π-lump model (called the "Segmented Pipeline" block in that software). In contrast, implementation of a distributed parameter model within

the WEC-Sim framework would require significant software development.

The study performed does not consider all possible architectures for wave energy systems. For those that differ from the system considered in this work, designers are advised to consider distributed parameter models, especially for architectures that include strong disturbances to the pipeline at higher frequencies than typical ocean wave frequencies such as rapid switching of valves in a switch-mode circuit, as with the system considered in [64]. Further work considering systems with these types of disturbances may clarify the limits of pipeline models.

5.6 Conclusion

Several pipeline models were compared in the context of a generic wave-energy PTO with realistic wave inputs. The models were compared for several design cases that explored variations in parameters such as accumulator capacitance, pipeline length, and entrained air volume fraction. Variables that would be important to the system designer were compared, such as power loss, variation in pressure, and the rate-of-change in pressure at the load (a variable specifically important to the application of wave-powered RO desalination). The results of this study suggest that for system designers interested in these metrics, the pipeline modeling guidelines found in literature can be slightly relaxed; that is, multi-segment lumped parameter models may replace distributed parameter models.

It is necessary to model the inertia of the pipeline, even for the relatively short 100-meter pipelines; otherwise, power losses and pressure variation may be under-predicted. The medium line model was still susceptible to error in design cases with low capacitance at either end of the pipeline. In these cases, one can use multiple nominal π-lumps. A reasonable rule-of-thumb is to maintain a pipeline segment length that is less than or equal to four percent of the wavelength at a frequency twice[1] the the peak wave

[1]Twice the the peak wave frequency due to rectification in the pump.

frequency .

Chapter 6

Conclusion

6.1 Review

In review, this thesis has presented three design studies and a study on modeling practices for the application of wave-powered reverse osmosis. The design studies compared hydraulic PTO architectures using three different multi-objective optimization problems. The modeling study compared methods for modeling long pipelines in design problems involving dynamics of the system.

In Chapter 2, several novel PTO architectures for wave-powered RO were introduced and compared in terms of their design performance and in the context of a realistic distribution of sea conditions. Design performance was judged based on the three objectives of having a power dense WEC-driven pump, small RO membrane module, and high permeate production. This comparative design study relied on a mixed modeling method where the WEC was modeled as a dynamic system and then characterized by a relationship between a constant PTO load and the power captured from the wave environment, and the PTO was modeled as having constant pressure and flow rate throughout the hydraulic circuit. This study found:

- Series-type PTO architectures offer a 30–74 percent reduction in the displacement of the WEC-driven pump over parallel-type architectures, while maintaining equivalent yearly production.

- Including a switch-mode power transformer in the series-type architecture improved the reduction in pump displacement to 70–92 percent.

- Varying the active RO membrane area as a function of sea conditions improved system design performance with either a 25–32 percent reduction in pump displacement, 7–41 percent reduction in installed RO membrane area, or 14–21 percent increase yearly production, while maintaining the other two objective at equivalent values.

- Varying the displacement of the WEC-driven pump as a function of sea conditions did not provide a significant improvement to the system performance.

In Chapter 3, the effect of a varying PTO load was examined for wave energy systems more generally. In this study, model predictive control was used as a machine learning method to provide constrained, optimal load control, enabling the maximum possible performance of the WEC to be characterized as a function of the practical limits of a PTO. This optimal performance was compared to a constant force load control, 'Coulomb damping' as a baseline. This study found that moment-to-moment variation of the PTO load could improve the average yearly power capture by up to 29 percent depending on values of constraints on the PTO load. A PTO load that was variable to 75 percent of the maximum load or that takes more than several seconds to ramp between the minimum and maximum value provides little to no improvement.

In Chapter 4, the consequences of a constraint on the rate-of-change in RO feed pressure, that is recommended by guidebooks on the design of reverse osmosis systems, was examined along with the effect that the PTO architecture has on the design performance when this constraint is applied. In this work, a two-way coupled, dynamic

model of the WEC/PTO system was used to simulate the pressure variations and power losses. The study found that:

- Applying the constraint in the design of the PTO results in requirement for an order of magnitude greater high-pressure accumulator volume.
- The addition of a resistive-capacitive network to the baseline, parallel-type PTO architecture, forming a second-order low-pass pressure filter in the circuit, reduced the required high-pressure accumulator volume by 48–55 percent.
- The series-type architecture required 75 percent less than the baseline, parallel-type architecture.

In Chapter 5, a comparative study on pipeline modeling techniques were performed in the context of a wave energy system. Several lumped parameter and distributed parameter models were compared in terms of their prediction of important variables, like power losses and variation in pressure. The results of each model were compared against the discrete Gas Cavity Model (DGCM) based on the method of characteristic. This study found that:

- A short line model, which only captures resistive effects, had poor performance and is not sufficient for wave energy systems.
- A medium line model perform well with error typically less than 5 percent but performed poorly when the capacitance at the WEC-driven pump is low.
- A long line model, the N π-lump model, maintained less than 5 percent error in all cases.
- The distributed parameter model based on the method of characteristic with a fixed wave speed, fMOC, had good agreement with the DGCM.

6.2 Conclusions

Together, this work provides valuable insight into the design of PTOs for wave-powered RO. The three design studies presented in Chapters 2, 3, and 4 demonstrate the significant effect that the PTO architecture design has on the performance of the system.

- Chapter 2 revealed that (1) varying the active RO membrane area as a function of sea condition has the effect of improving system performance by 7–41 percent, whether in terms of decreasing the size of components or improving the yearly average permeate production and (2) the series-type architectures provide a significant advantage in terms of the size of the WEC-driven pump with up to an order of magnitude reduction in pump displacement.

- The assumption of a constant PTO load in the modeling methods of Chapter 2 let to the conclusion that varying the volumetric displacement of the WEC-driven pump as a function of sea conditions provided no benefit to the system performance. However, the work of Chapter 3 revealed that a variable displacement pump does provide a significant benefit to the system performance when it is varied on a moment-to-moment basis, based on the variation in the incoming wave heights. Chapter 3 also provided insight into how the WEC-driven pump should be designed if it featured a variable displacement. The displacement should be able to vary down to 25–50 percent of full displacement, and it should be able to do so within a period of no more than a few seconds.

- Chapter 4 focused on the high-pressure accumulator volume required to meet a constraint on the rate-of-change in pressure at the RO feed inlet and found that applying the constraint in the design of the PTO results in an order of magnitude greater high-pressure accumulator volume but, also, that the volume requirement could be reduced by 48–75 percent with changes to the PTO architecture. The greatest advantage was with the series-type PTO which has direct control over the

pressure at the RO inlet and for which the accumulator volume requirement is a matter of power losses due to activation of pressure relief valves at the WEC-driven pump.

The ideal PTO architecture suggested by this work is a series-type PTO with a variable displacement pump and an RO membrane module that can vary the number of active RO elements. The series-type architecture consistently outperformed the parallel-type architecture in these design studies. The ability to vary the PTO load quickly and over a large range could be provided by a variable displacement, WEC-driven pump. Varying the active RO membrane area offers an additional degree of freedom in optimizing system performance as sea conditions change.

The modeling study presented in Chapter 5 provides insight for modeling practices when long pipelines are incorporated into the system. The study found that the N *pi*-lump model, which is simple lumped parameter model modeling a pipe as multiple pipe segments, is adequate for wave energy system models where metrics like power loss and pressure variation are of interest. The results of the study also support a rule-of-thumb for selecting the number of pipeline segments to be used: that is, the length of each pipe segment used to represent the pipeline should be no longer than 4 percent of the wavelength (in the working fluid) of the peak period for the sea condition. This modeling recommendation is significant because modeling software like Matlab's Simulink, where the WEC-Sim model has been developed, include this model (e.g., the "Segmented Pipeline" in Simulink's Simscape Fluids package) whereas the distributed parameters models require significant software development to be integrated with WEC-Sim.

6.3 Recommendations for Future Work

Recommendations for future work include addressing technology gaps, further exploration of PTO design problems, and further understanding of the limitations of reverse osmosis membrane modules.

Chapters 2 and 4 show significant advantages in using the series-type PTO architecture, with or without the switch-mode power transformer. These architectures operate at higher pressure than conventional RO systems and therefore availability of seawater compatible components rated at these pressure is low. Custom design would be needed to implement these architectures. This is especially true for the high-speed valves used in the switch-mode power transformer. This recommends future work to understand the design of seawater compatible hydraulic machines.

Chapters 2 also shows an advantage in implementing an RO membrane module that can vary the quantity of active membrane area. This could be accomplished by isolating pressure vessels that contain the membrane elements so they can be taken out of and put into service individually. Two issues related to the performance advantage are that (1) there is a costs of switching pressure vessels on and off since the the pressure must be ramped up and down slowly and the membrane elements must be flush to remove any saltwater solution and (2) the active membrane area is limited to discrete values rather than being continuously variable. A recommendation for future work is to examine the effect of these issues to performance. Specific questions to address are:

- What is the energy cost of switching RO pressure vessels on an off?
- How frequently would this switching need to occur based on changes in the sea conditions?
- What is the optimal RO module configuration for addressing the limitation to discrete quantities of membrane area?

The integration of the RO module into the PTO, where large pressure fluctuation is inevitable, brings concern for damage to the RO membranes. Furthermore, the practice of varying the active membrane area by switching individual membrane pressure vessels on and off would increase the number of large stress cycles that contribute to fatigue damage. The based on the work in Chapter 4, limiting the magnitude of pressure

variation comes at a significant cost, yet, the specific constraint that was imposed in that study, the constraint on the pressure rate-of-change, lacks substantiation. Both the mechanism of failure, or degradation, and the degree of significance remain unknown. It is recommended that damage and failure of RO membrane elements be studied for the purpose of recommending well-founded design constraints and/or damage models that can be integrated in to the design of the a PTO for wave-powered RO. Such knowledge will reduce risk and may allow for more economical designs if the current recommended rate-of-change constraint is found to be too conservative or simply not applicable to operation outside start-up and shut-down procedures.

The work of this thesis expands the scope of understanding in the design of PTOs for wave-powered RO and highlights a path toward higher performing designs. The design studies formulated and examined in this work may be reapplied in future projects that aim to construct a wave-powered RO system and the modeling efforts in this work may serve as a point of reference for modeling similar systems.

References

[1] Mekonnen, M. M. and Hoekstra, A. Y., 2016, "Four billion people facing severe water scarcity," Science advances, **2**(2), p. e1500323.

[2] Rijsberman, F. R., 2006, "Water scarcity: Fact or fiction?" Agricultural Water Management, **80**(1), pp. 5–22, Special Issue on Water Scarcity: Challenges and Opportunities for Crop Science.

[3] Shiklomanov, I. A., 1993, "World fresh water resources," *Water in crisis; a guide to the world's fresh water resources*, Oxford University Press, New York, pp. 13–24.

[4] Shiklomanov, I. A., 2000, "Appraisal and assessment of world water resources," Water international, **25**(1), pp. 11–32.

[5] Greenlee, L. F., Lawler, D. F., Freeman, B. D., Marrot, B., and Moulin, P., 2009, "Reverse osmosis desalination: water sources, technology, and today's challenges," Water research, **43**(9), pp. 2317–2348.

[6] Ghaffour, N., Missimer, T. M., and Amy, G. L., 2013, "Technical review and evaluation of the economics of water desalination: Current and future challenges for better water supply sustainability," Desalination, **309**, pp. 197–207.

[7] García Rodríguez, L., 2003, "Renewable energy applications in desalination: state of the art," Solar Energy, **75**(5), pp. 381–393, Solar Desalination.

[8] Kalogirou, S. A., 2005, "Seawater desalination using renewable energy sources," Progress in energy and combustion science, **31**(3), pp. 242–281.

[9] Leijon, J. and Boström, C., 2018, "Freshwater production from the motion of ocean waves – A review," Desalination, **435**, pp. 161–171.

[10] "American-Made Challenges," `https://americanmadechallenges.org/`, Accessed: Jul. 06, 2020.

[11] Folley, M., Suarez, B. P., and Whittaker, T., 2008, "An autonomous wave-powered desalination system," Desalination, **220**(1-3), pp. 412–421.

[12] Yu, Y.-H., Tom, N., and Jenne, D., 2018, "Numerical analysis on hydraulic power take-off for wave energy converter and power smoothing methods," *International Conference on Offshore Mechanics and Arctic Engineering*, Vol. 51319, American Society of Mechanical Engineers, p. V010T09A043.

[13] "Resolute Marine Energy," `http://www.resolutemarine.com/`, Accessed: Apr. 15, 2019.

[14] Nolan, G. and Ringwood, J., 2006, "Control of a heaving buoy wave energy converter for potable water production," .

[15] Gunn, K. and Stock-Williams, C., 2012, "Quantifying the global wave power resource," Renewable energy, **44**, pp. 296–304.

[16] Dudley, B., 2019, "BP statistical review of world energy 2019. London," .

[17] IEA, I., 2015, "International energy agency. key world energy statistics," Key World Energy Statistics.

[18] Prieto, L. F., Rodríguez, G. R., and Rodríguez, J. S., 2019, "Wave energy to power a desalination plant in the north of Gran Canaria Island: Wave resource, socioeconomic and environmental assessment," Journal of environmental management, **231**, pp. 546–551.

[19] Yu, Y.-H. and Jenne, D., 2017, "Analysis of a wave-powered, reverse-osmosis system and its economic availability in the United States," *International Conference on Offshore Mechanics and Arctic Engineering*, Vol. 57786, American Society of Mechanical Engineers, p. V010T09A032.

[20] Hansen, R. H., Andersen, T. O., and Pedersen, H. C., 2011, "Model based design of efficient power take-off systems for wave energy converters," *Proceedings of the 12th Scandinavian International Conference on Fluid Power, Tampere, Finland*, pp. 18–20.

[21] Tedeschi, E., Carraro, M., Molinas, M., and Mattavelli, P., 2011, "Effect of control strategies and power take-off efficiency on the power capture from sea waves," IEEE Transactions on Energy Conversion, **26**(4), pp. 1088–1098.

[22] Wijmans, J. and Baker, R., 1995, "The solution-diffusion model: a review," Journal of Membrane Science, **107**(1), pp. 1–21.

[23] Kucera, J., 2015, *Reverse Osmosis: Industrial Processes and Applications*, Scrivener Publishing, Salem, Massachusetts.

[24] Yu, Y.-H. and Jenne, D., 2018, "Numerical modeling and dynamic analysis of a wave-powered reverse-osmosis system," Journal of marine science and engineering, **6**(4), p. 132.

[25] Dupont, 2023, *Filmtec™ Reverse Osmosis Membranes Technical Manual*, Dupont Water Solutions, Edina, MN, USA, Form No. 45-D01504-en, Rev. 16.

[26] Ruiz-García, A. and de la Nuez-Pestana, I., 2018, "A computational tool for designing BWRO systems with spiral wound modules," Desalination, **426**, pp. 69–77.

[27] Miranda, M. S. and Infield, D., 2003, "A wind-powered seawater reverse-osmosis system without batteries," Desalination, **153**(1), pp. 9–16.

[28] Wilf, M. and Awerbuch, L., 2007, *The guidebook to membrane desalination technology: reverse osmosis, nanofiltration and hybrid systems: process, design, applications and economics*, Balaban Desalination Publications, L'Aquila, Italy.

[29] Folley, M. and Whittaker, T., 2009, "The cost of water from an autonomous wave-powered desalination plant," Renewable Energy, **34**(1), pp. 75–81.

[30] Cargo, C., Hillis, A., and Plummer, A., 2016, "Strategies for active tuning of Wave Energy Converter hydraulic power take-off mechanisms," Renewable Energy, **94**, pp. 32–47.

[31] Boccotti, P., 2000, *Wave mechanics for ocean engineering*, Elsevier.

[32] Hasselmann, K., Barnett, T. P., Bouws, E., Carlson, H., Cartwright, D. E., Enke, K., Ewing, J., Gienapp, A., Hasselmann, D., Kruseman, P., et al., 1973, "Measurements of wind-wave growth and swell decay during the Joint North Sea Wave Project (JONSWAP)." Ergaenzungsheft zur Deutschen Hydrographischen Zeitschrift, Reihe A.

[33] Falnes, J. and Kurniawan, A., 2020, *Ocean waves and oscillating systems: linear interactions including wave-energy extraction*, Vol. 8, Cambridge university press.

[34] Davies, P., 2005, "Wave-powered desalination: resource assessment and review of technology," Desalination, **186**(1-3), pp. 97–109.

[35] Drew, B., Plummer, A. R., and Sahinkaya, M. N., 2009, "A review of wave energy converter technology," Proceedings of the Institution of Mechanical Engineers, Part A: Journal of Power and Energy, **223**(8), pp. 887–902.

[36] de O. Falcão, A. F., 2010, "Wave energy utilization: A review of the technologies," Renewable and Sustainable Energy Reviews, **14**(3), pp. 899–918.

[37] Ahamed, R., McKee, K., and Howard, I., 2020, "Advancements of wave energy converters based on power take off (PTO) systems: A review," Ocean Engineering, **204**, p. 107248.

[38] Maria-Arenas, A., Garrido, A. J., Rusu, E., and Garrido, I., 2019, "Control Strategies Applied to Wave Energy Converters: State of the Art," Energies, **12**(16).

[39] Evans, D. V., 1981, "Power From Water Waves," Annual Review of Fluid Mechanics, **13**, pp. 157–187.

[40] Falnes, J., 2002, "Optimum Control of Oscillation of Wave-Energy Converters," International Journal of Offshore and Polar Engineering, **12**.

[41] Babarit, A., Guglielmi, M., and Clément, A. H., 2009, "Declutching control of a wave energy converter," Ocean Engineering, **36**(12), pp. 1015–1024.

[42] Clément, A. and Babarit, A., 2012, "Discrete control of resonant wave energy devices," Philosophical Transactions of the Royal Society A: Mathematical, Physical and Engineering Sciences, **370**(1959), pp. 288–314.

[43] Plummer, A. and Schlotter, M., 2009, "Investigating the performance of a hydraulic power take-off," *Proceedings of the eight European wave and tidal energy conference, Uppsala*, pp. 729–735.

[44] Cargo, C., Hillis, A., and Plummer, A., 2014, "Optimisation and control of a hydraulic power take-off unit for a wave energy converter in irregular waves,"

Proceedings of the Institution of Mechanical Engineers, Part A: Journal of Power and Energy, **228**(4), pp. 462–479.

[45] Ehsan, M., Rampen, W. H. S., and Salter, S. H., 1997, "Modeling of Digital-Displacement Pump-Motors and Their Application as Hydraulic Drives for Nonuniform Loads ," Journal of Dynamic Systems, Measurement, and Control, **122**(1), pp. 210–215.

[46] Costello, R., Ringwood, J., and Weber, J., 2011, "Comparison of two alternative hydraulic PTO concepts for wave energy conversion," *Proceedings of the 9th European wave and tidal energy conference (EWTEC)*.

[47] Dominic Dießel, L. V., Garth Bryans and Murrenhoff, H., 2015, "Wavepod a transmission for wave energy converters – set-up and testing," International Journal of Fluid Power, **16**(2), pp. 75–82.

[48] de O. Falcão, A. F., 2007, "Modelling and control of oscillating-body wave energy converters with hydraulic power take-off and gas accumulator," Ocean Engineering, **34**(14), pp. 2021–2032.

[49] Cargo, C. J., Plummer, A. R., Hillis, A. J., and Schlotter, M., 2012, "Determination of optimal parameters for a hydraulic power take-off unit of a wave energy converter in regular waves," Proceedings of the Institution of Mechanical Engineers, Part A: Journal of Power and Energy, **226**(1), pp. 98–111.

[50] Hansen, R. H., Kramer, M. M., and Vidal, E., 2013, "Discrete displacement hydraulic power take-off system for the wavestar wave energy converter," Energies, **6**(8), pp. 4001–4044.

[51] Hicks, D. C., Mitcheson, G. R., Pleass, C. M., and Salevan, J. F., 1989, "Delbouy: ocean wave-powered seawater reverse osmosis desalination systems," Desalination, **73**, pp. 81–94.

[52] Whittaker, T. and Folley, M., 2012, "Nearshore oscillating wave surge converters and the development of Oyster," Philosophical Transactions of the Royal Society A: Mathematical, Physical and Engineering Sciences, **370**(1959), pp. 345–364.

[53] Hicks, D., Pleass, C., and Mitcheson, G., 1988, "DELBUOY: wave-powered seawater desalination system," *OCEANS '88. 'A Partnership of Marine Interests'. Proceedings*, pp. 1049–1054 vol.3, doi:10.1109/OCEANS.1988.23660.

[54] Bacelli, G., Gilloteaux, J.-C., and Ringwood, J., 2009, "A predictive controller for a heaving buoy producing potable water," *2009 European Control Conference (ECC)*, pp. 3755–3760, doi:10.23919/ECC.2009.7074984.

[55] Ruehl, K. M., Michelen, C., Yu, Y.-H., and Lawson, M., 2014, "Development and demonstration of the WEC-Sim wave energy converter simulation tool," Sandia National Lab.(SNL-NM), Albuquerque, NM (United States).

[56] Mi, J., Wu, X., Capper, J., Li, X., Shalaby, A., Chung, U., Datla, R., Hajj, M., and Zuo, L., 2022, "Ocean Wave Powered Reverse Osmosis Desalination: Design, Modeling and Test Validation," IFAC-PapersOnLine, **55**(37), pp. 782–787.

[57] Mi, J., Wu, X., Capper, J., Li, X., Shalaby, A., Wang, R., Lin, S., Hajj, M., and Zuo, L., 2023, "Experimental investigation of a reverse osmosis desalination system directly powered by wave energy," Applied Energy, **343**, p. 121194.

[58] Suchithra, R., Das, T. K., Rajagopalan, K., Chaudhuri, A., Ulm, N., Prabu, M., Samad, A., and Cross, P., 2022, "Numerical modelling and design of a small-scale wave-powered desalination system," Ocean Engineering, **256**, p. 111419.

[59] Brodersen, K. M., Bywater, E. A., Lanter, A. M., Schennum, H. H., Furia, K. N., Sheth, M. K., Kiefer, N. S., Cafferty, B. K., Rao, A. K., Garcia, J. M., et al., 2022, "Direct-drive ocean wave-powered batch reverse osmosis," Desalination, **523**, p. 115393.

[60] Simmons, J. W. and Van de Ven, J. D., 2023, "A Comparison of Power Take-Off Architectures for Wave-Powered Reverse Osmosis Desalination of Seawater with Co-Production of Electricity," Energies, **16**(21), p. 7381.

[61] Ylänen, M. M. and Lampinen, M. J., 2014, "Determining optimal operating pressure for AaltoRO–A novel wave powered desalination system," Renewable energy, **69**, pp. 386–392.

[62] Folley, M., Whittaker, T., and van't Hoff, J., 2007, "The design of small seabed-mounted bottom-hinged wave energy converters," *Proceedings of the 7th European wave and tidal energy conference*, Vol. 455, Citeseer, p. 312.

[63] Fulbright, N. J., Boyce-Erickson, G. C., Chase, T. R., Li, P. Y., and Van de Ven, J. D., 2019, "Automated Design and Analysis of a Variable Displacement Linkage Motor," p. V001T01A036, doi:10.1115/FPMC2019-1677.

[64] Simmons, J. W. and Van de Ven, J. D., 2019, "Switch-mode power transformer in a wave-powered, reverse osmosis desalination plant," *Fluid Power Systems Technology*, Vol. 59339, American Society of Mechanical Engineers, p. V001T01A020.

[65] "Oyster 1," `http://www.aquamarinepower.com/technologies/oyster-1/`, Accessed: Nov. 29, 2010.

[66] Dallman, A. R. and Neary, V. S., 2014, "Characterization of US Wave Energy Converter (WEC) Test Sites: A Catalogue of Met-Ocean Data." Sandia National Lab.(SNL-NM), Albuquerque, NM (United States).

[67] "WAVE Water Treatment Design Software," `https://www.dupont.com/water/resources/design-software.html`, [Accessed Aug 21, 2023].

[68] van't Hoff, J., 2009, "Hydrodynamic modelling of the oscillating wave surge converter," Ph.D. thesis, Queen's University Belfast.

[69] Cummins, W., 1962, "The impulse response function and ship motions," David Taylor Model Basin Washington DC.

[70] Perez, T. and Fossen, T. I., 2009, "A Matlab Toolbox for Parametric Identification of Radiation-Force Models of Ships and Offshore Structures," Modeling, Identification and Control, **30**(1), pp. 1–15.

[71] Babarit, A. and Delhommeau, G., 2015, "Theoretical and numerical aspects of the open source BEM solver NEMOH," *11th European wave and tidal energy conference (EWTEC2015)*.

[72] Ruehl, K., Michelen, C., Kanner, S., Lawson, M., and Yu, Y.-H., 2014, "Preliminary verification and validation of WEC-Sim, an open-source wave energy converter design tool," *International conference on offshore mechanics and arctic engineering*, Vol. 45547, American Society of Mechanical Engineers, p. V09BT09A040.

[73] Linjama, M. et al., 2011, "Digital fluid power: State of the art," *Proceedings of The Twelfth Scandinavian International Conference on Fluid Power, Tampere, Finland*.

[74] Simmons, J. W. and Van de Ven, J. D., 2023, "Limits on the Range and Rate of Change in Power Take-Off Load in Ocean Wave Energy Conversion: A Study Using Model Predictive Control," Energies, **16**(16), p. 5909.

[75] Hals, J., Falnes, J., and Moan, T., 2011, "A comparison of selected strategies for adaptive control of wave energy converters," Journal of Offshore Mechanics and Arctic Engineering, **133**(3).

[76] Coe, R. G., Bacelli, G., Wilson, D. G., Abdelkhalik, O., Korde, U. A., and Robinett III, R. D., 2017, "A comparison of control strategies for wave energy converters," International journal of marine energy, **20**, pp. 45–63.

[77] O'Sullivan, A. C. and Lightbody, G., 2017, "Co-design of a wave energy converter using constrained predictive control," Renewable energy, **102**, pp. 142–156.

[78] Schwenzer, M., Ay, M., Bergs, T., and Abel, D., 2021, "Review on model predictive control: An engineering perspective," The International Journal of Advanced Manufacturing Technology, **117**(5-6), pp. 1327–1349.

[79] Faedo, N., Olaya, S., and Ringwood, J. V., 2017, "Optimal control, MPC and MPC-like algorithms for wave energy systems: An overview," IFAC Journal of Systems and Control, **1**, pp. 37–56.

[80] Ringwood, J. V., 2020, "Wave energy control: status and perspectives 2020," IFAC-PapersOnLine, **53**(2), pp. 12271–12282, 21st IFAC World Congress.

[81] Li, G. and Belmont, M. R., 2014, "Model predictive control of sea wave energy converters–Part I: A convex approach for the case of a single device," Renewable Energy, **69**, pp. 453–463.

[82] Liang, H., Qiao, D., Wang, X., Zhi, G., Yan, J., Ning, D., and Ou, J., 2023, "Energy capture optimization of heave oscillating buoy wave energy converter based on model predictive control," Ocean Engineering, **268**, p. 113402.

[83] Salter, S. H., Taylor, J., and Caldwell, N., 2002, "Power conversion mechanisms for wave energy," Proceedings of the Institution of Mechanical Engineers, Part M: Journal of Engineering for the Maritime Environment, **216**(1), pp. 1–27.

[84] Korde, U. A., 2002, "Latching control of deep water wave energy devices using an active reference," Ocean engineering, **29**(11), pp. 1343–1355.

[85] Babarit, A., Duclos, G., Clément, A., and Gilloteaux, J.-C., 2005, "Latching control of a power take off oscillator carried by a wave activated body," *Proc. 20th International Workshop on Water Waves and Floating Bodies, pages xxx—yyy.*

[86] Hansen, A. H., Asmussen, M. F., and Bech, M. M., 2018, "Model predictive control of a wave energy converter with discrete fluid power power take-off system," Energies, **11**(3), pp. 1–17.

[87] Gieske, P., 2007, "Model predictive control of a wave energy converter: Archimedes wave swing," Master's thesis, Delft University of Technology.

[88] Cretel, J. A., Lightbody, G., Thomas, G. P., and Lewis, A. W., 2011, "Maximisation of energy capture by a wave-energy point absorber using model predictive control," IFAC Proceedings Volumes, **44**(1), pp. 3714–3721.

[89] Sitterley, K. A., Cath, T. J., Jenne, D. S., Yu, Y.-H., and Cath, T. Y., 2022, "Performance of reverse osmosis membrane with large feed pressure fluctuations from a wave-driven desalination system," Desalination, **527**, p. 115546.

[90] Das, T. K., Folley, M., Lamont-Kane, P., and Frost, C., 2024, "Performance of a SWRO membrane under variable flow conditions arising from wave powered desalination," Desalination, **571**, p. 117069.

[91] Bull, D. and Dallman, A., 2017, "Wave Energy Prize Experimental Sea State Selection," p. V010T09A025, doi:10.1115/OMAE2017-62675.

[92] McCandlish, D. and Dorey, R. E., 1984, "The Mathematical Modelling of Hydrostatic Pumps and Motors," Proceedings of the Institution of Mechanical Engineers, Part B: Management and engineering manufacture, **198**(3), pp. 165–174.

[93] Simmons, J. W. and Van de Ven, J. D., 2021, "Pipeline Model Fidelity for Wave Energy System Models," *Fluid Power Systems Technology*, Vol. 85239, American Society of Mechanical Engineers, p. V001T01A011.

[94] Wang, K., Abdalla, A. A., Khaleel, M. A., Hilal, N., and Khraisheh, M. K., 2017, "Mechanical properties of water desalination and wastewater treatment membranes," Desalination, **401**, pp. 190–205.

[95] Grainger, J. J. and Stevenson Jr, W. D., 1994, *Power system analysis*, McGraw-Hill, London, UK.

[96] Watton, J., 2009, *Fundamentals of fluid power control*, Cambridge University Press, New York, NY.

[97] Ghidaoui, M. S., Zhao, M., McInnis, D. A., and Axworthy, D. H., 2005, "A review of water hammer theory and practice," Appl. Mech. Rev., **58**(1), pp. 49–76.

[98] Watton, J. and Tadmori, M., 1988, "A comparison of techniques for the analysis of transmission line dynamics in electrohydraulic control systems," Applied mathematical modelling, **12**(5), pp. 457–466.

[99] Soumelidis, M. I., Johnston, D. N., Edge, K. A., and Tilley, D. G., 2005, "A comparative study of modelling techniques for laminar flow transients in hydraulic pipelines," *Proceedings of the JFPS International Symposium on Fluid Power*, Vol. 2005, The Japan Fluid Power System Society, Paper No. 6, pp. 100–105.

[100] Leon, A., Ghidaoui, M. S., Schmidt, A. R., and García, M. H., 2007, "An efficient finite-volume scheme for modeling water hammer flows," Journal of Water Management Modeling.

[101] Zhou, L., Li, Y., Zhao, Y., Ou, C., and Zhao, Y., 2021, "An accurate and efficient scheme involving unsteady friction for transient pipe flow," Journal of Hydroinformatics, **23**(4), pp. 879–896.

[102] Krus, P., Weddfelt, K., and Palmberg, J.-O., 1994, "Fast pipeline models for simulation of hydraulic systems," Journal of Dynamic Systems, and Control.

[103] Johnston, N., 2012, "The transmission line method for modelling laminar flow of liquid in pipelines," Journal of Systems and Control Engineering, **226**(5), pp. 586–597.

[104] Wylie, E. B., 1965, "Pressure Transients in Viscous Fluid Systems," Journal of basic engineering, **87**(4), pp. 1089–1089.

[105] Yudell, A. C. and Van de Ven, J. D., 2017, "Experimental validation of a time domain cavitation model for switched inertance circuits," *ASME/BATH 2017 Symposium on Fluid Power and Motion Control, FPMC 2017*.

[106] Wylie, E. B., Streeter, V. L., and Suo, L., 1993, *Fluid transients in systems*, Vol. 1, Prentice Hall, Englewood Cliffs, NJ.

Appendix A

Convergence Studies

A.1 Introduction

This appendix documents convergence studies for the numerical simulation methods used throughout this work.

Section A.2 presents the studies performed for the hydrodynamic WEC model. Sub-section A.2.1 presents the method used to construct the wave excitation force and wave elevation, both of which are inputs to the hydrodynamic WEC model developed in Section 2.4.2, and presents a convergence study for the number of wave frequency components used in that construction. Sub-section A.2.2 presents a convergence study for the time-step size used in the numerical solution of the dynamic WEC model used for the design studies presented in Chapters 2 and 3. Sub-section A.2.3 presents a convergence study for the length of the simulations performed for those design studies.

Section A.3 presents the studies performed for the coupled dynamic WEC/PTO model used in the study presented in Chapter 4. Sub-section A.3.1 presents a convergence study for the the time-step size used in the numerical solution of the coupled, dynamic WEC/PTO model. Sub-section A.3.2 presents a convergence study for the length of the simulations performed for the design study.

Section A.4 presents the studies performed for the simulations used in the pipeline modeling study presented in Chapter 5. Sub-section A.4.1 presents a convergence study for the tolerance parameters of the variable time-step, numerical ODE solver used. Sub-section A.4.2 presents a convergence study on the number of pipeline segments used for the method of characteristics based pipeline models.

A.2 Hydrodynamic WEC model Simulations

This section present studies for the simulation parameters used in simulating the hydrodynamic WEC model. The simulations for these studies were performed for a single sea state having a significant wave height of 2.75 m and a peak period of 12 seconds. The PTO is represented by a constant reaction force with a value of 4 MNm.

A.2.1 Irregular Wave Construction and Convergence

The construction of the wave elevation and wave excitation force in the hydrodynamic WEC model developed in Chapter 2 follows from superposition of trigonometric functions with amplitude determined from a power spectral density function (PSD). Specifically, the amplitude is determined from the definite integral of the PSD in discrete bins. The discretization of the PSD was performed using an equal energy method where the definite integral of the PSD for each bin is equal. The approach taken in this work is to:

1. specify the number of discrete bins (i.e., the number of frequency components)
2. calculate the indefinite integral of the PSD, numerically, as a function of frequency with a dense grid of values (1,000,000 grid points were used in this work.)
3. determine the target value for the definite integral of each bin by dividing the maximum value for the indefinite integral of the PSD by the number of bins

4. set the lower bound of the current bin equal to the upper bound of the previous bin

   Note A: For the first bin, set the lower bound to be a significant frequency. In this work, the first frequency is use where the indefinite integral of the PSD exceeds exceeds 1 percent of the target value for the definite integral of each bin.

5. find the upper bound of the current bin for which the definite integral in the bin is equal to the target value

   Note B: Because the integral is calculated numerically, the first frequency for which the definite integral in the bin exceeds the target value should be selected.

6. assign the average of the upper and lower bound of the bin as the frequency representing the bin (ω_i) and set the bin width $\Delta\omega_i$ as the difference between the upper and lower bound of the bin[1]

7. repeat steps 4 through 6 until all bins are determined

An example for the resulting discretization using this method is given in Figure A.1. This shows the assigned frequencies for each bin, with a total of twenty discrete bins.

The number of frequency components used to construct the wave elevation and wave excitation force in this work was selected based on the convergence of results for the mean power captured by the WEC and the error of the numerically calculated integral of the power spectral density function. Figure A.2 shows the mean power captured by the WEC in 2000-second long simulations as a function the number of discretization. These results do not demonstrate a clear convergence because, for each discretization of the PSD, unique wave elevation and excitation force signals are constructed with the only similarity being the frequency content; there is no convergence to an ideal signal

[1] An improvement to this method could include finding the centroid of the definite integral of each bin and assigning that frequency as representing the bin in Step 6. This would remove the need for Note A in Step 4. Instead the lower bound can be set arbitrarily low.

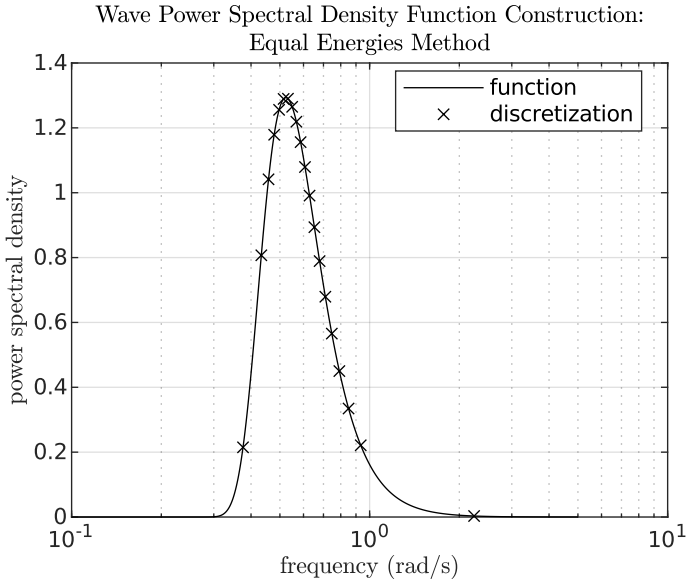

Figure A.1: Example discretization of the wave elevation spectral density function using the equal energy method.

using these methods.[2] However, these values show only about ten percent deviation about a mean.

Judgment of the signal construction is also be made based on the error between the indefinite integral of the original PSD and the sum of the definite integrals for each bin. The later is calculated as the product of the bin width and value of the PSD evaluated at the center of each bin (the frequency assigned as representing to the bin in Step 6). These results are given in Figure A.3 and show an error between 1 and 2 percent for 100 discretizations and between 0.1 and 0.2 percent for 1000 discretizations. The studies presented in Chapters 2, 3, and 4 used 1000 frequency components.

[2]It is important to note this behavior for the design of a study. Inputs to the model should be identical for each simulation in a study. For the wave elevation and wave excitation force, this includes seeding the random number generator used to give random phase values for each frequency component and using the same discretization of the PSD in the frequency domain.

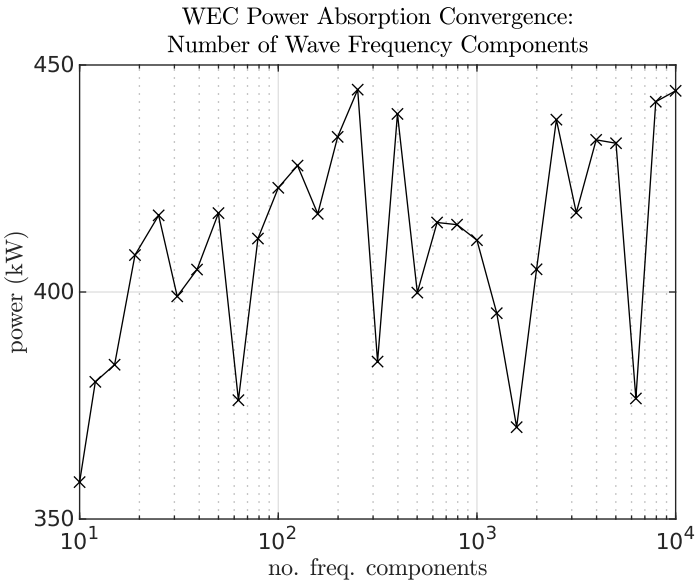

Figure A.2: Convergence results for the number of wave frequency components: mean WEC power capture.

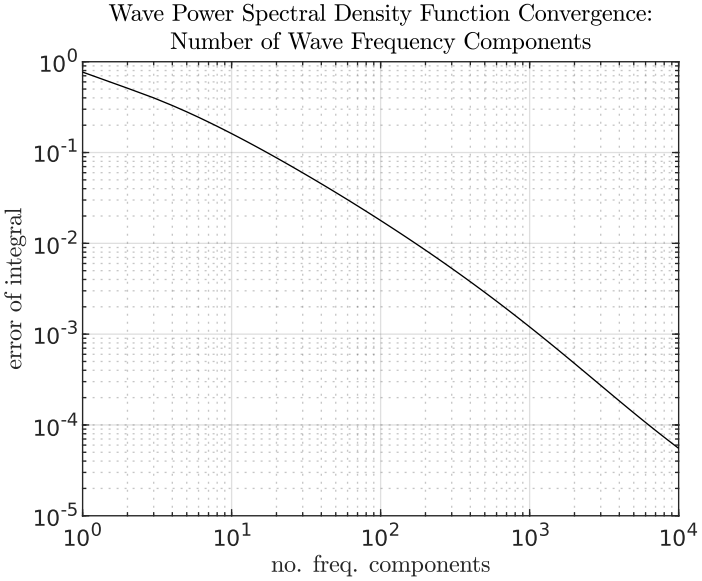

Figure A.3: Convergence results for the number of wave frequency components: error in the integral of the wave elevation power spectral density function.

A.2.2 WEC Simulation Time-Step Convergence

The dynamic WEC model was solved using the Euler method with a fixed time-step. The time-step used in Chapters 2 and 3 is based on results for the mean power captured by the WEC in simulation. The results given in Figure A.4 present an error with respect to the simulation with the smallest time-step. A time-step of 10 ms gives an error less than 1 percent and was chosen for the simulations performed in Chapter 2.

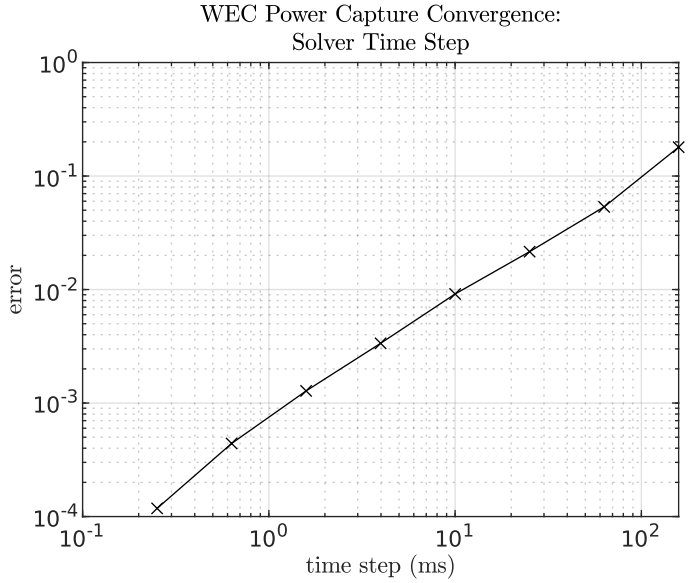

Figure A.4: WEC model solver time-step convergence results: error in mean WEC power capture with respect to the result using the smallest time step (0.1 ms)

A.2.3 WEC Simulation Time-Span Convergence

The length of the WEC simulations performed for the design studies in Chapters 2 and 3 are based on convergence of the mean power captured by the WEC in a given simulation. The results shown in Figure A.5 show a clear trend toward convergence with the results for a simulation length of 2,080 s being 12 percent greater than the result of a 10,000-second simulation. As the design studies presented in this work maintain consistent simulation parameters, 12 percent can be considered adequate. A length of

2000 s was chosen for this work.

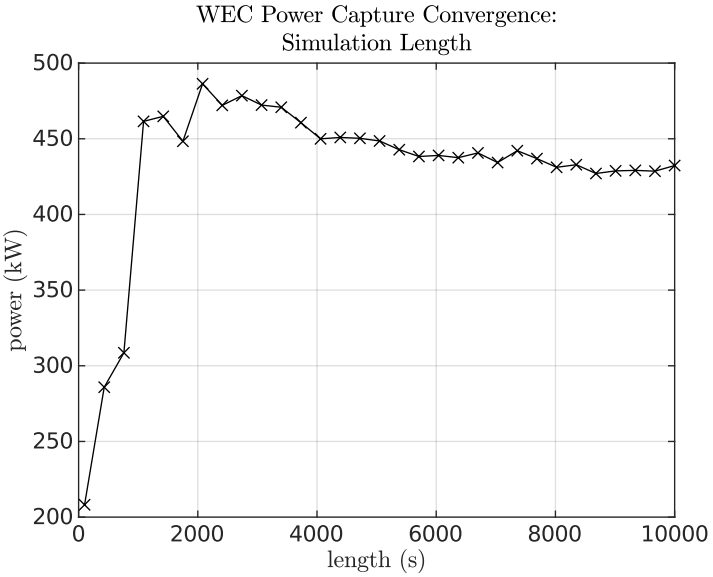

Figure A.5: Convergence results for length of WEC simulations: mean WEC power capture

A.3 Coupled WEC/PTO Model Simulations

Convergence was tested for two sea conditions. These sea conditions were selected from the set of sea states specified for the Wave-to-Water Prize competition [91]. The first, sea state 2, was the sole sea state considered for the study presented in Chapter 4. This sea state has a significant wave height of 2.64 m and a peak period of 9.86 s. The second, sea state 3, is the highest energy sea state of the set selected for the Wave-to-Water Prize competition. This sea state has a significant wave height of 5.36 m and a peak period of 11.52 s. The baseline architecture for the study presented in Chapter 4 was simulated for this convergence study.

A.3.1 WEC/PTO Simulation Time-Step Convergence

The time-step size used for simulations presented in Chapter 4 is based on convergence of an energy balance and volume-based mass balance in the PTO. The energy balance is measured as the difference between power flow at the system boundaries, including power losses, and the energy stored in the system. The volume balance is measured as the difference between the cumulative flow at the system boundaries and the volume stored in the capacitive elements of the system. Results for sea state 2 are presented in Figure A.6. Results for sea state 3 are presented in Figure A.7. The error reported in these figures is the energy balance and volume balance normalized to the energy absorbed by the WEC and the volume of permeate produced by the RO module, respectively. Convergence is obtained for a time step below 0.1 ms for sea state 2 and below 0.05 ms for sea state 3. Therefore, a time-step of 0.05 ms was chosen for the work in Chapter 4.

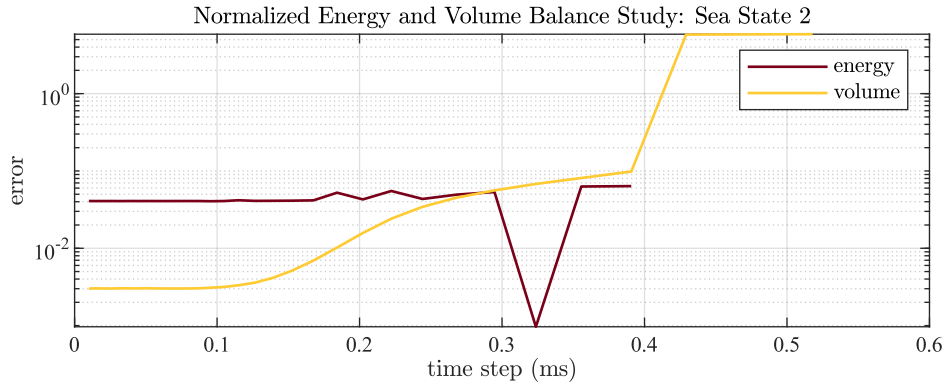

Figure A.6: Time-step convergence results for sea state 2: energy balance error and volume balance error.

A.3.2 WEC/PTO Simulation Time-Span Convergence

The length of time used for simulations presented in Chapter 4 is based on convergence of (1) the power absorbed by the WEC, (2) the permeate produced by the RO module,

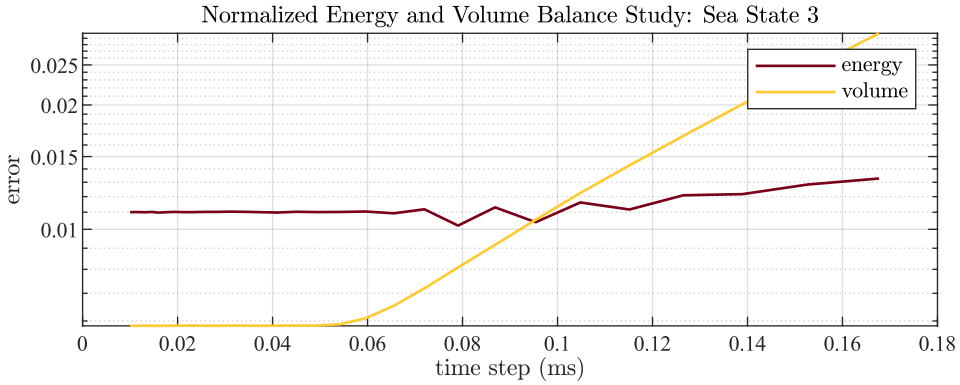

Figure A.7: Time-step convergence results for sea state 3: energy balance error and volume balance error.

and (3) the 99.7th-percentile value for the magnitude of rate-of-change in the RO feed pressure, p_f.

Results for the power absorbed by the WEC are presented in Figures A.8 and A.9. Results for the permeate production are presented in Figures A.10 and A.11. Results for the the rate-of-change in the RO feed pressure are presented in Figures A.12 and A.13. The results for pressure rate-of-change include the peak value and the 97th-percentile. In all cases, these results are normalized to the result for the longest simulation length considered (i.e., 3000 s). Good convergence is reported at 2000 s for all metrics and was chosen for the work presented in Chapter 4

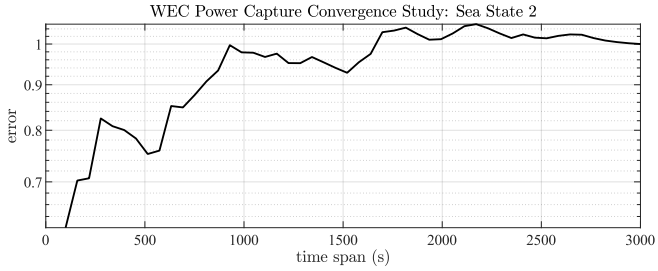

Figure A.8: Convergence results with respect to the length of WEC/PTO simulations for sea state 2: mean WEC power capture

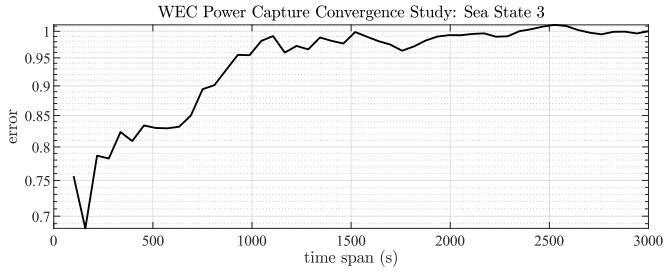

Figure A.9: Convergence results with respect to the length of WEC/PTO simulations for sea state 3: mean WEC power capture

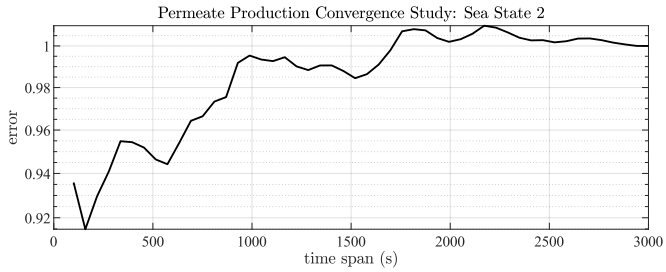

Figure A.10: Convergence results with respect to the length of WEC/PTO simulations for sea state 2: mean permeate production

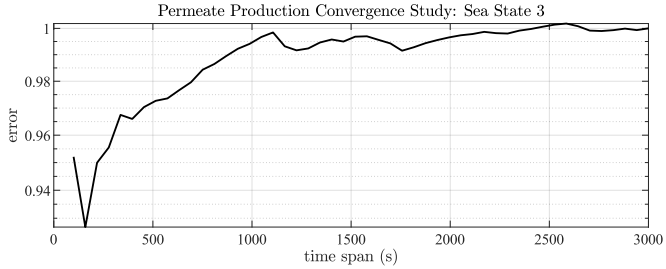

Figure A.11: Convergence results with respect to the length of WEC/PTO simulations for sea state 3: mean permeate production

A.4 Pipeline Model Simulations

This section reports the convergence study results for the simulations performed for the pipeline modeling study presented in Chapter 5. These studies used the same parameters reported in Tables 5.1 and 5.2 unless otherwise noted.

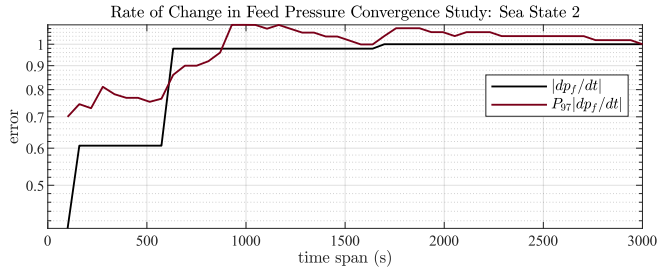

Figure A.12: Convergence results with respect to the length of WEC/PTO simulations for sea state 2: peak rate-of-change in feed pressure

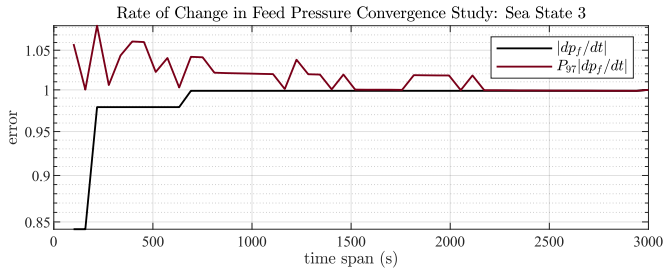

Figure A.13: Convergence results with respect to the length of WEC/PTO simulations for sea state 3: peak rate-of-change in feed pressure

A.4.1 ODE Solver Convergence

The variable time-step ODE solver used is parameterized by an absolute tolerance and relative tolerance for its results. The values were chosen based on convergence of the error between (1) mean power losses calculated by the model and (2) based on pressure and flow rate at the boundaries of the pipelines.

This study was performed using the medium-line model with accumulators having capacitance of $4.2{\cdot}10^{-8}$ m^3/Pa and the pipelines having length of 1200 m and internal diameter of 0.1 m. The peak period was 12 s and the value for X_q was set to 0.01.

Results for the low-pressure pipeline are given in Figure A.14. Results for the high-pressure pipeline are given in Figure A.15. The error is more sensitive to the relative tolerance, likely due to the many orders of magnitude difference between value of flow rate and pressure with the units being in m^3/s and Pa, respectively. The value of 10^{-6}

for both tolerance parameters gave an error less than 0.01 percent and was selected for the study presented in Chapter 5.

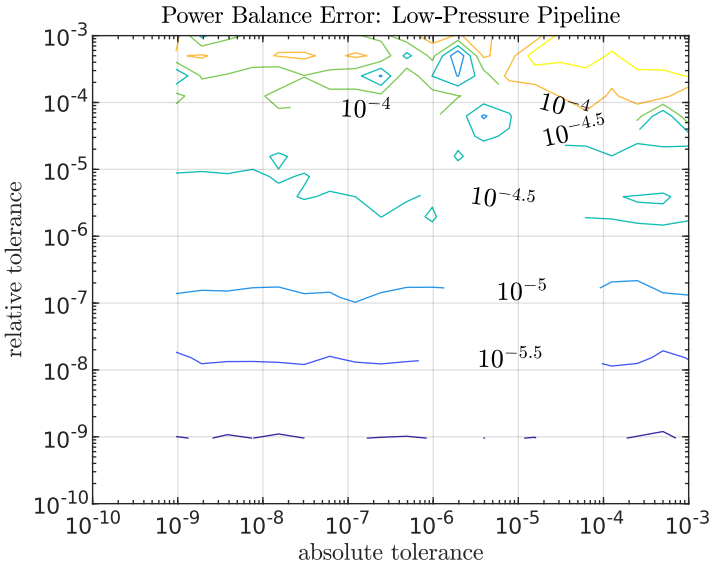

Figure A.14: Variable time step ODE solver tolerance convergence study for power loss in the low-pressure pipeline. Losses calculated by the model and based on boundary conditions are compared.

A.4.2 Method of Characteristics based Pipeline Model Convergence

The number of segments used for the method of characteristics based pipeline models, the fMOC and DGCM, were chosen based on convergence of the mean power loss, a volume balance, and the peak rate-of-change in load pressure (i.e., the outlet of the high-pressure pipeline) resulting from each simulation. Convergence of these metrics was studied for the DGCM model. The volume balance is calculated as the difference between (1) the change in gas volume in the pipeline, between the start and end of the simulation, and (2) the integral of the net flow rate into the pipeline. This metric is normalize by the volume of the pipeline. Convergence studies were performed for the design cases A, G, H, I, and K.

For design case A, the results for the power loss in the low-pressure line are given

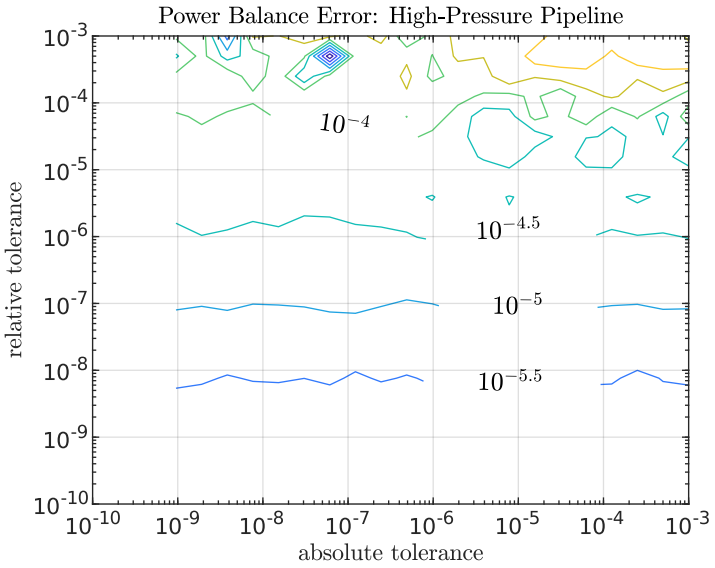

Figure A.15: Variable time step ODE solver tolerance convergence study for power loss in the high-pressure pipeline. Losses calculated by the model and based on boundary conditions are compared.

in Figure A.16, the results for the power loss in the high-pressure line are given in Figure A.17, the results for the volume balance are given in Figure A.18, and the peak rate-of-change in the load pressure is given in Figure A.19. These results show good convergence above 50 segments. This value was used for design cases A, B, C, D, E, F. and J in the work of Chapter 5 because of their similarity in pipeline length and because cases B, C, D, E, F. and J have higher accumulator capacitance than design case A (and therefore lower amplitude excitation of the pipeline).

For design case G, the results for the power loss in the low-pressure line are given in Figure A.20, the results for the power loss in the high-pressure line are given in Figure A.21, the results for the volume balance are given in Figure A.22, and the peak rate-of-change in the load pressure is given in Figure A.23. These results show good convergence above 10 segments. This value was used for design case G in the work of Chapter 5.

For design case H, the results for the power loss in the low-pressure line are given

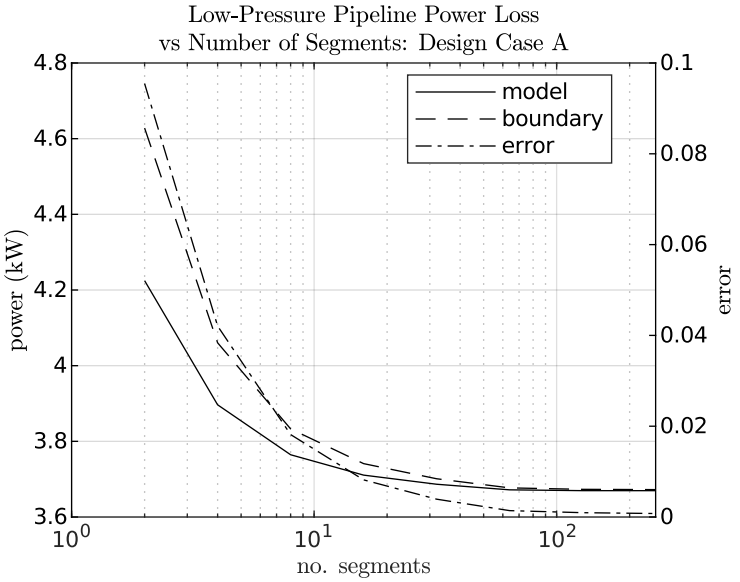

Figure A.16: DGCM convergence for power loss in the low-pressure pipeline with respect to number of segments: design case A. Losses calculated by the model and based on boundary conditions are compared.

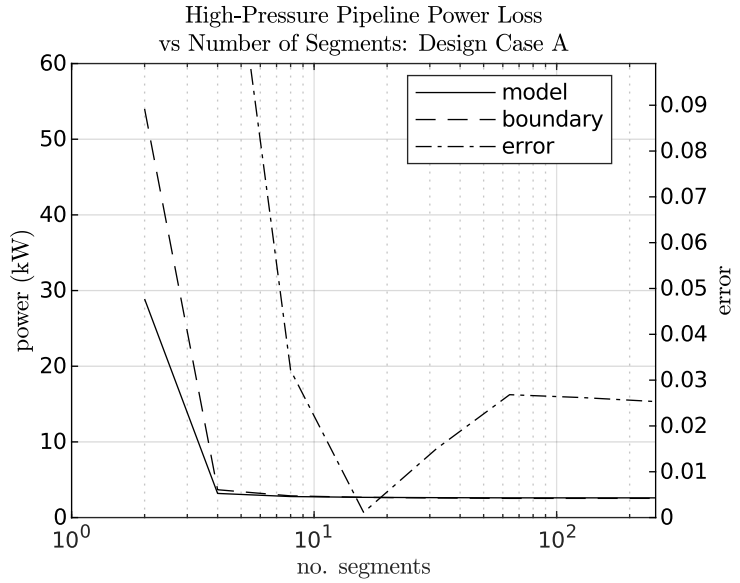

Figure A.17: DGCM convergence for power loss in the high-pressure pipeline with respect to number of segments: design case A. Losses calculated by the model and based on boundary conditions are compared.

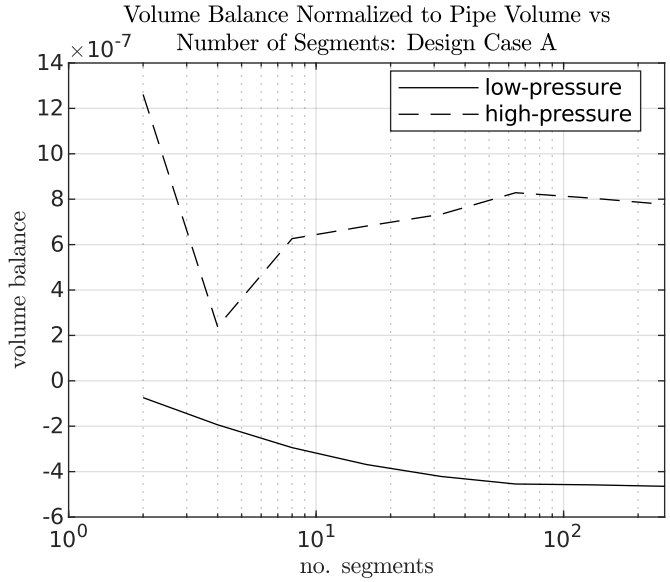

Figure A.18: DGCM convergence in volume (mass) balance with respect to number of segments: design case A. The difference between the change in volume of working fluid in the pipe is compared to the net volume flow into the pipe and is normalized by the pipe volume.

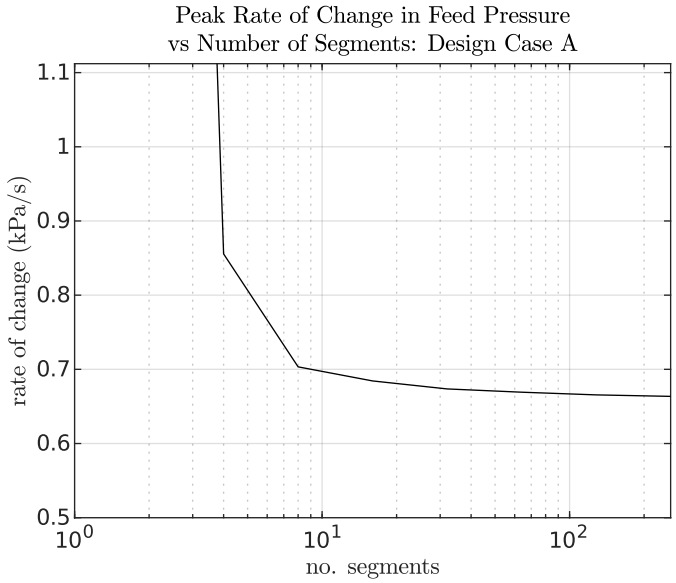

Figure A.19: DGCM convergence for peak rate-of-change in load pressure with respect to number of segments : design case A

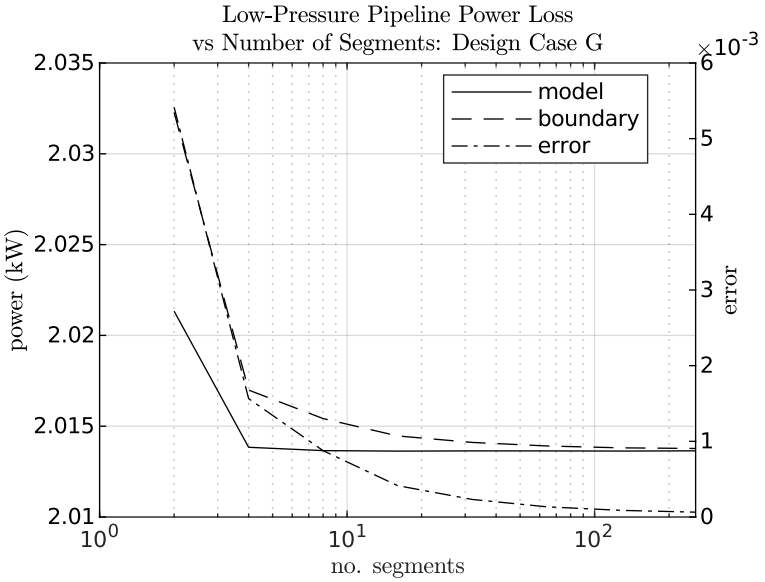

Figure A.20: DGCM convergence for power loss in the low-pressure pipeline with respect to number of segments: design case G. Losses calculated by the model and based on boundary conditions are compared.

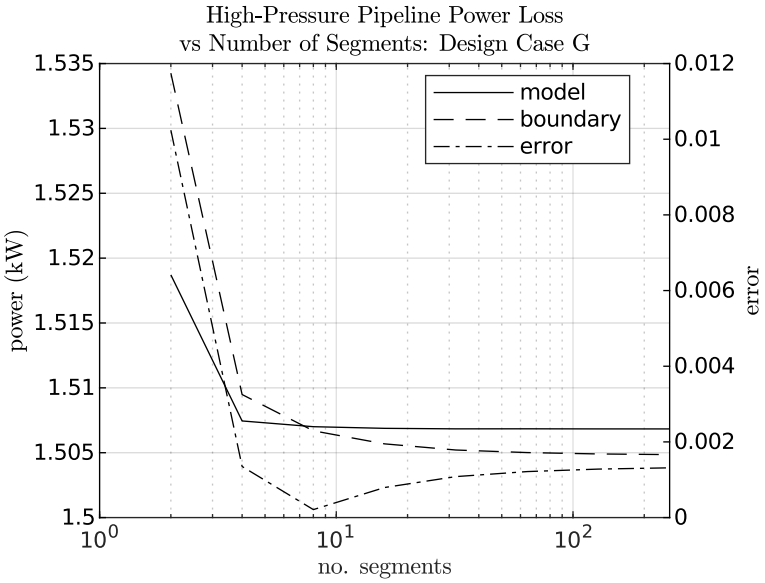

Figure A.21: DGCM convergence for power loss in the high-pressure pipeline with respect to number of segments: design case G. Losses calculated by the model and based on boundary conditions are compared.

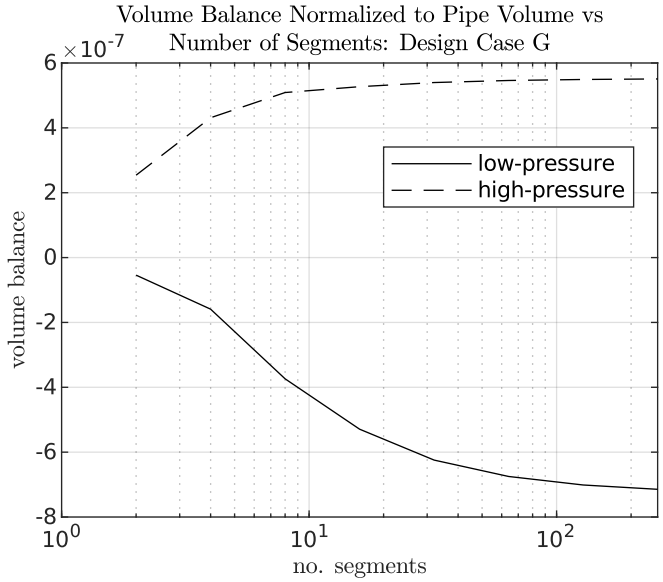

Figure A.22: DGCM convergence in volume (mass) balance with respect to number of segments: design case G. The difference between the change in volume of working fluid in the pipe is compared to the net volume flow into the pipe and is normalized by the pipe volume.

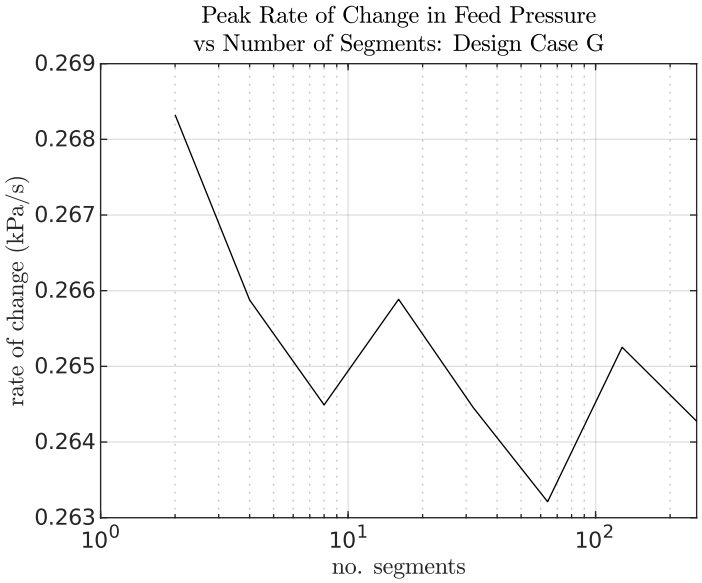

Figure A.23: DGCM convergence for peak rate-of-change in load pressure with respect to number of segments : design case G

in Figure A.24, the results for the power loss in the high-pressure line are given in Figure A.25, the results for the volume balance are given in Figure A.26, and the peak rate-of-change in the load pressure is given in Figure A.27. These results show good convergence above 50 segments. This value was used for design case H in the work of Chapter 5.

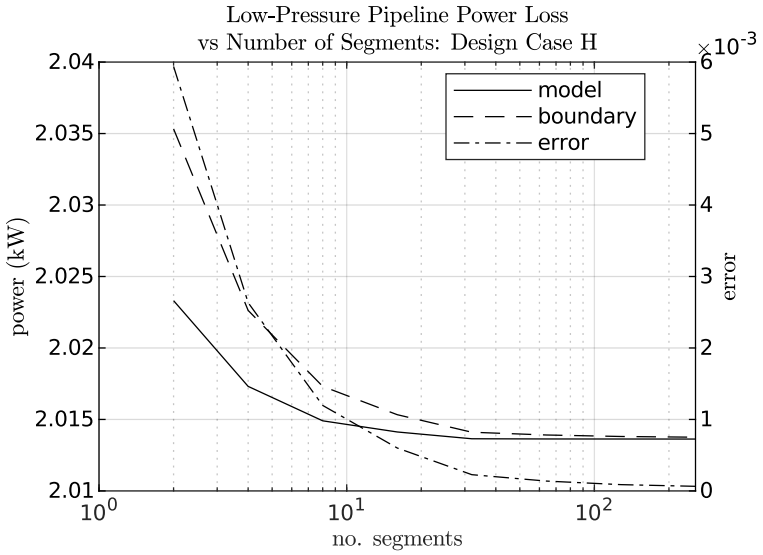

Figure A.24: DGCM convergence for power loss in the low-pressure pipeline with respect to number of segments: design case H. Losses calculated by the model and based on boundary conditions are compared.

For design case I, the results for the power loss in the low-pressure line are given in Figure A.28, the results for the power loss in the high-pressure line are given in Figure A.29, the results for the volume balance are given in Figure A.30, and the peak rate-of-change in the load pressure is given in Figure A.31. These results show good convergence above 10 segments. This value was used for design case I in the work of Chapter 5.

For design case K, the results for the power loss in the low-pressure line are given in Figure A.32, the results for the power loss in the high-pressure line are given in Figure A.33, the results for the volume balance are given in Figure A.34, and the peak

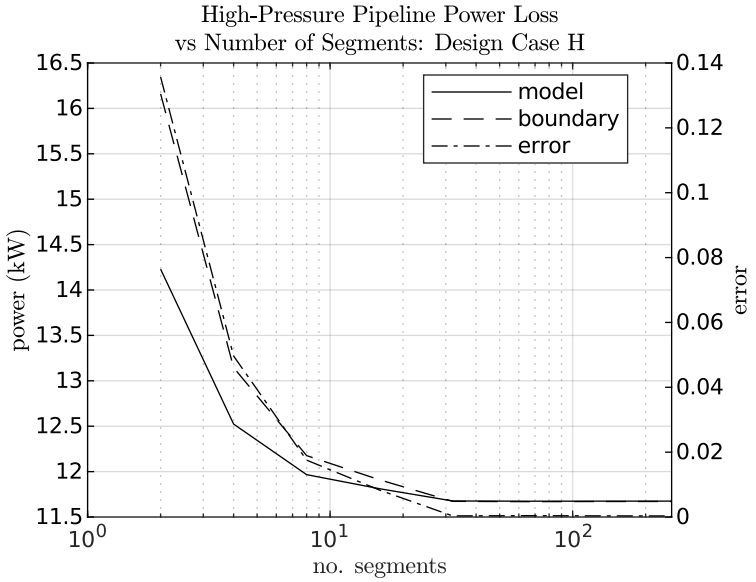

Figure A.25: DGCM convergence for power loss in the high-pressure pipeline with respect to number of segments: design case H. Losses calculated by the model and based on boundary conditions are compared.

rate-of-change in the load pressure is given in Figure A.35. These results show good convergence above 100 segments. This value was used for design case K in the work of Chapter 5.

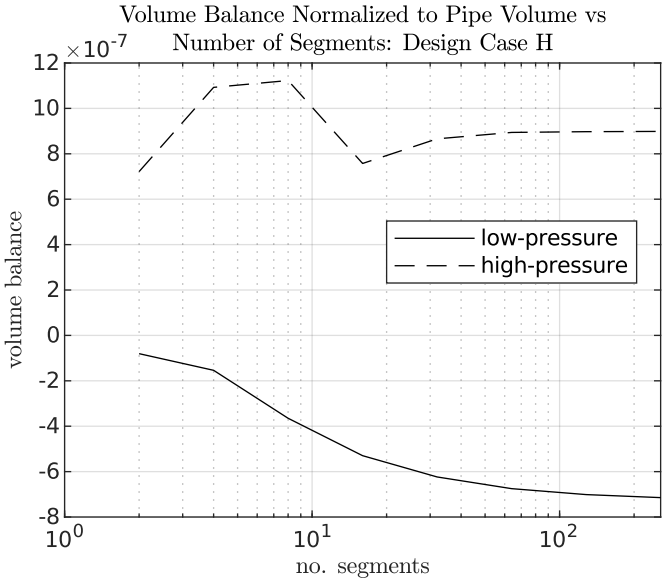

Figure A.26: DGCM convergence in volume (mass) balance with respect to number of segments: design case H. The difference between the change in volume of working fluid in the pipe is compared to the net volume flow into the pipe and is normalized by the pipe volume.

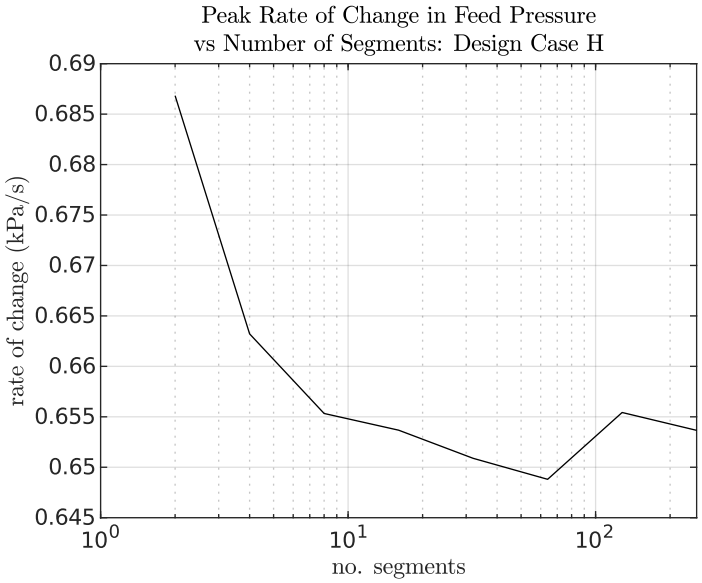

Figure A.27: DGCM convergence for peak rate-of-change in load pressure with respect to number of segments : design case H

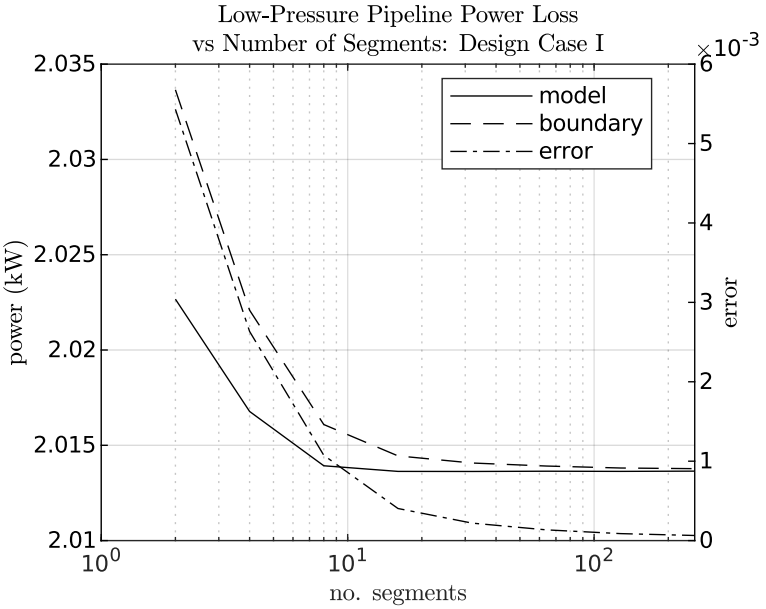

Figure A.28: DGCM convergence for power loss in the low-pressure pipeline with respect to number of segments: design case I. Losses calculated by the model and based on boundary conditions are compared.

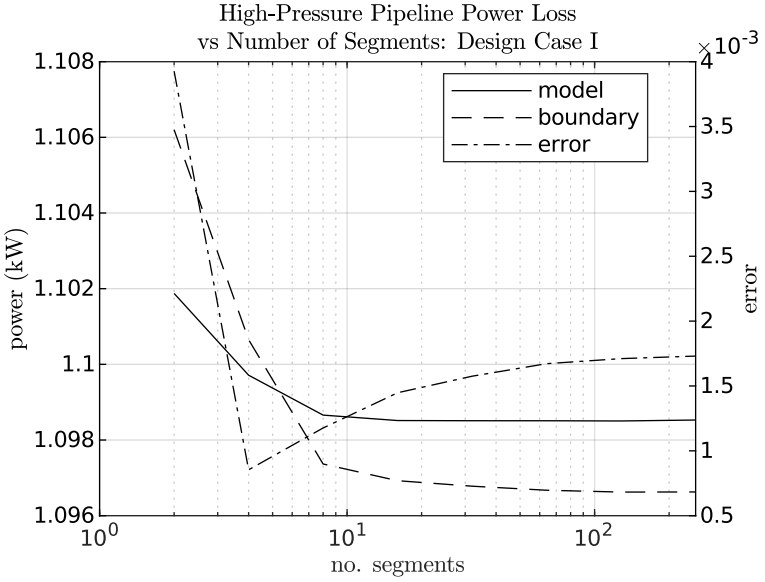

Figure A.29: DGCM convergence for power loss in the high-pressure pipeline with respect to number of segments: design case I. Losses calculated by the model and based on boundary conditions are compared.

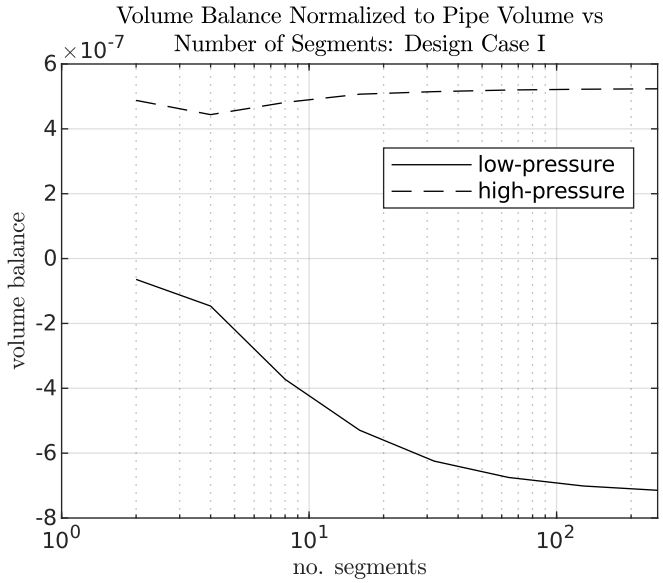

Figure A.30: DGCM convergence in volume (mass) balance with respect to number of segments: design case I. The difference between the change in volume of working fluid in the pipe is compared to the net volume flow into the pipe and is normalized by the pipe volume.

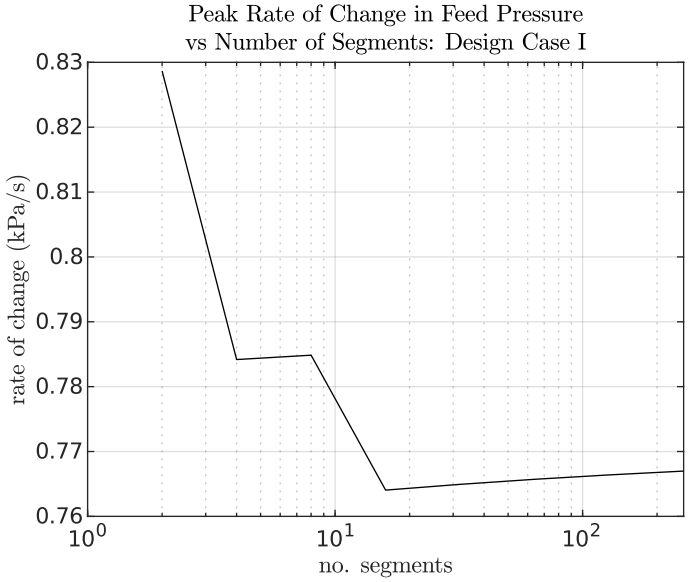

Figure A.31: DGCM convergence for peak rate-of-change in load pressure with respect to number of segments : design case I

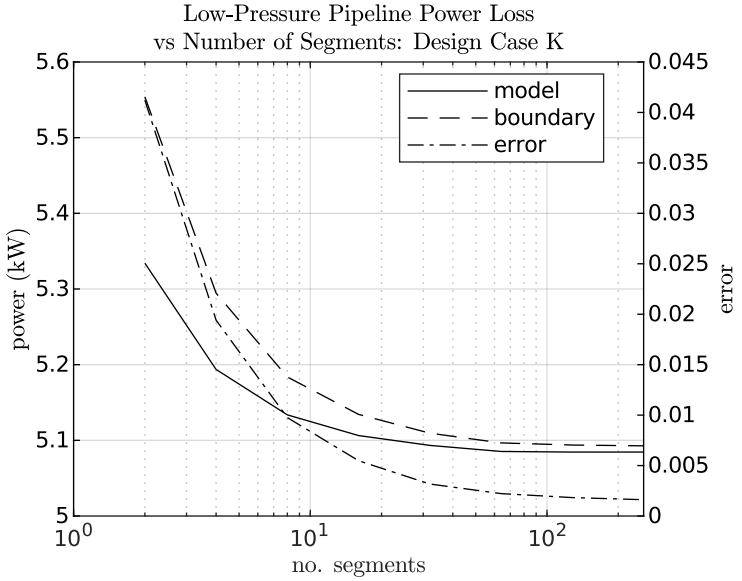

Figure A.32: DGCM convergence for power loss in the low-pressure pipeline with respect to number of segments: design case K. Losses calculated by the model and based on boundary conditions are compared.

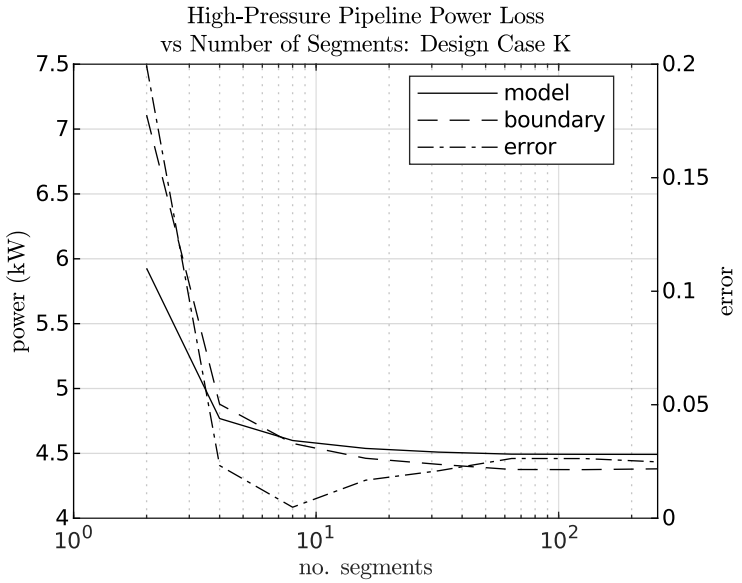

Figure A.33: DGCM convergence for power loss in the high-pressure pipeline with respect to number of segments: design case K. Losses calculated by the model and based on boundary conditions are compared.

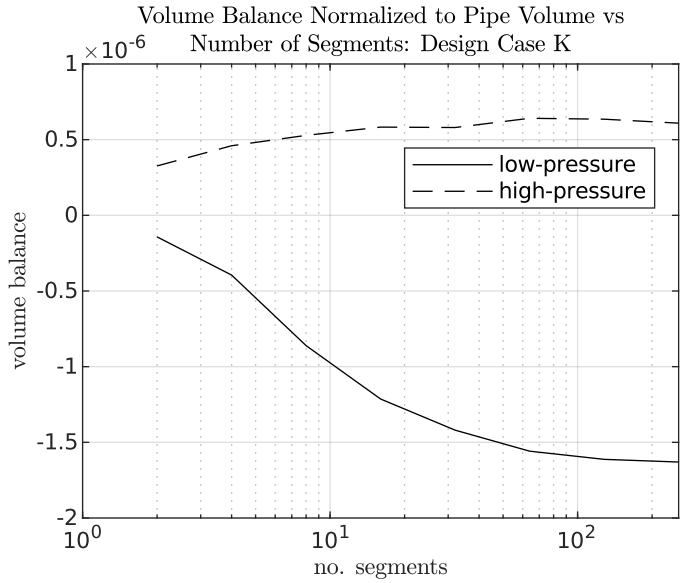

Figure A.34: DGCM convergence in volume (mass) balance with respect to number of segments: design case K. The difference between the change in volume of working fluid in the pipe is compared to the net volume flow into the pipe and is normalized by the pipe volume.

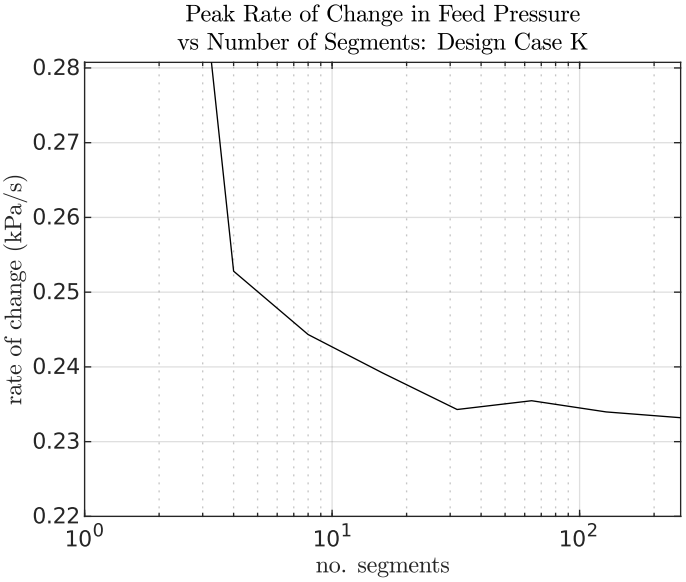

Figure A.35: DGCM convergence for peak rate-of-change in load pressure with respect to number of segments : design case K

Appendix B

Intermediary Results in the Comparison of Power Take-Off Architectures

The content of this appendix was first presented in [60].

B.1 Introduction

This appendix presents intermediary results and discussion from the work of Chapter 2. These results are part of a thorough demonstration of the methods of Chapter 2. Section B.2 presents results for the optimization of the operating parameters for several select PTO designs. Section B.3 presents the entire collection of results for the optimal annual permeate production rate as a function of pump displacement and installed RO membrane area.

B.2 Optimal Operating Parameters

The results presented below are the optimal operating parameters found for several PTO designs operating in a random sample of ten sea conditions. Each table presents the sea conditions, the optimal operating parameters found for each sea condition, and the resulting permeate production rate and its weighted contribution to the yearly average production.

The three parallel-type architectures chosen as examples are the P-FF, P-VF, and P-VV. The results for the selected P-FF design are presented in Tables B.1 and B.2, the P-VF design in Tables B.3 and B.4, and the P-VV design in Tables B.5 and B.6. The PFF example are the results of reference design B. The P-VF and P-VV examples are selected based on the design criterion of Case 1 taking reference design B as the point of reference; that is, their installed membrane area match but they have the smallest pump displacement required to match the annual average permeate production.

Table B.1: Optimal operating parameters example for a parallel-type PTO with fixed displacement and fixed active RO membrane area (P-FF)

Sea condition		Operating parameters
Significant wave height (m)	Peak period (s)	RO feed pressure (MPa)
0.75	9.9	-
0.75	12.2	-
1.25	5.2	-
1.75	14.5	5.1
2.25	8.7	-
2.25	19.1	5.4
3.25	13.3	7.4
3.25	14.5	7.4
4.25	11	8.0
4.75	16.8	8.0

Note: Results are given for a randomly selected subset of sea conditions presented in Figure 2.6. This example design has a 0.230 m^3/rad pump displacement and 3700 m^2 total installed membrane area. The annual average permeate production for this design is 1518 m^3/day. This is reference design B.

Table B.2: Optimal performance example for a parallel-type PTO with fixed displacement and fixed active RO membrane area (P-FF)

Sea condition		Permeate production (m^3/day)		Power (kW)		
Significant wave height (m)	Peak period (s)	unweighted	weighted	Captured by WEC	Consumed by charge pump	Produced by generator
0.75	9.9	0	0	-	-	-
0.75	12.2	0	0	-	-	-
1.25	5.2	0	0	-	-	-
1.75	14.5	2283	17.35	208.5	50.3	50.3
2.25	8.7	0	0	-	-	-
2.25	19.1	2539	0.508	242.2	56.0	56.0
3.25	13.3	4224	59.98	514.3	93.1	93.1
3.25	14.5	4199	33.17	509.7	92.6	92.6
4.25	11	4704	9.88	610.4	103.7	105.4
4.75	16.8	4704	3.29	639.5	103.7	126.6

Note: See note for Table B.1.

For the P-FF design, it is shown that system cannot satisfy the design constraints for operation in four out of the ten sea conditions; including the sea conditions not shown, the design fails to operate in 29 out of 114 sea conditions. As a general trend the RO feed pressure is lower in cases where less power is available for production of permeate. In the two highest power sea conditions shown, the RO feed pressure is set to the upper limit and the excess power is converted to electricity (comparing the power consumed by the charge pump and the power generated by the generator).

The P-VF design has practically identical results to reference design B, including failure to operate in the same sea conditions, despite the added degree of freedom offered by the variable displacement of the WEC-driven pump. For this combination of pump displacement, membrane area, and selection of sea conditions, there appears to be no advantage in having a variable-displacement pump. The only sea condition shown where the pump displacement is decreased is the highest power condition where there is an

Table B.3: Optimal operating parameters example for a parallel-type PTO with variable displacement and fixed active RO membrane area (P-VF)

Sea condition		Operating parameters	
Significant wave height (m)	Peak period (s)	WEC-driven pump displacement (m^3/rad)	RO feed pressure (MPa)
0.75	9.9	-	-
0.75	12.2	-	-
1.25	5.2	-	-
1.75	14.5	0.230	5.1
2.25	8.7	-	-
2.25	19.1	0.230	5.4
3.25	13.3	0.230	7.4
3.25	14.5	0.230	7.4
4.25	11	0.230	8.0
4.75	16.8	0.216	8.0

Note: Results are given for a randomly selected subset of sea conditions presented in Figure 2.6. This example design has a 0.230 m^3/rad pump displacement and 3700 m^2 total installed membrane area. The annual average permeate production for this design is 1518 m^3/day.

excess of power available.

In contrast, the P-VV architecture achieves operation in all 114 sea conditions. The overall design performance is better because the annual average permeate production and installed membrane match while the P-VV design has a pump displacement that is 25 percent lower. Permeate production rates for this P-VV design in Table B.5 are generally lower compared to the P-FF results in Table 8 but this is made up for with the greater number of sea conditions the P-VV design can operate in. As with the P-VF design, this design makes little use of the variable pump displacement, with it only varying in 4 of 114 sea conditions. However, the design does make use of the variable RO membrane area, with this being lowered in all but one of the ten selected sea conditions and all but eleven out of the entire set of 114 sea conditions. Figure B.1 shows the distribution of the specified active membrane area for all 114 sea conditions. The distribution of the variable membrane area is essentially bi-modal with median

Table B.4: Optimal performance example for a parallel-type PTO with variable displacement and fixed active RO membrane area (P-VF)

Sea condition		Permeate production (m^3/day)		Power (kW)		
Significant wave height (m)	Peak period (s)	unweighted	weighted	Captured by WEC	Consumed by charge pump	Produced by generator
0.75	9.9	0	0	-	-	-
0.75	12.2	0	0	-	-	-
1.25	5.2	0	0	-	-	-
1.75	14.5	2283	17.35	208.5	50.3	50.3
2.25	8.7	0	0	-	-	-
2.25	19.1	2539	0.508	242.2	56.0	56.0
3.25	13.3	4224	59.98	514.3	93.1	93.1
3.25	14.5	4199	33.17	509.7	92.6	92.6
4.25	11	4704	9.88	610.4	103.7	105.4
4.75	16.8	4704	3.29	608.2	103.7	103.8

Note: See note for Table B.3.

values of about 700 square meters in the lesser mode and 3200 square meters for the greater mode.

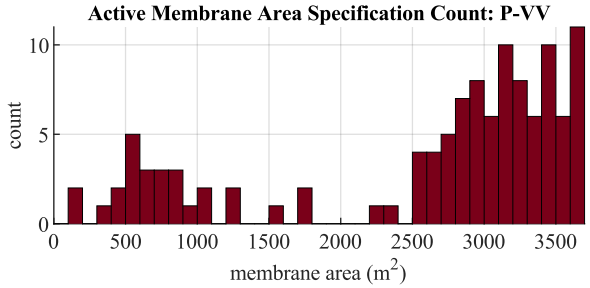

Figure B.1: Histogram of active RO membrane specified for each sea condition for the parallel-type PTO with variable displacement and variable active RO membrane area (P-VV) having a 0.172 cubic meter per radian pump displacement and 3700 square meters of total installed membrane area.

The second set of examples are for series-type architectures. The first is for the S-VV architecture, given in Tables B.7 and B.8. The second is the M-FV architecture

Table B.5: Optimal operating parameters for a parallel-type PTO with variable displacement and variable active RO membrane area (P-VV)

Sea condition		Operating parameters		
Significant wave height (m)	Peak period (s)	WEC-driven pump displacement (m^3/rad)	Active RO membrane area (m^2)	RO feed pressure (MPa)
0.75	9.9	-	629	-
0.75	12.2	-		-
1.25	5.2	-	518	-
1.75	14.5	0.172	3700	4.8
2.25	8.7	-	888	-
2.25	19.1	0.172	3552	5.0
3.25	13.3	0.172	2886	7.6
3.25	14.5	0.172	2738	7.9
4.25	11	0.172	2997	8.0
4.75	16.8	0.172	3071	8.0

Note: Results are given for a randomly selected subset of sea conditions presented in Figure 2.6. This example design has a 0.172 m^3/rad pump displacement and 3700 m^2 total installed membrane area. The annual average permeate production for this design is 1518 m^3/day.

given in Tables B.9 and B.10. These selected designs are also derived using the criterion of Case 1 with reference design B as the point of reference.

Like the P-VV example design, both series-type PTO examples appear to be more flexible to changing sea conditions than the baseline design. Like the P-VV example, they succeed in operating in all sea conditions and make use of the variable membranes area. However, these examples make less use of the variable membrane area with the S-VV using all membrane area in 81 out of 114 sea conditions and the M-FV using all membrane area in 83 out of 114 sea conditions. As with the P-VV example, the S-VV example only varies the pump displacement in four out of 114 sea conditions.

For the M-FV example, the pressure at the WEC driven pump is essentially maximized at the imposed limit of 30 MPa in all but ten sea conditions (one is shown in Table B.9). The switching duty for the M-FV example is varied between 0.22 to 0.50 which is a reasonable range for switch-mode systems.

Table B.6: Optimal performance example for a parallel-type PTO with variable displacement and variable active RO membrane area (P-VV)

Sea condition		Permeate production (m^3/day)		Power (kW)		
Significant wave height (m)	Peak period (s)	unweighted	weighted	Captured by WEC	Consumed by charge pump	Produced by generator
0.75	9.9	248	4.73	-	-	-
0.75	12.2	337	1.79	-	-	-
1.25	5.2	286	0.0286	-	-	-
1.75	14.5	2045	15.54	179.2	45.1	45.1
2.25	8.7	969	50.85	-	-	-
2.25	19.1	2172	0.434	197.7	47.9	47.9
3.25	13.3	3438	48.83	428.6	75.8	75.8
3.25	14.5	3405	26.90	434.8	75.1	75.1
4.25	11	3797	7.97	489.9	83.7	83.7
4.75	16.8	3878	2.71	499.3	85.5	85.5

Note: See note for Table B.5.

B.3 Objective Space

This subsection presents all data obtained by the design study for the performance of each architecture with respect to the three primary design objectives: maximizing permeate production, minimizing pump displacement, and minimizing the total installed membrane area. The design study produces a surface that can be presented on contour plots for the yearly average permeate production as a function of the maximum pump displacement and total installed membrane area with each data point being based on optimal operating conditions in each sea condition.

Along with these data, contour-level curves and markers are included to provide a visual comparison to the reference designs specified in Table 2.5. The contour plots presented below include contour-level curves for permeate production matching the performance of the two reference designs and markers at the pump displacement and total installed membrane area for those reference designs. A notable use for these visual aids

Table B.7: Optimal operating parameters example for a series-type PTO with variable displacement and variable active RO membrane area (S-VV)

Sea condition		Operating parameters		
Significant wave height (m)	Peak period (s)	WEC-driven pump displacement (m^3/rad)	Active RO membrane area (m^2)	RO feed pressure (MPa)
0.75	9.9	0.117	666	6.4
0.75	12.2	0.117	888	6.4
1.25	5.2	0.117	777	6.4
1.75	14.5	0.117	3700	7.2
2.25	8.7	0.117	2516	6.4
2.25	19.1	0.117	3700	7.3
3.25	13.3	0.117	3700	8.6
3.25	14.5	0.117	3700	8.5
4.25	11	0.117	3700	8.9
4.75	16.8	0.117	3700	8.9

Note: Results are given for a randomly selected subset of sea conditions presented in Figure 2.6. This example design has a 0.117 m^3/rad pump displacement and 3700 m^2 total installed membrane area. The annual average permeate production for this design is 1518 m^3/day.

is in determining whether a PTO architecture can surpass the design performance of the reference design. When the reference contour-level for a given architecture crosses through points with lower pump displacement and total installed membrane area than the corresponding marker, it is possible for that architecture to outperform the reference design with respect to all three design objectives simultaneously. In other words, choosing this architecture over the reference design would be a strong Pareto improvement [1] to the system design. Note however that this is not a mandatory condition for showing a strong Pareto improvement over a reference design.

The data are grouped by the type of architecture (i.e., parallel-type, series-type, and series-type with a switch-mode power transformer). The parallel and series-type groups include each combination of fixed and variable pump displacement and active membrane

[1] Applied to multi-objective machine design, a "Pareto improvement" is a design change that improves on at least one design objective while not degrading performance on the other objectives. A "strong Pareto improvement" is a design change that improves on all design objectives simultaneously.

Table B.8: Optimal performance example for a series-type PTO with variable displacement and variable active RO membrane area (S-VV)

Sea condition		Permeate production (m^3/day)		Power (kW)		
Significant wave height (m)	Peak period (s)	unweighted	weighted	Captured by WEC	Consumed by charge pump	Produced by generator
0.75	9.9	260	4.97	20.4	5.7	5.7
0.75	12.2	343	1.82	26.8	7.6	7.6
1.25	5.2	303	0.0303	23.7	6.7	6.7
1.75	14.5	2078	15.79	183.2	45.8	45.8
2.25	8.7	972	51.01	75.8	21.4	21.4
2.25	19.1	2202	0.440	198.4	48.5	48.5
3.25	13.3	3248	46.12	345.9	71.6	71.6
3.25	14.5	3210	25.36	339.9	70.8	70.8
4.25	11	3519	7.39	389.6	77.6	77.6
4.75	16.8	3539	2.48	393.0	78.0	78.0

Note: See note for Table B.7.

area. The data for the parallel-type architectures are given in Figure B.2. The data for the series-type architectures are given in Figure B.3. The group with the switch-mode power transformer includes the option of a fixed and variable active membrane area with each having a fixed displacement pump; results for these architectures are given in Figure B.4. Note that roughness of the contour curves in these figures are a result of having a discrete set of sea conditions with designs being able to operate in some subset of sea conditions at one point and a different subset of conditions at adjacent points.

The results for the parallel-type architectures, shown in Figure B.2, suggest an advantage in having a variable active membrane area but no significant advantage in using a variable displacement pump. The contours for the for P-VF design follow similar paths as the P-FF design and both peak between 2000 and 2500 m^3/day. However, the P-FV and P-VV designs peak between 3000 and 3500 m^3/day within the range of designs displayed. The general trend between the P-FF and P-VF plots is that the surface is

Table B.9: Optimal operating parameters example for a series-type PTO with a switch-mode power transformer, fixed displacement, and variable Active RO membrane area (M-FV)

Sea condition		Operating parameters		
Significant wave height (m)	Peak period (s)	duty	Active RO membrane area (m^2)	RO feed pressure (MPa)
0.75	9.9	0.23	666	30.0
0.75	12.2	0.28	814	23.8
1.25	5.2	0.23	851	30.0
1.75	14.5	0.26	3700	30.0
2.25	8.7	0.23	2997	30.0
2.25	19.1	0.26	3700	30.0
3.25	13.3	0.30	3700	30.0
3.25	14.5	0.30	3700	30.0
4.25	11	0.31	3700	30.0
4.75	16.8	0.31	3700	30.0

Note: Results are given for a randomly selected subset of sea conditions presented in Figure 2.6. This example design has a 0.0327 m^3/rad pump displacement and 3700 sm^2 total installed membrane area. The annual average permeate production for this design is 1518 m^3/day.

projected in the direction of increasing pump size without the height of the surface being affected much at the lower displacements. The P-FV plot is similar but continues to increase in height as the membrane area increases.

The result for the series-type architectures, shown in Figure B.3, show similar trends to the parallel-type architectures. The most significant difference between the series and parallel-type architectures is that the peak of the surface is shifted to lower pump displacements. Otherwise, the same type of surface projection occurs between cases of fixed versus variable conditions for the pump displacement and active membrane area. The peaks of each surface are again between 2000 and 2500 m^3/day for the architectures with fixed active RO membrane areas and between 3000 and 3500 m^3/day with variable active membrane areas. An interesting observation with respect to the reference contour and marker for reference design A is that the pump displacement of reference design A

Table B.10: Optimal performance example for a series-type PTO with a switch-mode power transformer, fixed displacement, and variable Active RO membrane area (M-FV)

Sea condition		Permeate production (m^3/day)		Power (kW)		
Significant wave height (m)	Peak period (s)	unweighted	weighted	Captured by WEC	Consumed by charge pump	Produced by generator
0.75	9.9	261	4.99	22.7	5.8	5.8
0.75	12.2	314	1.66	27.0	6.9	6.9
1.25	5.2	334	0.0334	29.1	7.4	7.4
1.75	14.5	2056	15.62	201.2	45.3	45.3
2.25	8.7	1150	60.35	99.4	25.3	25.3
2.25	19.1	2208	0.442	222.0	48.7	48.7
3.25	13.3	3040	43.16	350.1	67.0	67.0
3.25	14.5	3013	23.81	345.7	66.4	66.4
4.25	11	3222	6.77	381.4	71.0	71.0
4.75	16.8	3233	2.26	383.2	71.3	71.3

Note: See note for Table B.9.

is beyond the peak in the surface and in a region where increasing the pump size harms the performance of the design.

The results for the architecture with a switch-mode power transformer, shown in Figure B.4, are also similar to the other types of architectures but with peaks shifted to even lower pump displacements. Additionally, the same observation made of the series-type architectures and the pump displacement of the reference design can be made for the switch-mode architectures, in that the pump displacement used by the reference design is in a region where increasing it will harm the performance of the design.

A final observation from these data is that each architecture is shown to be a strong Pareto improvement over the reference designs. The degree to which this is true will be analyzed in the next sub-section with the direct comparisons based on the three design cases outlined in the beginning of Section 2.3.

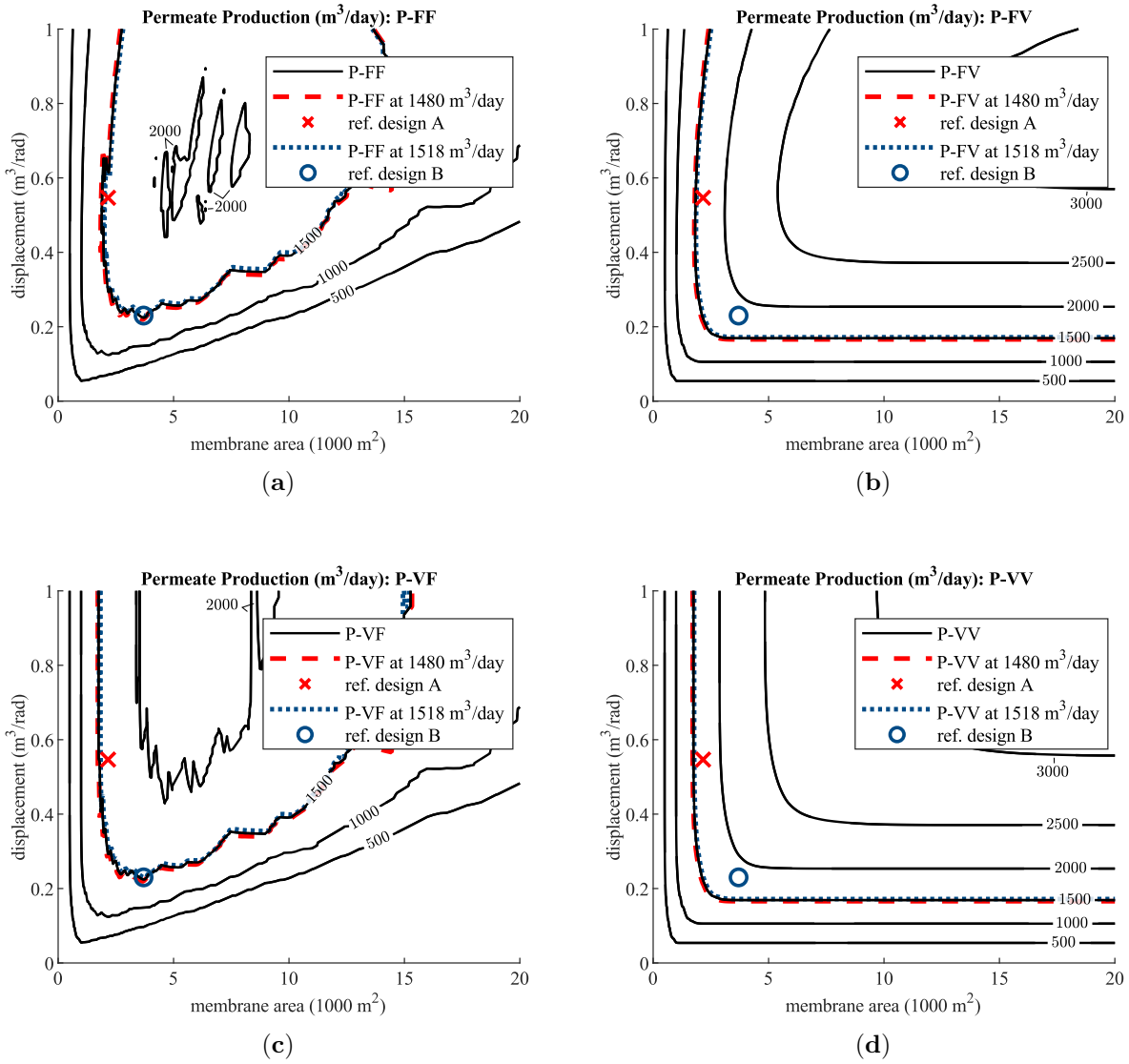

Figure B.2: Annual average permeate production as a function of WEC-driven pump displacement and installed RO membrane area for parallel-type PTO architectures having a WEC-driven pump with fixed displacement (P-FF and P-FV, a and b) or variable displacement (P-VF and P-VV, c and d) and an RO module with an active membrane area that is fixed (P-FF and P-VF, a and c) or variable (P-FV and P-VV, b and d).

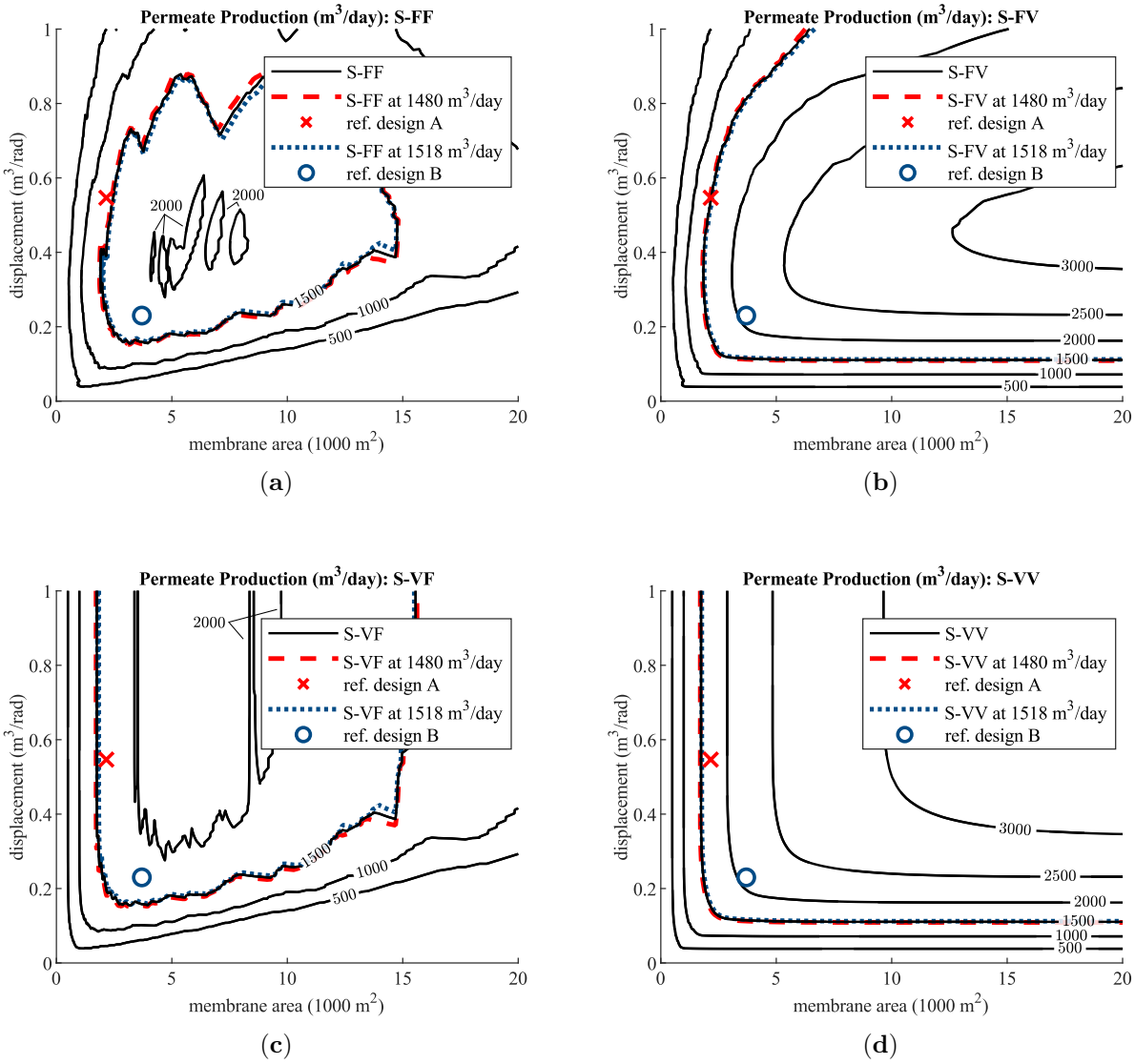

Figure B.3: Annual average permeate production as a function of WEC-driven pump displacement and installed RO membrane area for series-type PTO architectures having a WEC-driven pump with fixed displacement (S-FF and S-FV, a and b) or variable displacement (S-VF and S-VV, c and d) and an RO module with an active membrane area that is fixed (S-FF and S-VF, a and c) or variable (S-FV and S-VV, b and d).

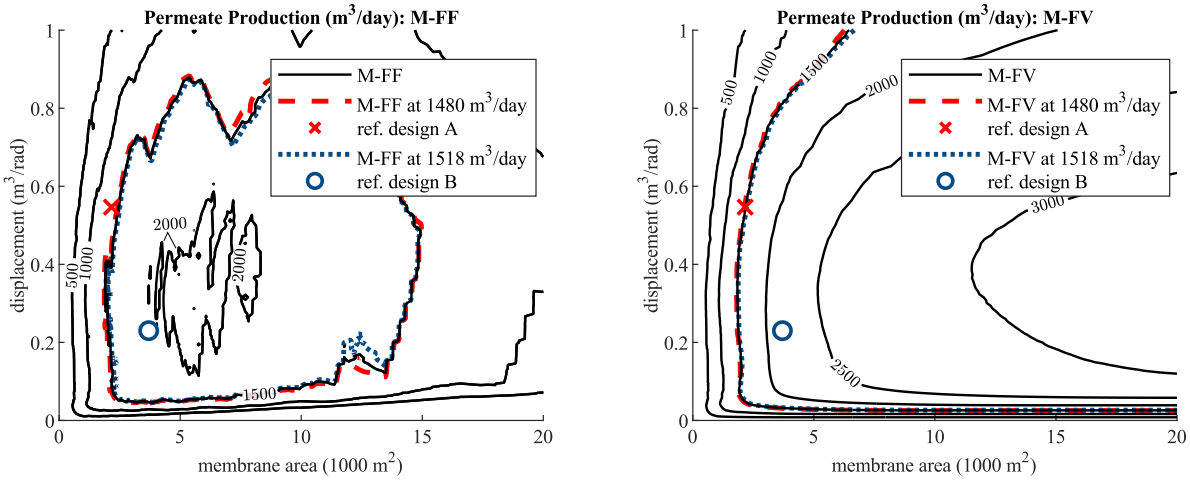

(**a**) (**b**)

Figure B.4: Annual average permeate production as a function of WEC-driven pump displacement and installed RO membrane area for series-type PTO architectures with a switch-mode power transformer having an RO module with an active membrane area that is fixed (M-FF, a) or variable (M-FV, b).

Appendix C

Component Sizing

This appendix presents design studies related to components sizing not explored in Chapter 4 and details about the modeling of components in the low-pressure branch of the hydraulic circuit. Section C.1 presents a grid study used to select the size of the check valves in the WEC-driven pump. Section C.2 presents a grid study used to select the size of the hydraulic motor for the parallel-type PTO architectures. Section C.3 presents details about how the low-pressure accumulator and charge pump were modeled for the study presented in Chapter 4 and presents a design study showing the potential design performance of the system in terms of the volume of the low-pressure accumulator and the power losses of the charge pump.

Parameters specific to each design study presented below are specified. Otherwise, all other parameters of the simulations were identical to simulations performed for the study in Chapter 4.

C.1 WEC-Driven Pump Check Valve Sizing

The sizes of the check valves in the WEC-driven pump were chosen considering the efficiency of the WEC-driven pump and the minimum pressure in the pumping chamber. A grid study was performed varying the flow coefficient of the check valves. The flow

coefficient of the low-pressure, inlet check valve was set at 1.5 times larger than the high-pressure, outlet check valve. The low-pressure accumulator volume was set to 4000 liters and the charge pump speed was set to 2500 rpm. The system was simulated for 500 seconds with a time-step of 1 us. The results of this study are presented in Figure C.1.

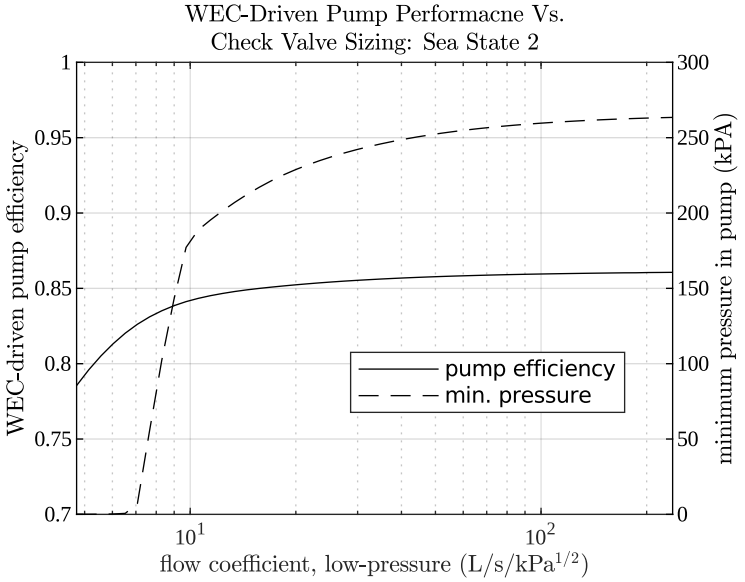

Figure C.1: Check valve sizing study results: minimum pressure and efficiency of the WEC-driven pump vs. flow coefficient of the low-pressure check valve. The high pressure check valve has a flow coefficient that is 1.5 times smaller.

The results in Figure C.1 show an increase in the the efficiency and minimum pressure as the flow coefficient is increases. These reach asymtotes of about 0.86 and 270 kPa respectively and are a results of the cracking pressure setting a minimum pressure drop. The values 10 and 15 L/s/KPa$^{1/2}$ are chosen which give an efficiency of 0.85 and a minimum pressure at a point of diminishing returns.

C.2 Hydraulic Motor Sizing

The size of the hydraulic motor was selected with consideration of (1) the regulation of RO feed pressure (mean, minimum, maximum, and standard deviation), (2) the peak

rate-of-change in the RO feed pressure, (3) the mean electrical power generated, (4) the power losses from the hydraulic motor, generator, and pressure relief valves, and (5) the permeate production rate. A grid study varying the hydraulic motor displacement was performed for the parallel-type PTO architecture with an added passive resistive element and high-pressure accumulator. The total accumulator volume was set to 10,000 liters with an equal distribution between the two high-pressure accumulators. The flow coefficient of the resistive element was set at 4.7 L/s/kPa$^{1/2}$. Figure C.2 presents the results of this study.

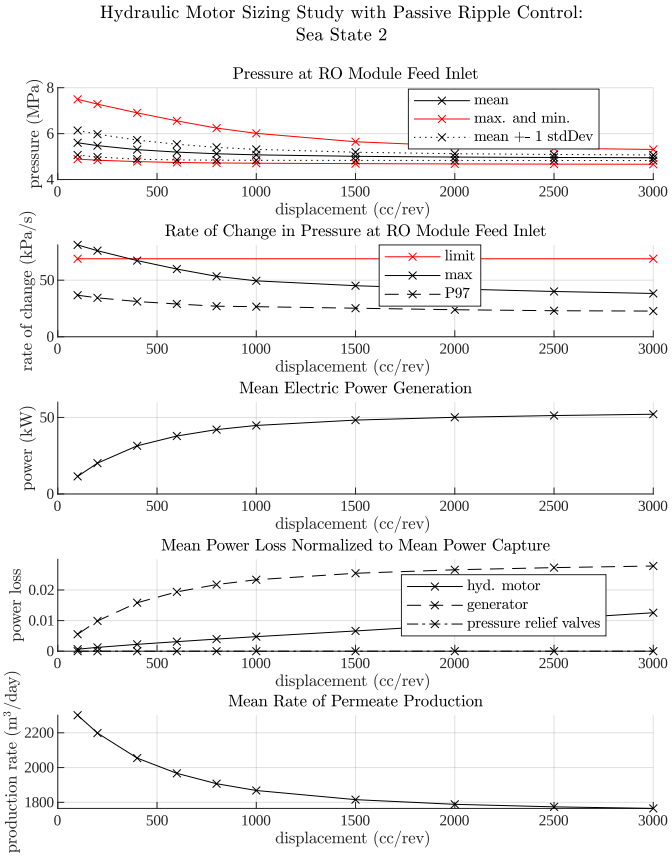

Figure C.2: Hydraulic motor sizing study results

The results in Figure C.2 show an adverse affect to pressure regulation and the peak rate-of-change in feed pressure for motor lower displacements. This is explained by the saturation of the flow through the motor at its maximum speed preventing it from keeping up with the mean flow supplied by the WEC-driven pump. There is also a trade-off between electrical power production and permeate production at the low displacements due to the higher mean pressure at the RO feed inlet leading to higher rates of permeate flow and to lower rates of flow available for electric power generation. Each metric levels off at higher displacement except for the power losses from the hydraulic motor. This is explained by the hydraulic motor operating at a lower mean shaft speed, where its overall efficiency is lower.

Overall, there is a trade-off between (1) power losses from the hydraulic motor and higher cost of of a larger machine and (2) pressure regulation performance. From these results, 1000 cc/rev was chosen as the hydraulic motor displacement for the parallel-type PTO architecture in Chapter 4.

C.3 Low-Pressure Branch Design

A model of the charge pump and the behavior of the low-pressure branch is not reported in Chapter 4 because this part of the system did not influence the results of the study presented there. However, these were modeled and do impact the performance of the system through the pressure differentials across the WEC-driven pump, ERU, and, for parallel-type PTO architectures, the hydraulic motor that drives the generator. This section describes the models used and presents a design study that informs the sizing of the low-pressure accumulators and operating speed of the charge pump.

The low-pressure accumulator was modeled the same as the high-pressure accumulators. The charge pressure for the low-pressure accumulator was set to 150 kPa.

The flow through the charge pump was modeled by a parabolic pump curve

$$q_c = \sqrt{\frac{p_l - p_o - c_n\omega^2}{c_q}} \tag{C.1}$$

following the nomenclature of Chapter 4 and where c_n and c_q are coefficients of the model. The flow is zero when the pressure differential exceeds the shut-off pressure $c_n\omega^2$. The coefficient value assumed for c_n was 5.5 Pa·s^2/rad^2. The coefficient value assumed for c_q was -5·10^6 (m^3/s)^2/Pa.

For the study performed in Chapter 4, the low-pressure accumulator volume was assumed to be 10,000 liters and the charge pump was operated at 2500 rpm.

Improved design performance (i.e. reduced volume and power loss) could be gained by selecting the low-pressure accumulator volume and the speed of the charge pump based on the power loss of the charge pump and electric motor driving it, and the minimum pressure seen in the pumping chamber of the WEC-driven pump. A grid study considering these variable is presented here to demonstrate the performance potential of the system. A Pareto front was found which takes the design objective as minimizing the accumulator volume and minimizing the power loss. A constraint for the minimum pressure in the WEC-driven pump was set at 50 kPa. The accumulator volume was varied on a base-10 log scale between 100 L and 5000 L with 20 values. The charge pump speed was varied from 1700 rpm to 3000 rpm in increments of 100 rpm. Losses of the charge pump and the electric motor driving it were based on a constant efficiency. The charge pump was assumed to have an efficiency of 0.7. The electric motor was assumed to have an efficiency of 0.9.

Result of this study are given in Figure C.3. This figure presents (1) the Pareto front for power loss and volume, (2) the minimum pressure in the WEC-driven pump throughout the simulation, (3) the charge pump speed determined to be optimal for each accumulator volume, and (4) a description of the pressure variation in the low-pressure accumulator at the WEC-driven pump inlet. Based on these results, the values chosen

for the study presented in Chapter 4 are conservative as evidenced by the optimal charge pump speeds and power loss. Theses results suggest that a volume of 4000 liters already approaches an asymtotes for charge pump speed and power loss, with the optimal charge pump speed of 2000 rpm being lower than the 2500 rpm assumed in Chapter 4. A choice of 1000 liters for the low-pressure accumulator volume and a charge pump speed of 2000 rpm meets the minimum pressure constraint with only slightly greater power loss than found for a volume of 4000 liter suggesting it would be a reasonable choice.

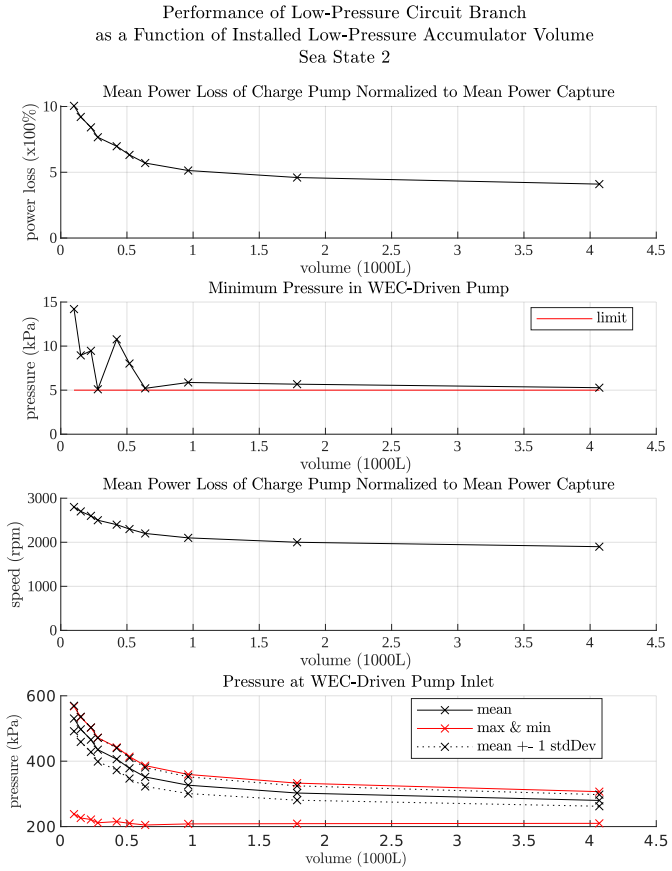

Figure C.3: Low-pressure accumulator sizing study results with optimal charge pump speed.